Numerical Modelling of Aerothermodynamics in Micro-Gas Turbines with Realistic Geometries

Heyu Wang

A dissertation submitted in partial fulfillment

of the requirements for the degree of

Doctor of Philosophy

of

University College London.

Department of Mechanical Engineering

University College London

May 29, 2024

I, Heyu Wang, confirm that the work presented in this thesis is my own. Where information has been derived from other sources, I confirm that this has been indicated in the work.

Abstract

The heavy use of fossil fuels, being major sources of carbon emissions, has intensified the global warming issue. Consequently, governments and organizations around the world have set a target to reach net zero emissions by 2050. Yet, with the rising needs for energy and transportation, electric engine technologies are not being leveraged to their full potential for various reasons. As a result, combustion gas turbines are expected to remain essential in the foreseeable future.

This thesis investigates the aerodynamics, aerothermal performance, and emission characteristics of various components in gas turbine systems. Initial studies focused on the dump diffuser combustor, a simplified representation of a gas turbine combustion chamber, analyzing the aerodynamic effects of geometric parameters such as the pre-diffuser divergence angle and dump gap ratio. The research revealed the potential for optimizing weight, length, and aerodynamic efficiency through design adjustments.

In subsequent sections, the aerothermal performance and emissions of a realistic micro-gas turbine geometry were investigated, employing a publicly available model for validation. Key parameters such as non-uniform outlet pressure, fuel-to-air ratio, and fuel injection velocity were identified as pivotal factors influencing the combustor's performance and emission characteristics. Through a thorough analysis of the combustor-turbine interaction, with a focus on clocking effects, the intricate balance and ramifications of various modelling approaches on aerothermal dynamics and soot emissions were elucidated. These findings underscored the significant impact of combustion modelling on predicting the aerodynamic performance of the turbine stage. Notably, unburned fuel migrating downstream the turbine vane was observed

to create elevated temperature fields, affecting heat transfer performance. Leveraging clocking effects holds promise for enhancing aerothermodynamic performance and reducing soot emissions. Leading-edge hot-streak impingement clocking was found to enhance aerodynamic efficiency, while mid-passage clocking mitigated turbine vanes' heat load and reduced soot emissions, presenting avenues for optimization.

Lastly, recommendations for future research, guided by the insights from the conducted studies, span the domains of compressor-combustor interaction, high-fidelity turbulence resolution, unsteady bladerow simulations, fuel type effects, and diverse operating points, providing a roadmap for further advancements in the field.

Impact Statement

The work presented in this thesis, focusing on micro-gas turbine numerical modeling, possesses the potential to make significant contributions both inside and outside academia.

Inside Academia:

- **Discipline and Future Scholarship**: This research provides deeper insights into component interactions within a micro-gas turbine, which will be valuable for future researchers seeking to optimize gas turbine performance. It establishes a foundation for subsequent investigations to push the scientific boundary of the current state-of-the-art.

- **Research Methods and Methodology**: The application of fully-coupled simulation approaches with combustion and droplet breakup models and in-depth analyses presented offers a methodological benchmark. Future research can leverage these methodologies for other complex gas turbine systems, thereby improving the accuracy and precision of simulations across a myriad of applications.

- **Curriculum Development**: The findings of this research can be integrated into academic syllabi related to mechanical engineering, thermodynamics, and renewable energy courses. This would ensure that students are exposed to cutting-edge knowledge, better preparing them for the challenges and opportunities in the field.

Outside Academia:

- **Commercial Activity**: Gas turbine manufacturers can adopt the insights from this study to enhance turbine performance and efficiency. As combustion turbines remain crucial, any improvement in their performance can lead to significant economic gains and reduce operational costs for industries relying on these turbines.

- **Environmental Quality**: By addressing the performance and emission characteristics of micro-gas turbines, this research directly contributes to strategies for reducing carbon emissions, promoting a cleaner environment and helping the engineering community to meet the net-zero target by 2050.

Realizing the Impact: To ensure the realization of these potential impacts, a multi-pronged dissemination strategy is suggested:

- **Scholarly Journals**: Publishing the findings in reputed conference proceeding and journals will ensure that the academic community can easily access and build upon this research. Parts of this thesis have already been published in the public domain with open-access.

- **Public Engagement**: Organizing seminars, webinars, or public lectures can help in directly communicating the benefits and potential applications of this research to a broader audience.

- **Collaborations**: Building partnerships with industries and fellow researchers will ensure the practical application of the research findings. Collaborative projects can lead to the rapid implementation of optimized turbine designs and operational strategies.

In conclusion, the research presented in this thesis has the potential to create ripples of positive impact, both immediate and long-term, across various sectors. By harnessing these insights and implementing the recommended strategies, we can move closer to a future where energy is both efficient and sustainable.

Acknowledgements

I would like to express my heartfelt gratitude to several individuals who have played an invaluable role in the completion of this thesis.

The journey of completing this thesis was not without its challenges, and the COVID-19 period brought about numerous setbacks and difficulties. However, it is thanks to the unwavering support, encouragement, and love of my parents that I was able to persevere and overcome these obstacles. Their sacrifices and belief in my abilities remained constant sources of motivation, even in the face of adversity.

I am immensely thankful to my supervisor, Professor Luo, for his guidance, mentorship, and scholarly insights throughout the research process. His expertise and dedication were instrumental in helping me navigate the unique challenges presented by the pandemic and ensured that this thesis reached its completion.

I also want to acknowledge my dear friend, Harry Phan, for his continuous encouragement, late-night discussions, and the occasional distraction that kept me sane during the most demanding phases of this project, particularly when the world around us was grappling with uncertainty. Your friendship has been a source of inspiration and much-needed respite during these trying times.

Finally, I would like to thank all those who, directly or indirectly, supported me during this academic endeavor amidst the difficulties brought about by the pandemic. Your contributions were significant, and I am deeply grateful for your presence in my life during this challenging period.

This thesis would not have been possible without the support and encouragement of these individuals, and for that, I am truly thankful.

I also would like to acknowledge the support of ARCHER2 supercomput-

ing resources provided by the UK Engineering and Physical Sciences Research Council under the project “UK Consortium on Mesoscale Engineering Sciences (UKCOMES)” (Grant No. EP/X035875/1). This work made use of computational support by CoSeC, the Computational Science Centre for Research Communities, through UKCOMES.

Contents

List of Figures

List of Tables

Nomenclature

ΔH_R	Reaction heat release per mole
δ	Identity matrix/Kronecker delta function
$\dot{m}_{air}$	Air mass flow rate
$\dot{m}_{fuel}$	Fuel mass flow rate
$\dot{W}_C$	Compressor power
$\dot{W}_t$	Turbine power
$\dot{y}$	Droplet distortion rate of change
$\dot{y}_0$	Initial droplet distortion rate of change
ε	Turbulent eddy dissipation
η	Efficiency
Γ	Diffusivity
λ	Thermal conductivity
$[I]$	Molar mass concentration of component I
μ	Dynamic viscosity
μ_t	Turbulent viscosity
μ_{eff}	Effective viscosity

ν_{kI} Stoichiometric coefficient for component I

Φ Angle of each complete clocking revolution

ρ Density

σ Surface tension

σ_k Turbulence model constant for the k equation

σ_ε Turbulence model constant for the ε equation

σ_ω Turbulence model constant for the ω equation

τ Shear stress

$\mathbf{S}_E$ Energy source term

$\mathbf{S}_M$ Momentum source vector

$\mathbf{U}$ Velocity vector

$\widetilde{S}_{fuel}$ Fuel consumption rate

$\widetilde{S}_{nulcei,c}$ Source term for nuclei combustion

$\widetilde{S}_{nulcei,f}$ Source term for nuclei formation

$\widetilde{S}_{soot,c}$ Source term for soot combustion

$\widetilde{S}_{soot,f}$ Source term for soot formation

A Pre-exponential collision frequency factor

C_b Critical amplitude coefficient in the TAB model

C_d Damping coefficient in the TAB model

C_f External force coefficient in the TAB model

C_k Restoring force coefficient in the TAB model

C_N Nuclei particle concentration number

C_S Soot particle concentration number

C_v New droplet velocity factor in the TAB model

C_{MFT} Virtual concentration

CAB Cascade Atomization and Breakup

E Activation energy

$ETAB$ Enhanced Taylor Analogy Breakup

F Thrust

f Chain branching coefficient

f_c Mass fraction of carbon in the fuel material

FAR Fuel-to-air ratio

g Chain termination coefficient

g_0 Linear termination coefficient of radical nuclei on the soot particles

H Specific total enthalpy

h Specific static enthalpy

K Energy ratio factor in the TAB model

k Turbulent kinetic energy

K_1 ETAB bag breakup factor in the ETAB model

K_2 Stripping breakup factor in the ETAB model

m_p Mass of a soot particle

n Temperature exponent

n_0 Spontaneous formation of radical nulcei from the fuel

N_b Number of turbine vanes in the blade row

N_C Total number of components in the multi-component fluid model

p'' Modified static pressure

p Static pressure

P_k Turbulence production due to viscous forces

Pr_t Turbulent Prandtl number

r Droplet particle radius

R_k Elementary reaction rate of progress for reaction k

ref Reference

RP Ratio of turbine power to compressor power

S_I Source term for production/consumption of component I in the multi-component fluid model

T Temperature

t Time

TAB Taylor Analogy Breakup

V_{slip} Slip velocity, relative velocity between the droplet particle and the surrounding fluid

W_I Molar mass of component I

We Weber number

X_N Specific concentratopn of radical nuclei

y Droplet distortion

y_0 Initial droplet distortion

Y_I Mass fraction for component I in the multi-component fluid model

Y_S Soot mass fraction

Chapter 1

Introduction

1.1 Research Background

Over the past few decades, the over-reliance on fossil fuels has exacerbated global warming. In response, governments and international entities have established a goal to achieve net zero emissions by 2050. However, despite increasing demands for transportation and energy—key contributors to carbon emissions—technological innovations in electric-powered engines remain underutilized for various reasons. Thus, combustion gas turbines will likely persist as vital components in the near term. Within the realm of renewable energy, micro-gas turbines play a pivotal role in electricity production. These turbines can run on alternative fuels, such as biogas, hydrogen, and liquid biofuels, providing the dual benefits of versatility and low initial investment. Their significance in generating electric and thermal energy from renewable sources is on the rise. In the realm of electric vehicles, micro-gas turbines can act as range extenders, replacing diesel engines. They also serve as propulsion mechanisms for unmanned aircraft.

Aside from the combustor, major components of micro-gas turbines include compressors and turbines. During conventional design processes, fundamental cycle parameters are determined from the requirements, followed by individual component design, considering spatial constraints and cycle boundary conditions. Unfortunately, inter-component interactions are often overlooked, particularly in early design phases. Standard numerical predictions frequently omit combustion effects in the turbine

stage due to constrained modeling resources. As the push for compact, lightweight components intensifies, the interplay between components will inevitably heighten, challenging traditional design approaches. This interactivity can influence both the turbine's performance and emission profiles.

It becomes evident that a thorough understanding of micro-gas turbine characteristics, both at design and off-design stages, is paramount for the evolution of advanced machines. This thesis undertakes a holistic exploration into the aerothermal performance and emission traits of a micro-gas turbine model, with the aim of optimizing its operation. Key focal points include combustion modeling, multi-species flow transportation, and the formation of particulate matter. This study stands as one of the few publicly available works addressing comprehensive performance issues at such a systemic level.

1.2 Research Questions

The present thesis seeks to deepen the understanding of combustion modeling and its implications on the aerodynamic, thermal, and emissions performance prediction of micro-gas turbines. To fulfill the research objectives, the following key research questions will be addressed:

- ***What is the role of combustion modeling in the prediction of micro-gas turbine performance?*** Conventional numerical approaches often overlook the effects of combustion when predicting the aerodynamic and heat transfer attributes of micro-gas turbines' main flow gas paths. Moreover, there has been a tendency to design components with minimal considerations for their integration with the combustion chamber.

- ***How do components in a micro-gas turbine interplay?*** The coupling with upstream and downstream components will be investigated. New gas turbine architectures will tend to have a stronger interaction between each component and independent design of each component will be less accurate.

- ***Is it feasible to harness these component interactions to enhance performance?*** If inter-component interactions prove influential, strategic design

alterations might be leveraged to improve the overall efficiency of the micro-gas turbine.

1.3 Overview of the Thesis

The following chapters form the main body of this thesis:

- **Chapter 1**: this chapter presents overview of the thesis and the research questions.
- **Chapter 2**: this chapter describes literature review related to the research questions arisen in the thesis. It starts with descriptions of the gas turbine theory and the Brayton thermodynamic cycle. Gas turbine emissions and regulations are also discussed. The interactions (combustor-turbine and compressor-combustor) among gas turbine components at the system and component level are discussed. Finally, the state-of-the-art in reacting flow modeling in gas turbine is discussed.
- **Chapter 3**: this chapter summarizes the Computational Fluid Dynamics (CFD) numerical methodology used across the thesis. Turbulence closure and turbulence models are discussed. Notably, combustion models, droplet breakup models, and soot formation models are also briefly described.
- **Chapter 4**: Dump diffuser combustor is a simple geometry that represents a gas turbine combustor system. This chapter investigates the aerodynamic performance of a dump diffuser combustor simple geometry and study the effects of boundary condition perturbation. The results in this chapter suggest further study on the interactions between components in a gas turbine system.
- **Chapter 5**: from this chapter onwards, a real geometry of a micro-gas turbine is adopted for further investigations. This chapter comprises of a validation of numerical predictions against experimental data for a bulk performance of the whole micro-gas turbine. Then the combustion chamber is the main focus of this chapter, where the effects of outlet flow non-uniformity, fuel-to-air ratio, and fuel injection velocity are discussed.

- **Chapter 6**: this chapter investigates the combustor-turbine interaction in more details. One of the novel feature is the use of fully-coupled domain, which allows the tracking of multi-species flow and soot formation and transport across the turbine stage. The predictions by the decoupled simulation approach is compared against that by the coupled method. Finally, the effects of stator clocking on the combustor efficiency, the turbine efficiency. the turbine heat transfer, and the soot formation are discussed.

- **Chapter 7**: this chapter summarizes the main results of this thesis and suggests some potential future works.

1.4 List of Publications

In this section, publications that were directly derived from the work done as part of this thesis are listed below. These publications were written whilst the author held the PhD research student status at the University College London.

- H. Wang and K. H. Luo, 2020. Numerical Investigation of Dump Diffuser Combustor Performance at Uniform and Non-Uniform Inlet Conditions. ASME Turbo Expo 2020 conference paper [12].

- H. Wang and K. H. Luo, 2023. Aerothermal Performance and Soot Emissions of Reacting Flow in a Micro-Gas Turbine Combustor. *Energies*, 16(7), pp. 2947 [13].

- H. Wang and K. H. Luo. Fully Coupled Whole-Annulus Investigation of Combustor-Turbine Interaction with Reacting Flow. *Energies*, 17(4), pp. 873 [14].

- H. Wang and K. H. Luo. Casing Treatment of Centrifugal Compressor in a Micro-Gas Turbine. Manuscript in preparation.

Chapter 2

Literature Review

2.1 Micro-Gas Turbine

2.1.1 Gas Turbine Theory

Gas turbine belongs to a family of internal combustion engines. There are four common processes during its operation: intake, compression, combustion, and exhaust. In aerospace applications, gas turbine produces a high velocity jet at the engine outlet, that creates thrust and pushes the aircraft forward. In power generation applications, the shaft is connected to a generator that produces electricity. Gas turbine engines have several advantages compared to traditional reciprocating engines because the four operation processes can be done simultaneously.

Figure 2.1 shows an illustration of a typical gas turbine layout. The multi-stage axial compressor compresses the incoming air flow. The high-pressure flow is fed into the annular combustion chamber, where fuel is injected. The mixture ignites and produces a high-temperature flow. The high-pressure high-temperature expands in the multi-stage axial turbine. This process produces a shaft work output that drives the compressor. The hot exhaust gas comes out of the nozzle and produces thrust.

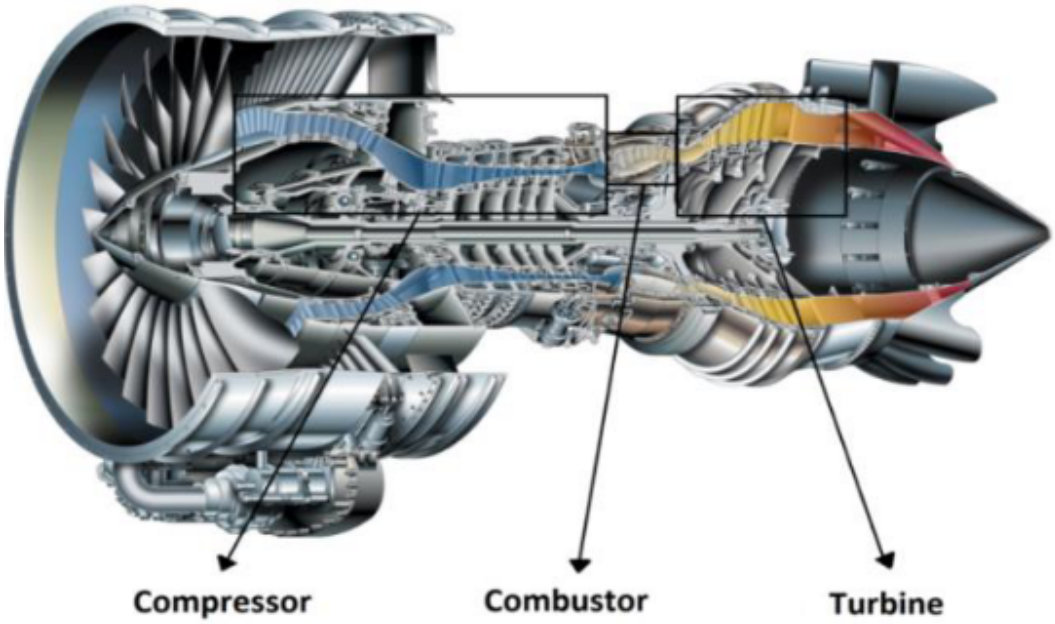

Figure 2.1: Cut-away view of a typical gas turbine, reproduced from [1].

2.1.2 Brayton Thermodynamic Cycle

Micro-gas turbine's operation follows the standard Brayton open-air cycle. Figure 2.2 illustrates the typical Brayton thermodynamic cycle of a micro-gas turbine. The micro-gas turbine thermodynamic processes are described as follows:

- 0-2: The incoming free-stream air at station **0** is slowed down by the inlet before entering the compressor at station **2**. The air static pressure increases as part of this air compression process. Ideally, the process is isentropic and the static temperature increases as shown in Figure 2.2.

- 2-3: The compressor imparts energy on the gas due to the work done by the rotor and increases both air temperature and pressure until the compressor exit station **3**. Ideally, the compression process is isentropic, as suggested by the vertical line in Figure 2.2. In reality, non-isentropic losses occur in the compressor and the line should lean to the right to reflect an increase in entropy.

- 3-4: The combustion process in the chamber occurs at constant pressure from station **3** to **4**. The temperature rise depends on the fuel type and the fuel-to-air

ratio.

- 4-5: The hot exhaust gas coming out of the combustor enters the turbine at station **4**. Work done by the hot gas flow imparts energy to the turbine stage. Because the turbine and the compressor are on the same shaft, the work done on the turbine needs to be balanced by the compressor work done.
- 5-8: The air exits the turbine and enters the exhaust nozzle at station **5**. The nozzle brings the air flow to the free-stream conditions at station **8** in an isentropic process.

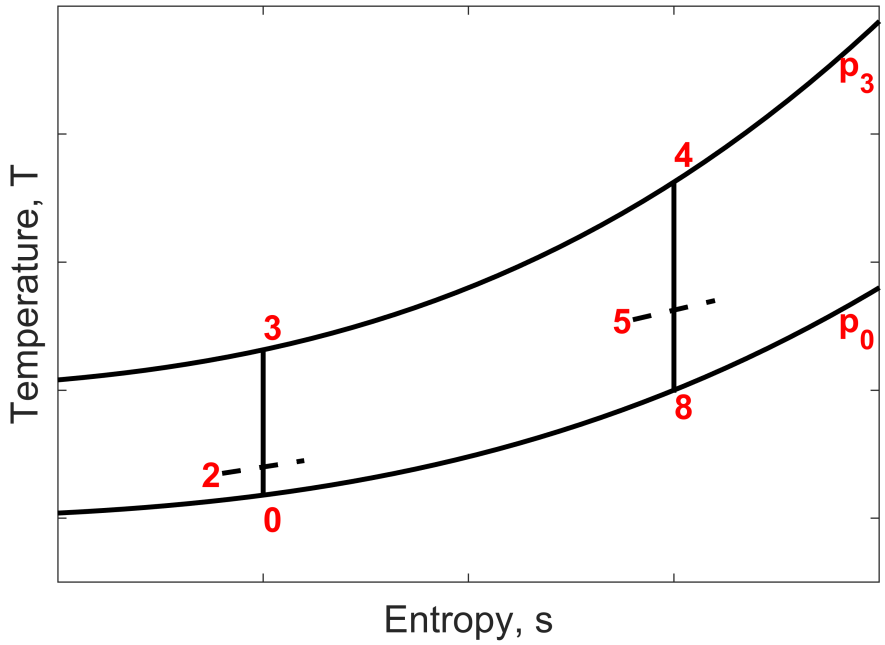

Figure 2.2: Brayton cycle T-s diagram.

The cycle is then completed. The area under the T-s diagram is proportional to the engine thrust. The overall cycle efficiency of a gas turbine can be improved by either increasing the turbine entry temperature or increasing the overall pressure ratio. This relationship is presented in Equation 2.1, where the overall cycle efficiency is proportional to the pressure ratio and the temperature ratio.

$$\eta_{cycle} = \frac{\theta\eta_t\left(1-1/r^{(\gamma-1)/\gamma}\right)-\left(r^{(\gamma-1)/\gamma}-1\right)/\eta_c}{\theta-1-\left(r^{(\gamma-1)/\gamma}\right)/\eta_c} \tag{2.1}$$

where:

η_{cycle} is the overall cycle efficiency

η_t is the turbine efficiency

η_c is the compressor efficiency

$\theta = T_{04}/T_{02}$ is the total temperature ratio between the turbine inlet and the compressor inlet

$r = P_{03}/P_{02}$ is the total pressure ratio between the compressor outlet and the compressor inlet

2.2 Gas Turbine Emissions and Regulations

Emissions have long been a concern for both aeronautical and stationary gas turbines, alongside efficiency and reliability. However, in recent years, the strict regulations in emission control has arose and forced development of the combustion system. The reduction of emissions is not only beneficial in terms of environmental consequences but also can lead to a potential advantage for engine manufacturers in an increasingly competitive market. The emissions can be either noise or exhaust. However, in the context of this work, we only consider the exhaust emissions.

The exhaust from a gas turbine combustion system includes carbon monoxide (CO), carbon monoxide (CO_2), nitrogen oxides (NO_x), unburned hydrocarbons (UHC), water vapour, and particulates. Among these combustion products, the major species are CO_2, N_2, H_20, and O_2, whereas CO, UHC, NO_x, SO_x, and particulates are minor species. Table 2.1 and Table 2.2 shows the typical concentration of each species (in percent volume concentrations for major species and in percent parts per million volume concentrations) and the source of each species

Major Species	**Typical Concentration (% Volume)**	**Source**
Nitrogen (N_2)	66-72	Inlet air
Oxygen (O_2)	12-18	Inlet air
Carbon Dioxide (CO_2)	1-5	Oxidation of fuel carbon
Water vapour (H_2O)	1-5	Oxidation of fuel hydrogen

Table 2.1: Major species of gas turbine exhaust emissions of conventional fuels, adapted from [2].

Minor Species	Concentration (PPMV)	Source
Nitric Oxide (NO)	20-220	Oxidation of atmospheric nitrogen
Nitrogen Dioxide (NO_2)	2-20	Oxidation of fuel-bound organic nitrogen
Carbon Monoxide (CO)	5-330	Incomplete oxidation of fuel carbon
Sulphur Dioxide (SO_2)	Trace - 100	Oxidation of fuel-bound organic sulphur
Sulfur Trioxide (SO_3)	Trace - 4	Oxidation of fuel-bound organic sulphur
Unburned Hydrocarbons (UHC)	5-300	Incomplete oxidation of fuel or intermediates
Particulates	Trace - 25	Inlet ingestion, fuel ash, hot-gas path attrition ,incomplete oxidation of fuel or intermediates

Table 2.2: Minor species of gas turbine exhaust emissions of conventional fuels, adapted from [2].

Among the exhaust emissions, carbon dioxide and water vapour are usually not considered as pollutants because they are must-have products of the combustion process of a hydrocarbon fuel. On the other hand, other species can affect the wellbeing of people in the neighbourhood of airports as well as can pollute the stratosphere at cruise altitudes [15]. To be specific, carbon monoxide can reduce oxygen absorption capacity of the blood vessels. On top of that, unburned hydrocarbons can combine with nitrogen oxides to form photo chemical smog. Nitrogen oxides encourages the formation of smog and acid rain. In addition, each specie is also a function of operating conditions.

2.2.1 Nitrogen oxides

Thermal NO_x: formed from the oxidation of the free nitrogen

- Increases with fuel-to-air ratio or firing temperature
- Increases with the combustor inlet air temperature
- Increases with the combustor inlet pressure
- Increases with residence time in the flame zone
- Decreases with water or steam injection

Organic NO_x formed from the oxidation of organic bound nitrogen in the fuel

- Only important if the amount of fuel-bound nitrogen is significant as in crude or residual oil

2.2.2 Carbon monoxide

As firing temperature decreases, carbon monoxide production increases. Figure 2.3 shows a typical curve of carbon monoxide production against firing temperature for natural gas and distillate oil for the GE MS7001EA gas turbine model.

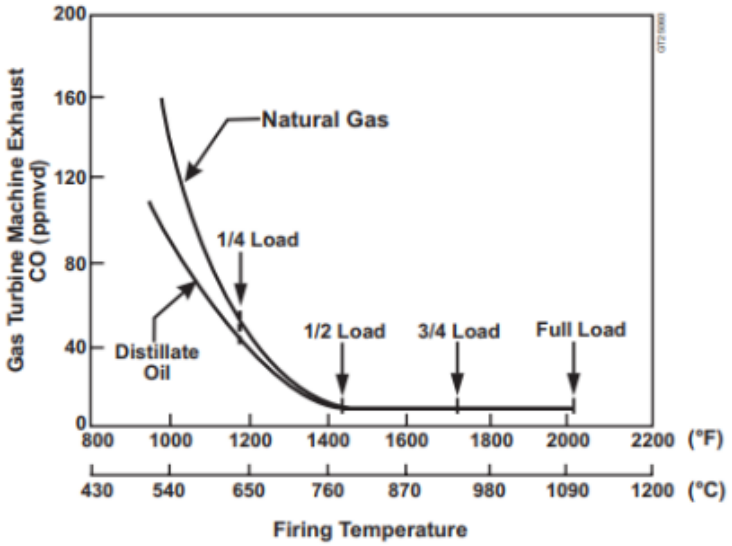

Figure 2.3: CO emissions against firing temperature of GE MS7001EA, adapted from [2].

2.2.3 Unburned hydrocarbons

The distribution of unburned hydrocarbons are similar to that of carbon monoxide. Figure 2.4 shows a typical hyperbolic curve of unburned hydrocarbons production against firing temperature for natural gas and distillate oil for the GE MS7001EA gas turbine model.

2.2.4 Sulphur oxides

Sulphur in the fuel can be converted to sulphur dioxide SO_2 and sulphur trioxide SO_3. The latter can combine with water vapour to form sulphuric acid. The various sulphur oxide emissions can be calculated from the fuel flow rate and the sulphur content in fuel. This relationship is shown in Figure 2.5.

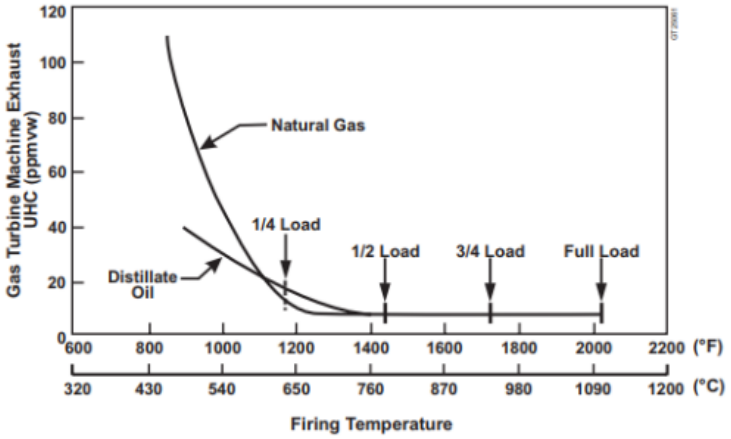

Figure 2.4: UHC emissions against firing temperature of GE MS7001EA, adapted from [2].

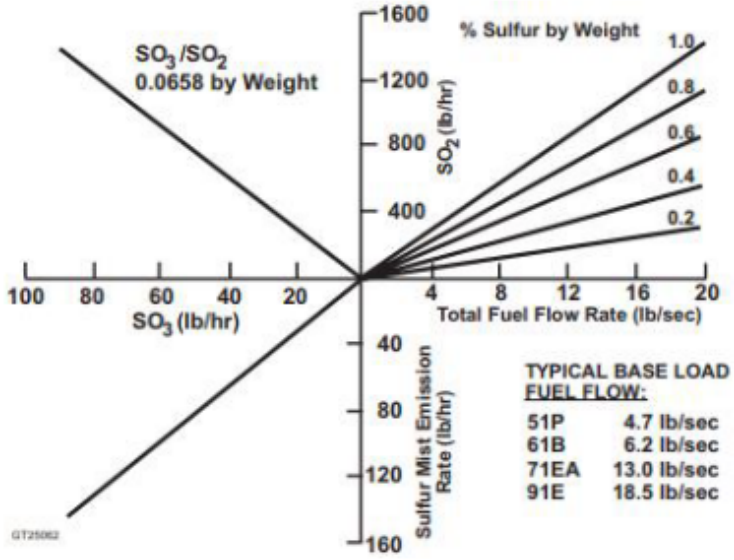

Figure 2.5: Sulfur oxide emission characteristics, adapted from [2].

The production of CO and UHC reaches maximum at low power condition, while the production of NO_x and smoke peaks at maximum power. This relationship is presented in Figure 2.6. For modern gas turbines, CO and UHC can be effectively reduced at low power conditions. However, NO_x reduction still remains a challenge.

2.2.5 NO_x reduction techniques

According to Lefebvre [3], the most effective way to reduce NO_x emissions is to: a) reduce the reaction temperature, or b) decrease residence time at high temperature. The reduction of reaction temperature is based on avoiding the exact ratio

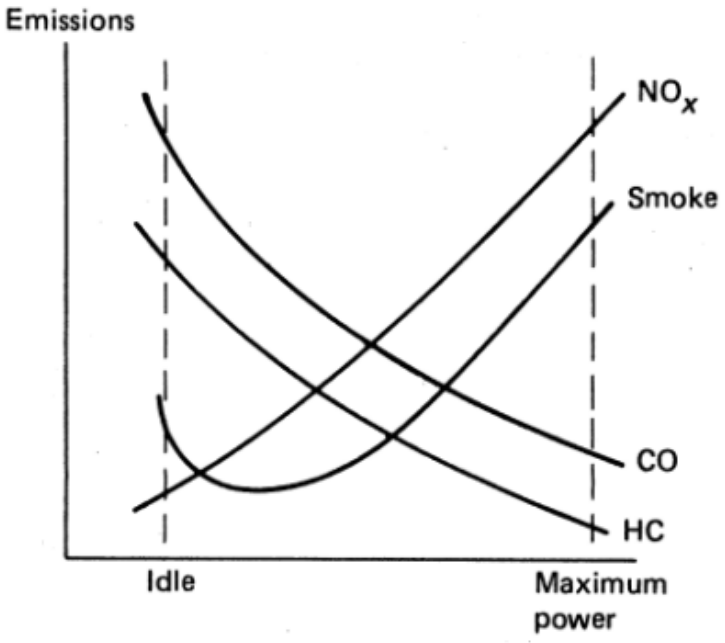

Figure 2.6: NO_x, smoke, CO, and UHC emission characteristics with power settings, adapted from [3].

of chemicals that are introduced into the reaction during combustion. The reaction temperature can be reduced by various methods:

- Reducing oxygen content by increasing fuel concentration
- Reducing energy input by using lean fuel mixtures
- Water or steam injection

The residence time at high temperature should be minimised to prevent a huge amount of nitrogen from becoming ionised. The elimination of hot-spots is therefore also a typical target, which aims to prevent NO_x from local formation.

2.2.5.1 Water/steam injection

Another technology has been adopted to reduce NO_x formation is water/steam injection [16]. Water and steam can be injected in various ways:

- Directly into the flame via a number of nozzles that are located at the head of the combustor [17]
- Into the compressor [17]

- At upstream of combustion liner which flows through the main air swirler to the combustion zone [18]

However, it has been reported that this method has many drawbacks such as:

- Increased capital cost: due to additional fuel needed to heat the water to combustion temperature
- Cost of water treatment: to prevent the deposit accumulation, water purity is desired
- Increased fuel consumption

For aero-engine propulsion, the task of carrying another water tank is almost impossible physically. A less apparent disadvantage of water/steam injection is by lowering the flame temperature, the CO and UHC production will increase accordingly. Indeed, for a conventional combustor, an optimum temperature should be in the range between 1670K and 1900K as shown in Figure 2.7. Within this range, both CO and NO_x emissions can be kept below 25 and 15ppm, respectively.

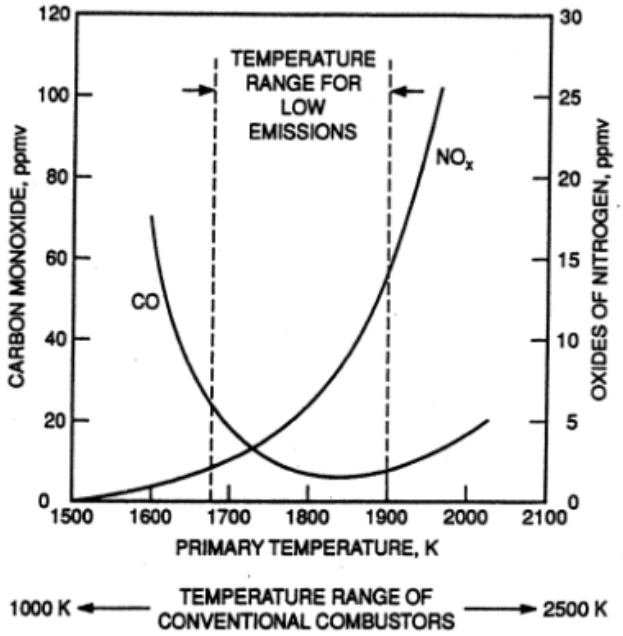

Figure 2.7: Influence of primary zone temperature on CO and NOx emissions.

2.2.5.2 Catalytic combustor

Selective catalytic reduction (SCR) is the technology that involves injecting ammonia into the stream in the presence of a catalyst, which then converts NO_x into molecular nitrogen and water. The exhaust gases are first passed through an oxidation catalyst and then mixed with ammonia before proceeding to the SCR catalyst. The oxidation process removes NO_x by converting them to N_2 and H_20 [15]. The chemical equations are given as below:

$$6NO + 4NH_3 \rightarrow 5N_2 + 6H_2O \tag{2.2}$$

$$6NO_2 + 8NH_3 \rightarrow 7N2 + 12H_20 \tag{2.3}$$

SCR methodology tends to be more effective with natural gas fuel and is shown not to be compatible with liquid fuel, particularly with large amount of sulphur.

2.2.5.3 Leaned premixed combustion

In a conventional combustion chamber, the primary zone is usually operated with high fuel-to-air ratio. This leads to localised combustion with high temperature and high amount of NO_x exhaust as the result of little air available for the combustion process. The lean premixed combustor therefore aims to eliminate the local hot-spots by pre-mixing fuel and air and operating the primary zone with low fuel-to-air ratio. Combustion of the premixed prevaporised mixture hence takes place at low and uniform temperature. NO_x exhaust is also reduced as the result. Poeschl et al. [19] reported that NO_x exhaust concentration can be reduced up to 10 ppm by using a premixed and prevaporised mixture. In addition, Leonard and Stegmaier [20] showed that the flame temperature did not exceed 1900K during the combustion of premixed prevaporised mixture. As a result, the amount of NO_x exhaust is not proportional to the residence time. This finding is beneficial for the lean combustion system because a long residence time can be used to reduce the amount of CO and UHC exhaust without increasing the amount of NO_x exhaust. However, there exists a danger of flashback at high power settings due to the high temperature premixed fuel. In addition, because of the low fuel-to-air ratio, there is another danger of flame

instability (blow-out) at low power conditions.

2.2.5.4 RQL combustion

RQL stands for Rich Burn-Quick Quench-Lean Burn combustion. This combustor architecture was proposed by Mosier and Pierce [21]. RQL combustor adopts a rich zone with high fuel-to-air ratio to improve the combustion stability. In addition, the NO_x exhaust is reduced due to the combined effects of low temperature and lack of oxygen. The cooling air for the combustor liner wall is not included in the rich zone to prevent the NO_x formation to increase due to near-stoichiometric mixtures. After the rich burn, the combustion products are then cooled rapidly to the temperature level where NO_x production is limited. This stage requires a fast cooling rate so the combustion regime shifts rapidly from the rich-burn to lean-burn combustion without the formation of local hot-spots. Figure 2.8 illustrates the NOx formation routes of the RQL combustor. The RQL combustor technology has been adopted in the TALON family of Pratt & Whitney [22] and Rolls-Royce Trent 1000 [23].

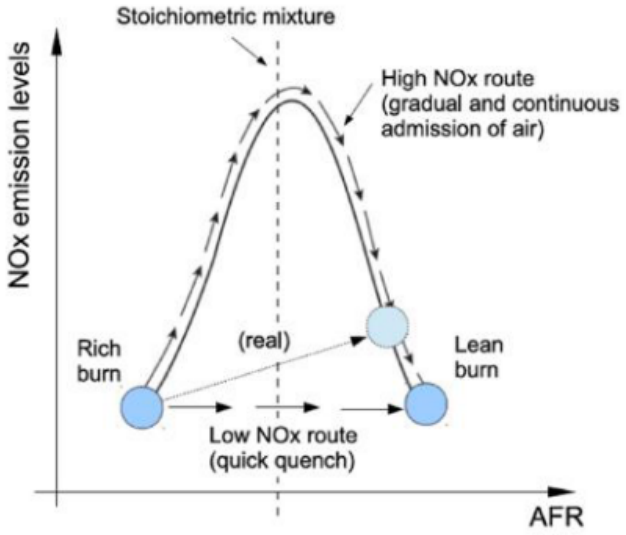

Figure 2.8: Working principle of the RQL combustor, reproduced from [4].

2.2.6 Soot reduction techniques

Soot is the particulate matter resulting from incomplete combustion of hydrocarbon fuels. Soot formation is undesirable due to environmental concern as well as the damages of combustion equipment. When present in sufficient particle size and

quantity, soot in exhaust gases constitutes a black smoke. To reduce soot emissions, additives can be added to fuel apart from the combustor design modifications. Howard and Kausch [24] reviewed several metal additives and demonstrated that the soot content can be effectively reduced in practical flames, particularly with high power, high load, or poorly maintained combustors.The most effective metal additives were identified as Mn, Fe, and Ba, although those metal oxide particulates needs further examination on the health effects. The review by Chiong et al. [25] showed that liquid biofuels exhibit cleaner combustion characteristics with NO_x, CO, and soot reduction. Apart from the high production cost, liquid biofuels may suffer difficult fuel flow delivery and clogged atomizer orifice, which inhibits their extensive use at the current stage.

2.3 Combustor-Turbine Interactions

The interface of combustor/turbine is an active subject of research. It receives extensive attention because of the desire to increase the turbine entry temperature to increase the engine efficiency. In a modern lean-burn combustor system, a high non-uniformity at the combustor/turbine interface has been reported with very high levels of non-uniform total pressure, turbulence intensity, length scales, and a residual swirl [26, 27, 28]. Figure 2.9 illustrates the flow structures downstream of the swirler interacting with the turbine Nozzle Guide Vane (NGV).

The Nozzle Guide Vane (NGV) is the first turbine component that is in contact with the hot exhaust of the combustor system. Therefore, its resistance to extremely hot gas is essential in the development of this component. In lean-burn combustor, the complex flow field depends heavily on the configurations of upstream swirler [29]. In order to meet the aerothermal requirement of the NGV, an integrated approach has been proposed taking into account the strong coupling between the combustor and the turbine. Figure 2.10 illustrates the concept of integrated NGV design. In the conventional configuration, the NGVs are separated from the combustor wall. In the integrated NGV design, some of the vanes can be connected directly downstream of the combustor wall. The cooling air in the combustor wall gap can be used cool the

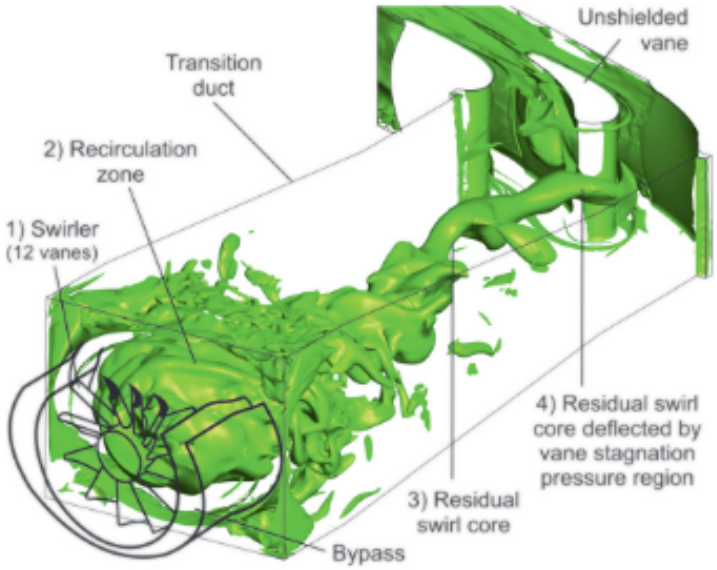

Figure 2.9: Combustor swirler-turbine vane interaction, reproduced from [5].

vane. Internal cooling requirement for these vanes can be significantly reduced.

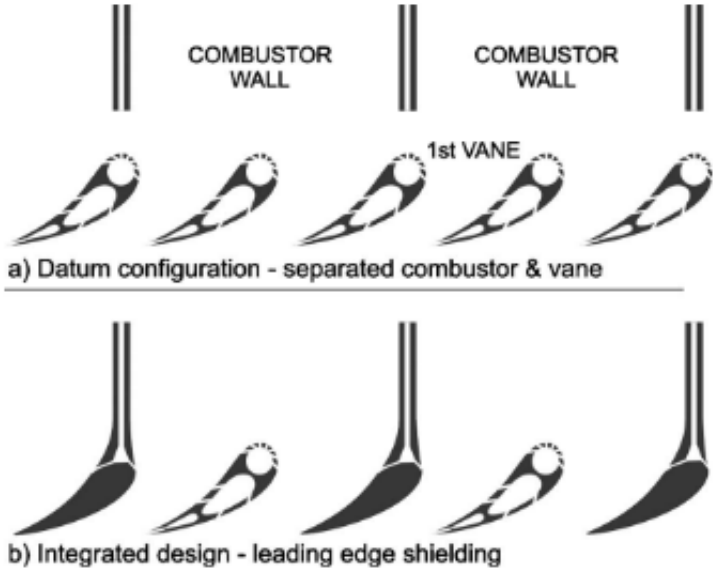

Figure 2.10: Illustrations of the integrated combustor-NGV design with leading edge shielding, reproduced from [6].

As shown in Figure 2.11, Rosic et al. [6] also proposed another possible concept for integrated NGV design with new vane geometry. The number of vanes in this design concept can be able to reduce by half, which significantly reduces the manufacturing cost. This integrated NGV has been tested in a modular high-speed linear cascade. The total pressure loss coefficient of the integrated NGV can be reduced by more than 25% compared to a baseline case [30]. This is attributed to the reduction in profile loss (less wetted area) and endwall loss (more aggressive 3D aerodynamics design). On the aerothermal aspect, the integrated NGV design can drastically reduce the heat transfer on the vane surface. Therefore, the vane suction surface is less influenced by the incoming hot exhaust gas from the combustor. As a result, the vane would have better endurance against the high temperature. Similar observation have been made in a realistic-engine condition testing, which dictates the reduction of heat transfer coefficient for the integrated NGV design due to the elimination of the leading edge stagnation pressure [27]. Further researches are still taking place to investigate the potential of this concept [31, 28]. Hybrid RANS/LES treatment has also been investigated to couple the complex flow in the combustor and the flow in the turbine [32, 33, 34].

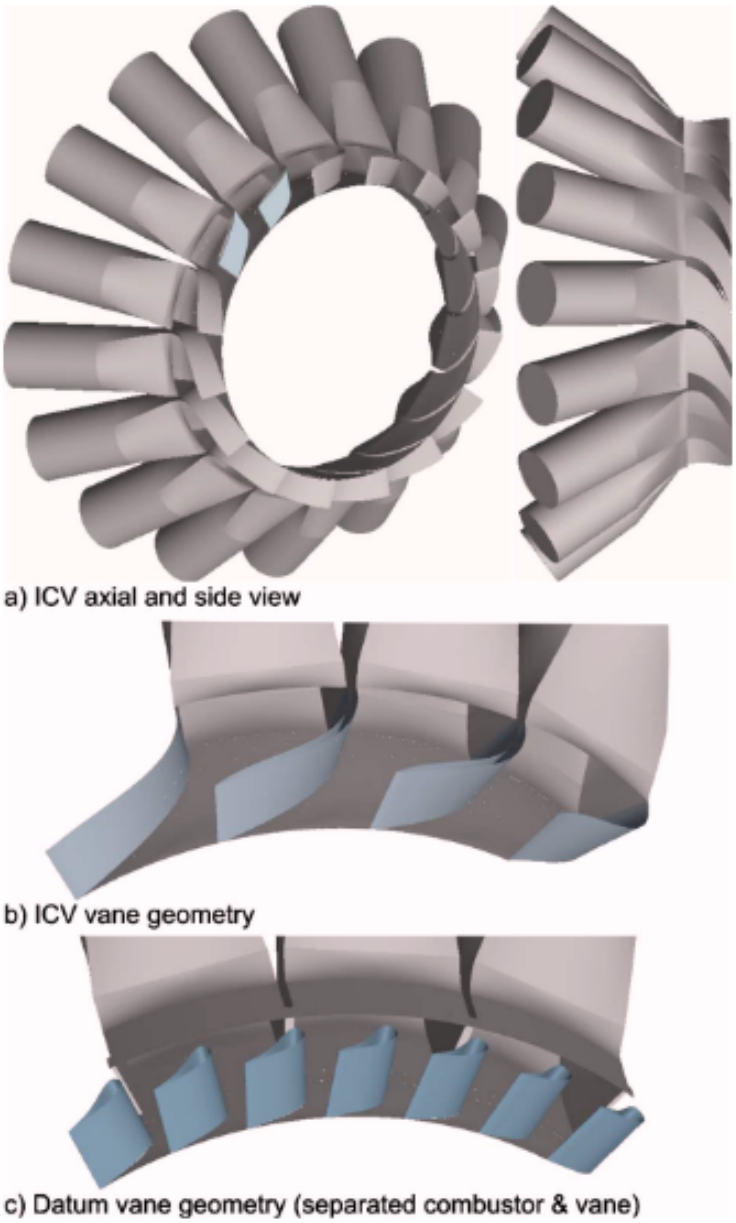

Figure 2.11: Illustrations of the integrated combustor-NGV design with leading edge shielding, reproduced from [6].

2.4 Compressor-Combustor Interactions

In the compressor-combustor system, there exists a coupling among two components at different extent. As in a typical gas turbine configuration illustrated in Figure 2.12, the interface between the compressor exit and the pre-diffuser inlet could include a 3D turbulent wake mixing, annulus endwall boundary layers, and possibly flow separation [7].

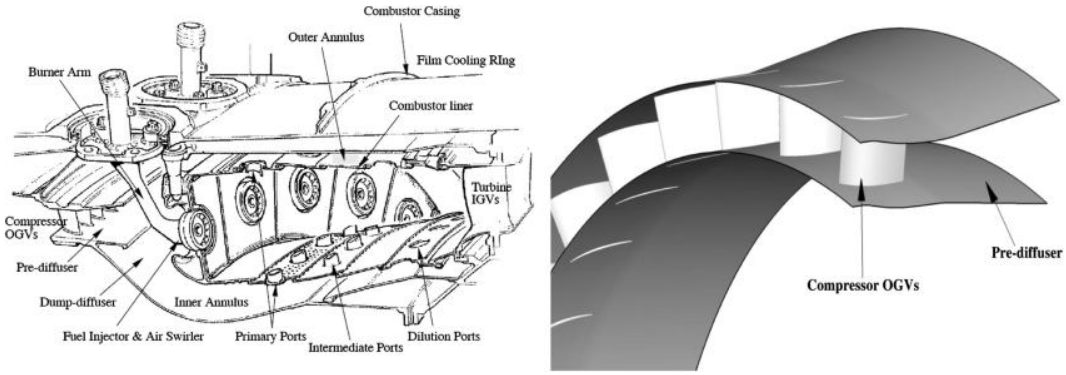

Figure 2.12: Typical gas turbine configuration with the compressor-combustor interface, reproduced from [7].

The interaction between the compressor and the combustor can happen in two ways [35, 36]:

- Upstream-to-downstream: three-dimensional wakes and turbulence of the compressor exit flow help to re-energise the boundary layers and delay the onset of bubble separation.
- Downstream-to-upstream: the dump gap between the compressor exit and the combustor inlet can help to establish an upstream potential field to cause high static pressure in mid-passage at the pre-diffuser exit. This would help to enhance the flow turning and lead to a delay of bubble separation onset.

Previous researches showed that the rotor exit flow field can be altered significantly if the combustor flow split increases to 70%, which represents a typical configuration for a modern lean burn combustor system [36]. The diffuser exit flow is more distorted when the cowl flow split increases. A low pressure at diffuser mid-passage is also detrimental to the boundary layer attachment. In another study, the diffuser exit flow was showed to deteriorate if the dump gap designed for a rich-burn combustor remains the same for a lean-burn design [37]. A significant flow non-uniformity could be observed when the flow feed to the injector increased from 50% to 70%. Walker concluded that a larger dump gap was necessary for a higher mass flow injector in a lean-burn system to prevent the convected disturbances of the compressor system. This modification came with a penalty because the loss would be increased as the dump gap extended.

As a result, several researchers have attempted to design a closely coupled Outlet Guide Vane (OGV) and a pre-diffuser [8, 38]. An improved design of the integrated OGV was realized by the combination of blade sweep and lean as showed in Figure 2.13. The improvements came from a higher momentum fluid transport towards the endwall, which off-loaded the pre-diffuser endwall boundary layer. This design modification led to a better resistance to the adverse pressure gradient and allow a higher area ratio diffuser design.

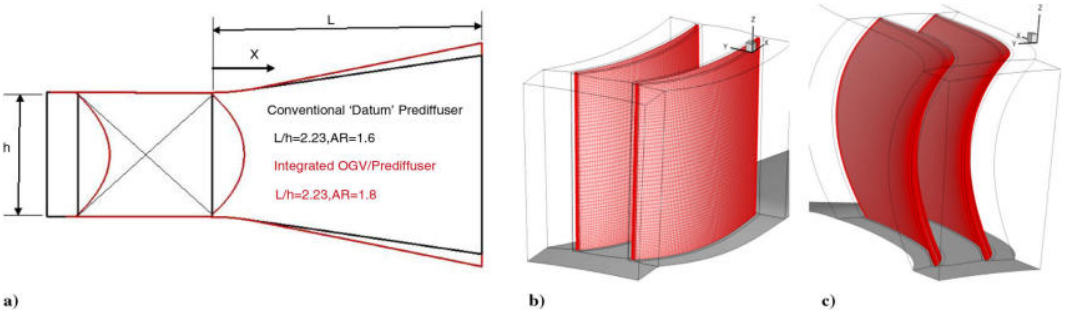

Figure 2.13: Illustration of the integrated compressor OGV-pre diffuser concept, reproduced from [7].

Figure 2.14 presents the measurements of axial velocity contours at the compressor/diffuser interface. It can be seen that the flow near the endwall has been re-energised, whereas the flow in mid-passage has much thicker wake structures. The re-energisation of the endwall boundary layer flow is the merit of this design technique and the mid-passage flow distortion does not show much damaging consequences. With the integrated OGV design, the inner and outer annulus loss has been reduced by 10% and 20%, respectively. Rolls-Royce has already used the integrated OGV concept in its TXWB design [35].

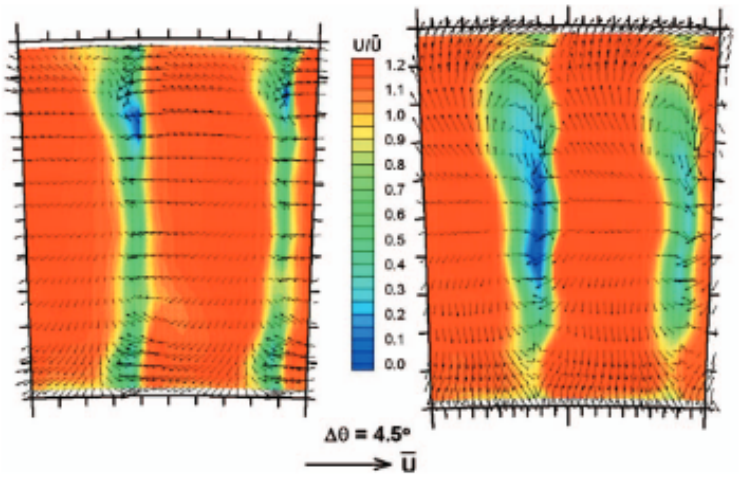

Figure 2.14: Illustration of the integrated compressor OGV-pre diffuser concept, reproduced from [8].

On the aspect of numerical modeling, the compressor flow is characterised by mostly the attached flow around the blades, whereas the flow in a combustor is characterised by detached flows, chemical reactions, and fuel spray [39]. Typically, RANS solver is used for the compressor flow and LES solver is preferred for the combustor flow. As a result, there has been many efforts to establish a hybrid RANS/LES solver to study the coupling effects of the compressor/combustor system [40, 41, 39, 42, 43].

2.5 Review of Numerical Modelling for Micro-Gas Turbines

The current study utilizes a turbojet-type micro-gas turbine, derived from the KJ66 model [10]. Originally designed for small radio-controlled unmanned aerial vehicles, this turbine model and its variants have undergone extensive investigation by other researchers due to the availability of both geometric and operational details. Xiang et al. [44] analysed the compressor stage performance of a KJ66 using both steady and unsteady simulation methods. The unsteady simulation provided detailed insights into transient flow behaviors during operation. Teixeira et al. [104] demonstrated the capability of performing an integrated fully coupled engine simulation on a redesigned KJ66, capturing component interactions through mixing-plane interfaces

and a non-linear harmonic methodology. Combustion was modelled using a simplified flamelet model, with no inclusion of a soot model. More recently, Yang et al. [11] conducted a full-engine 2D throughflow simulation on a KJ66 micro gas turbine, offering computational efficiency and enabling performance analysis across various operating points. With advancements in computational hardware, the frequency of full-engine simulations has steadily increased, with ongoing growth projected. For instance, Xu et al. [45] compared 3D full-engine simulation predictions between coupled and uncoupled schemes, noting significant errors in the uncoupled scheme due to boundary condition uncertainties and low-dimensional forced mixing at component interfaces. Arroyo et al. [46] demonstrated a 360-degree large-eddy simulation of the DGEN-380 demonstrator engine, including a fully integrated fan, compressor, and annular combustion chamber under take-off conditions. Xu et al. [47] proposed a component-coupled approach with power balance iteration technique for 3D full-engine CFD simulations, showcasing its robustness across different operational states.

Based on the literature review, it's evident that most numerical investigations of micro-gas turbines employ reduced-order modelling methodologies. For instance, Yang et al.'s throughflow method [11] significantly reduces computational time, facilitating whole-engine modelling, yet relying on empirical correlations, potentially compromising accuracy. Studies employing Computational Fluid Dynamics often employ reductions in simulation domain and physics modelling. A common domain reduction technique involves periodicity boundary conditions to exploit the repeating nature of annular bladerows. However, connecting blade-rows with differing blade counts necessitates special techniques, and imposing periodicity can restrict circumferential wavelength, particularly during stall and surge conditions. Consequently, individual simulation of micro-gas turbine components is common. Acknowledging the limitations of decoupled simulation, recent efforts aim to model the entire micro-gas turbine, though physics modeling may be simplified to accommodate increased mesh size, such as neglecting soot particles formation and their transport processes.

Hence, this thesis proposes a fully coupled whole annulus simulation approach,

incorporating reacting flow and soot formation to investigate micro-gas turbine engine performance. The absence of periodicity conditions and direct linking of domains in a single simulation (full coupling) will enable modelling of combustion processes and multi-species flow transportation across all sub-components, facilitating comprehensive exploration of flow field dynamics, aerothermal performance, and pollutant emissions.

Chapter 3

Numerical Methodology

3.1 Finite-Volume Computational Fluid Dynamics

The solver ANSYS CFX is adopted in the current work. It is an implicit finite volume-based Navier-Stokes solver. The governing equations represent the conservation of mass, momentum, and energy at each instantaneous time step are described as follows:

$$\frac{\partial \rho}{\partial t} + \nabla \cdot (\rho \mathbf{U}) = 0 \tag{3.1}$$

$$\frac{\partial (\rho \mathbf{U})}{\partial t} + \nabla \cdot (\rho \mathbf{U} \otimes \mathbf{U}) = \nabla p + \nabla \cdot \tau + \mathbf{S}_M \tag{3.2}$$

$$\frac{\partial (\rho H)}{\partial t} - \frac{\partial p}{\partial t} + \nabla \cdot (\rho \mathbf{U} H) = -\nabla (\lambda \nabla T) + \nabla \cdot (\mathbf{U} \cdot \tau) + \mathbf{S}_E \tag{3.3}$$

where the stress tensor τ is related to the strain rate by:

$$\tau = \mu \left[\nabla \mathbf{U} + (\nabla \mathbf{U})^T - \frac{2}{3} \delta \nabla \cdot \mathbf{U} \right] \tag{3.4}$$

and H is the total enthalpy:

$$H = h + 0.5\mathbf{U}^2 \tag{3.5}$$

The term $\nabla \cdot (\mathbf{U} \cdot \tau)$ is the viscous work term that represents the work due to viscous stresses. $\mathbf{S}_M$ and $\mathbf{S}_E$ are the source terms for the momentum and energy equation, respectively.

The advection terms are discretized by the bounded high-resolution scheme similar to Barth and Jespersen [48]. Pressure-velocity coupling is done by the 4th order smoothing algorithm similar to Rhie and Chow [49]. The algebraic multigrid method is used to accelerate the solver convergence rate. The solution is marched with the pseudo time step until the convergence criteria are reached and the residuals drop several orders of magnitude. To close the governing equations, a turbulence model needs to be specified.

3.2 Turbulence Modelling

Turbulence consists of unsteady eddies of varying scales. The eddies' structure is complicated and three-dimensional. These eddies' motion induce chaotic fluctuations in both spatial and temporal dimension of the flow field. The effects of turbulence are more pronounced at high Reynolds number (typically in gas turbine flow), when the inertia forces dominate the viscous forces. Turbulence can have a significant effect on the flow characteristics.

Turbulence at all scales can be resolved directly using the Direct Numerical Simulation (DNS). However, a DNS model would require a very small mesh and time step to capture small eddies and their motions, which makes it prohibitive for routine simulations at the industrial scale. To enable a more efficient prediction of turbulence effects, turbulence models can be adopted. Modeling turbulence is difficult and is still an active area of research. Large Eddy Simulation (LES) is the next level of turbulence model hierarchy after Direct Numerical Simulation, which is more efficient but less accurate. The rationale behind LES technique is the separation of scales, where large eddies are resolved and small eddies are modeled. Nevertheless, LES is still prohibitive for routine simulations. As a result, statistical Reynolds-averaged (RANS/URANS) turbulence models are the most popular model at the industrial level. The rationale behind RANS model is the separation of an averaged component and an additional time-varying component, based on the assumption/observation that a turbulent flow would reach a statistically averaged position after a while. In RANS technique, turbulence of all scales are modeled.

Thus, RANS/URANS models are much more computationally efficient compared to DNS and LES.

In RANS model, a velocity U_i is separated into an average component $\overline{U_i}$ and a time-varying component u_i:

$$U_i = \overline{U_i} + u_i \tag{3.6}$$

The averaged component is obtained by averaging instantaneous data over a long time:

$$\overline{U_i} = \frac{1}{\Delta t}\int_t^{t+\Delta t} U_i\, dt \tag{3.7}$$

If the averaged variables are substituted into the governing equations, extra Reynolds stress terms will arise from the nonlinear convective term. Turbulence models close the Reynolds averaged equations by providing models for the computation of the Reynolds stresses. In ANSYS CFX, RANS turbulence models can be largely classified into two categories: eddy viscosity models and Reynolds stress models.

3.2.1 Eddy Viscosity Turbulence Models

Eddy viscosity turbulence models propose that the Reynolds stresses are proportional to mean velocity gradients by the gradient diffusion hypothesis:

$$-\rho\overline{u_i u_j} = \mu_t\left(\frac{\partial U_i}{\partial x_j} + \frac{\partial U_j}{\partial x_i}\right) - \frac{2}{3}\delta_{ij}\left(\rho k + \mu_t\frac{\partial U_k}{\partial x_k}\right) \tag{3.8}$$

where μ_t is the eddy viscosity that needs to be modeled.

The Reynolds averaged momentum equations become:

$$\frac{\partial \rho U_i}{\partial t} + \frac{\partial}{\partial x_j}\left(\rho U_i U_j\right) = -\frac{\partial p'}{\partial x_i} + \frac{\partial}{\partial x_j}\left[\mu_{eff}\left(\frac{\partial U_i}{\partial x_j} + \frac{\partial U_j}{\partial x_i}\right)\right] + S_M \tag{3.9}$$

where S_M is the sum of the body forces; $\mu_{eff} = \mu + \mu_t$ is the effective viscosity; $p' = p + \frac{2}{3}\rho k + \frac{2}{3}\mu_{eff}\frac{\partial U_k}{\partial x_k}$ is the modified pressure.

The Reynolds averaged energy equation becomes:

$$\frac{\partial \rho H}{\partial t} - \frac{\partial p}{\partial t} + \frac{\partial}{\partial x_j}\left(\rho U_j H\right) = \frac{\partial}{\partial x_j}\left(\lambda \frac{\partial T}{\partial x_j} + \frac{\mu_t}{Pr_t}\frac{\partial h}{\partial x_j}\right) + \frac{\partial}{\partial x_j}\left[U_i\left(\tau_{ij} - \rho\overline{u_i u_j}\right)\right] + \mathbf{S}_E \tag{3.10}$$

3.2.1.1 The $k-\varepsilon$ model

The $k-\varepsilon$ model proposes that the turbulence viscosity is related to the turbulence kinetic energy k and the turbulence eddy dissipation ε:

$$\mu_t = C_\mu \rho \frac{k^2}{\varepsilon} \tag{3.11}$$

Two additional transport equations will be solved for k and ε:

$$\frac{\partial \rho k}{\partial t} + \frac{\partial}{\partial x_j}\left(\rho U_j k\right) = \frac{\partial}{\partial x_j}\left[\left(\mu + \frac{\mu_t}{\sigma_k}\right)\frac{\partial k}{\partial x_j}\right] + P_k - \rho\varepsilon \tag{3.12}$$

$$\frac{\partial \rho \varepsilon}{\partial t} + \frac{\partial}{\partial x_j}\left(\rho U_j \varepsilon\right) = \frac{\partial}{\partial x_j}\left[\left(\mu + \frac{\mu_t}{\sigma_\varepsilon}\right)\frac{\partial \varepsilon}{\partial x_j}\right] + \frac{\varepsilon}{k}\left(C_{\varepsilon 1} P_k - C_{\varepsilon 2}\rho\varepsilon\right) \tag{3.13}$$

The model constants are:

$$C_{\varepsilon 1} = 1.44 \tag{3.14}$$

$$C_{\varepsilon 2} = 1.92 \tag{3.15}$$

$$C_\mu = 0.09 \tag{3.16}$$

P_k is the turbulence production due to viscous forces:

$$P_k = \mu_t\left(\frac{\partial U_i}{\partial x_j} + \frac{\partial U_j}{\partial x_i}\right)\frac{\partial U_i}{\partial x_j} - \frac{2}{3}\frac{\partial U_k}{\partial x_k}\left(3\mu_t\frac{\partial U_k}{\partial x_k} + \rho k\right) \tag{3.17}$$

3.2.1.2 The $k-\omega$ model

The $k-\omega$ model proposes that the turbulence viscosity is related to the turbulence kinetic energy k and the turbulence frequency ω:

$$\mu_t = \rho \frac{k}{\omega} \tag{3.18}$$

Two additional transport equations will be solved for k and ω:

$$\frac{\partial \rho k}{\partial t} + \frac{\partial}{\partial x_j}\left(\rho U_j k\right) = \frac{\partial}{\partial x_j}\left[\left(\mu + \frac{\mu_t}{\sigma_k}\right)\frac{\partial k}{\partial x_j}\right] + P_k - \beta' \rho k \omega \tag{3.19}$$

$$\frac{\partial \rho \omega}{\partial t} + \frac{\partial}{\partial x_j}\left(\rho U_j \omega\right) = \frac{\partial}{\partial x_j}\left[\left(\mu + \frac{\mu_t}{\sigma_\omega}\right)\frac{\partial \omega}{\partial x_j}\right] + \alpha\frac{\omega}{k}P_k - \beta \rho \omega^2 \tag{3.20}$$

The model constants are:

$$\beta' = 0.09 \tag{3.21}$$

$$\alpha = 5/9 \tag{3.22}$$

$$\beta = 0.075 \tag{3.23}$$

$$\sigma_k = 2 \tag{3.24}$$

$$\sigma_\omega = 2 \tag{3.25}$$

The turbulence production due to viscous forces P_k is calculated in the same way as in the $k-\varepsilon$ model.

3.2.2 The Reynolds Stress Models

The Reynolds stress models do not use the eddy viscosity hypothesis. Instead the Reynolds stress model transport equations are solved for each stress components. The Reynolds averaged momentum equation for the mean velocity is:

$$\frac{\partial \rho U_i}{\partial t} + \frac{\partial}{\partial x_j}\left(\rho U_i U_j\right) - \frac{\partial}{\partial x_j}\left[\mu\left(\frac{\partial U_i}{\partial x_j} + \frac{\partial U_j}{\partial x_i}\right)\right] = -\frac{\partial p''}{\partial x_i} - \frac{\partial}{\partial x_i}\left(\rho\overline{u_i u_j}\right) + S_{M_i} \tag{3.26}$$

where $p'' = p + \frac{2}{3}\mu\frac{\partial U_k}{\partial x_k}$ is a modified pressure; $S_{M,i}$ is the sum of body forces and the fluctuating Reynolds stress contribution.

A separate transport equation must be solved for each of the six Reynolds stress components:

$$\frac{\partial \rho\overline{u_i u_j}}{\partial t} + \frac{\partial}{\partial x_k}\left[\left(\delta_{kl}\mu + \rho C_S \tfrac{k}{\varepsilon}\overline{u_k u_l}\right)\frac{\partial u_i u_j}{\partial x_l}\right] = P_{ij} - \frac{2}{3}\delta_{ij}\rho\varepsilon + \Phi_{ij} \tag{3.27}$$

where P_{ij} is the shear turbulence production term of the Reynolds stresses; Φ_{ij}

is the pressure strain tensor.

The turbulence production term is given by:

$$P_{ij} = -\rho\overline{u_i u_j}\frac{\partial U_j}{\partial x_k} - \rho\overline{u_j u_k}\frac{\partial U_i}{\partial x_k} \tag{3.28}$$

The turbulence dissipation ε transport equation now has the form:

$$\frac{\partial(\rho\varepsilon)}{\partial t} + \frac{\partial}{\partial x_k}(\rho U_k \varepsilon) = \frac{\varepsilon}{k}(C_{\varepsilon 1}P_k - C_{\varepsilon 2}\rho\varepsilon + C_{\varepsilon 1}P_{\varepsilon b}) + \frac{\partial}{\partial x_k}\left[\left(\mu + \frac{\mu_t}{\sigma_{\varepsilon RS}}\right)\frac{\partial \varepsilon}{\partial x_k}\right] \tag{3.29}$$

3.3 Combustion Modelling

In this section, the combustion model for the reacting mixture in the combustor is presented. In the present study, the fuel type for the micro gas turbine is Jet-A fuel ($C_{12}H_{23}$). This is the most common fuel for micro gas turbine applications, although bio-fuels and hydrogen have been increasingly used to achieve greener emissions and fuel flexibility. The transport equations for the combustion mode use the same algorithms for multiphase flow with additional source terms due to chemical reactions:

$$\frac{\partial(\rho Y_I)}{\partial t} + \nabla\cdot(\rho \mathbf{U} Y_I) = \nabla\left(\Gamma_{eff}(\nabla Y_I)\right) + S_I \tag{3.30}$$

where Y_I is the mass fraction for component I; S_I is the source term due to the chemical reaction rate of component I.

The chemical reactions can be described in terms of K elementary reactions involving N_C components:

$$\sum_{I=A,B,C,\ldots}^{N_C} \nu'_{kI} I \Leftrightarrow \sum_{I=A,B,C,\ldots}^{N_C} \nu''_{kI} I \tag{3.31}$$

where ν_{kI} is the stoichiometric coefficient for component I in the elementary k. The stoichiometric coefficients for reactants are denoted as ν'_{kI} and those for products as ν''_{kI}. N_C is the total number of components.

The rate of production/consumption S_I for component I can be computed as the sum of the rate of progress for all the elementary reactions in which component I participates:

$$S_I = W_I \sum_{k=1}^{K} \left(\nu''_{kI} - \nu'_{kI}\right) R_k \tag{3.32}$$

where R_k is the elementary reaction rate of progress for reaction k. W_I is the molar mass of component I.

Eddy Dissipation model is adopted in this study due to its computational efficiency and robustness. It is suitable for large scale industrial simulations as in this project, where the whole micro gas turbine needs to be simulated at various operating conditions. The eddy dissipation model is built upon the concept that chemical reaction is fast relative to the flow transport process. The model assumes that the reaction rate is proportional to the reactants mixing time, which is also proportional to the ratio of turbulent dissipation and turbulent kinetic energy:

$$reaction\ \ rate \propto \frac{\varepsilon}{k} \tag{3.33}$$

where k is the turbulent kinetic energy; ε is the rate of dissipation of turbulent kinetic energy.

In the Eddy Dissipation model, the rate of progress of elementary reaction k is determined by the smallest of the reactants and products limiters:

$$R_k = \min\left(R_{k,reactants}, R_{k,products}\right) \tag{3.34}$$

$$R_{k,reactants} = A\frac{\varepsilon}{k}\min\left(\frac{[I]}{\nu'_{kI}}\right) \tag{3.35}$$

where $[I]$ is the molar concentration of component I; and I only includes the reactant components.

$$R_{k,products} = AB\frac{\varepsilon}{k}\left(\frac{\sum_P (I) W_I}{\sum_P \nu''_{kI} W_I}\right) \tag{3.36}$$

where P loops over all product components in the elementary reaction k.

A maximum flame temperature limiter can also be applied to the Eddy Dissipation model. The reaction rate is smoothly blended to zero when the specified upper

temperature limit is approached:

$$R_{k,MFT} = A\frac{\varepsilon}{k}C_{MFT} \tag{3.37}$$

$$C_{MFT} = \max\left\{\left(T_{\max} - T\right), 0\,[K]\right\} \cdot \frac{\rho C_p}{\Delta H_R} \tag{3.38}$$

where C_{MFT} can be interpreted as a virtual concentration, which vanishes if the temperature is equal to the constrained maximum flame temperature. C_p is the specific heat capacity of the fluid mixture at constant pressure and ΔH_R is the reaction heat release per mole.

The two-step chemical kinetic mechanism of the Jet-A fuel adopted in the present work is shown below. A reduced kinetic mechanism is used to balance the cost/time of simulation against the prediction accuracy. Despite being relatively simple compared to the full kinetic mechanisms (which are also subject to several modelling uncertainties), reduced kinetic mechanisms have been shown to reproduce reasonably the key quantities of interest including heat release rates, flame temperature, and species concentration. For example, one can refer to References [50, 51, 52, 53] for previous works that adopted reduced kinetic mechanisms for Jet-A and other fuels.

$$C_{12}H_{23} + 11.75O_2 \rightarrow 12CO + 11.5H_2O \tag{3.39}$$

$$CO + 0.5O_2 \rightarrow CO_2 \tag{3.40}$$

The reaction rate is calculated based on the modified Arrhenius equation:

$$k = AT^n e^{(-E/RT)} \tag{3.41}$$

where A is the pre-exponential collision frequency factor; T is the temperature; n is the temperature exponent; E is the activation energy; R is the universal gas constant. These constants for Jet-A fuel are experimentally obtained from published documents (e.g [50]).

3.4 Droplet Breakup Modelling

Liquid Jet-A fuel is pumped via the fuel feed into the combustor. In the micro gas turbine model adopted in this study, liquid Jet-A fuel will be vaporized to gaseous Jet-A fuel. The vaporization process is simulated by the droplet breakup modelling approach. There are a few droplet breakup models to choose from in the solver ANSYS CFX. They are based on the statistical breakup approaches. In this framework, it is assumed that if a droplet breaks up into child droplets, the particle diameter is decreased accordingly to the predictions of used breakup model. The particle number rate is adjusted so that the total particle mass remains constant. With this assumption, it is not necessary to generate and track new droplets after breakup, but to continue to track a single representative particle.

In this section, these models will be described and one of the models will be chosen in a further study.

3.4.1 Taylor Analogy Breakup (TAB) Model

Firstly, the Taylor Analogy Breakup (TAB) model [54] is discussed. It is built upon the Taylor analogy, in which the droplet distortion can be described as a one-dimensional spring-mass system. TAB model assumes that the droplet velocity acts as a damping force and the surface tension acts as a restoring force. The equation of deformation motion becomes:

$$\ddot{y} = -\frac{5\mu_p}{\rho_P r^2}\dot{y} - \frac{8\sigma}{\rho_P r^3}y + \frac{2\rho_g V_{slip}^2}{3\rho_g r^2} \tag{3.42}$$

Integrating the above equation leads to the time-dependent particle distortion equation:

$$y(t) = We_C + e^{-t/t_D}\left[(y_0 - We_C)\cos\omega t + \left(\frac{y_0}{\omega} + \frac{y_0 - We_C}{\omega t_D}\right)\sin\omega t\right] \tag{3.43}$$

where:

$$t_D = \frac{2\rho_P r^2}{C_d \mu_P} \tag{3.44}$$

$$\omega^2 = \frac{C_k \sigma}{\rho_P r^3} - \frac{1}{t_d^2} \tag{3.45}$$

$$We_C = We \frac{C_f}{C_k C_b} \tag{3.46}$$

y_0 and $\dot{y}_0$ are the initial distortion and distortion rate of change. For the TAB model, y_0 and $\dot{y}_0$ are typically assumed to be zero.

If the deviation of the particle equator from its equilibrium position has become larger than half the droplet radius, breakup deems to occur. The Sauter mean radius of the child drop-lets after breakup is determined based on the energy balance between the parent and child droplets:

$$\frac{r_{p,parent}}{r_{p_child}} = 1 + 0.4K + \frac{\rho_p r_{p,parent}^3}{\sigma} \dot{y_0}^2 \left(\frac{6K-5}{120} \right) \tag{3.47}$$

The TAB model is used to determine the normal velocity of the child droplets after breakup. At the time of breakup, the equator of the parent droplet moves at a velocity of $V_N = C_v C_b r \dot{y}$ in a direction normal to the parent droplet path. This velocity is taken as the normal velocity component of the child droplets and the spray angle θ can be determined from:

$$\tan \frac{\theta}{2} = \frac{V_N}{V_{slip}} \tag{3.48}$$

The TAB model constants are:

$$C_b = 0.5 \tag{3.49}$$

$$C_d = 5.0 \tag{3.50}$$

$$C_f = 1/3 \tag{3.51}$$

$$C_k = 8.0 \tag{3.52}$$

$$C_v = 1.0 \tag{3.53}$$

$$K = 10/3 \tag{3.54}$$

3.4.2 Enhanced Taylor Analogy Breakup (ETAB) Model

An improved version of the TAB model is the Enhanced Taylor Analogy Breakup (ETAB) model introduced by Tanner [55]. This model uses the same droplet distortion mechanism as the standard TAB model, but with a different relation for the description of the breakup process. In the ETAB model, the rate of child droplet generation is assumed to be proportional to the number of child droplets:

$$\frac{d}{dt}n(t) = 3K_{br}n(t) \tag{3.55}$$

The constant K_{br} depends on the breakup regime:

$$K_{br} = \begin{cases} k_1\omega, & \text{if } We \leq We_t \\ k_2\omega\sqrt{We}, & \text{otherwise} \end{cases}$$

where, We_t is the Weber number that divides the bag breakup regime from the stripping breakup regime.

Assuming a uniform droplet size distribution, the ratio of child to parent droplet radii can be derived:

$$\frac{r_{p,child}}{r_{p,parent}} = e^{-K_{br}t} \tag{3.56}$$

The child droplets inherit a velocity component normal to the path of the parent droplet with a value:

$$V_N = A\dot{x} \tag{3.57}$$

where A is a constant that is determined from an energy balance consideration:

$$A^2 = 3\left[1 - \frac{r_{p,parent}}{r_{p,child}} + 5C_D We/72\right]\frac{\omega^2}{\dot{y}^2} \tag{3.58}$$

with

$$\omega^2 = \frac{C_k\sigma}{\rho_p r_{p,parent}} \tag{3.59}$$

and C_D is the parent droplet drag coefficient at breakup.

The TAB model has been observed to often predicts a too small ratio of child to

parent droplet. This is mainly caused by the assumption that the initial deformation parameters y_0 and $\dot{y}_0$ are zero upon injection, which may lead to far too short breakup times. The largely underestimated breakup times in turn lead to an underprediction of global spray parameters such as the penetration depth and the cross-sectional droplet size distribution. In the ETAB model, Tanner proposed to set the initial value of the rate of droplet deformation $\dot{y}_0$ to:

$$\dot{y}_0 = [1 - We_c\,(1 - \cos \omega t_{bu})]\,\frac{\omega}{\sin \omega t_{bu}} \tag{3.60}$$

The initial droplet deformation is still kept as zero $y_0 = 0$.

t_{bu} is determined as:

$$t_{bu} = C\sqrt{\frac{\rho_P}{\rho_F}}\frac{d_{P,0}}{V_{P,0}} \tag{3.61}$$

where $C = 5.5$.

Setting $\dot{y}_0$ to a negative number delays the first breakup of the large initial droplets and to extend their life span, which results in a more accurate simulation of the jet breakup.

The ETAB model constants are:

$$K_1 = 2/9 \tag{3.62}$$

$$K_2 = 2/9 \tag{3.63}$$

$$We_t = 80 \tag{3.64}$$

Besides the TAB and ETAB models, there are several other droplet breakup models such as the Cascade Atomization and Breakup (CAB) [56], the Reitz and Diwakar model [57], etc. Wahba and Nawar [58] compared predictions of several droplet breakup models for validation against experiments by Sedarsky et al. [59] and Liu et al. [60] as well as their own studies in a gas turbine system. In their study, the ETAB model consistently showed the least deviation from experimental measurements. Therefore, the ETAB model is chosen in this study.

3.5 Soot Modelling

Besides the aerothermal performance of the micro gas turbine, its emission characteristics are of interest. In this section, modeling of soot formation is described. The Magnussen soot model [61] will be adopted. In this model, soot is assumed to form from a gaseous fuel in two stages: the formation of radical nuclei and the formation of soot particles from these nuclei. Extra transport equations need to be solved for soot modelling:

$$\frac{\partial\left(\bar{\rho}\widetilde{X_N}\right)}{\partial t}+\nabla\cdot\left(\bar{\rho}\mathbf{U}\widetilde{X_N}\right)=\nabla\widetilde{X_N}\left(\bar{\mu}+\frac{\mu_t}{Pr_t}\right)+\tilde{S}_{nuclei,f}+\tilde{S}_{nuclei,c} \tag{3.65}$$

$$\frac{\partial\left(\bar{\rho}\widetilde{Y_S}\right)}{\partial t}+\nabla\cdot\left(\bar{\rho}\mathbf{U}\widetilde{Y_S}\right)=\nabla\widetilde{Y_S}\left(\bar{\mu}+\frac{\mu_t}{Pr_t}\right)+\tilde{S}_{soot,f}+\tilde{S}_{soot,c} \tag{3.66}$$

where X_N is the specific concentration of radical nuclei; Y_S is the soot mass fraction.

The modelling procedures comprise of three independent parts:

- Formation of nuclei and soot particles according to Tesner et al. model [62]
- Combustion of nuclei and soot particles
- Magnussen's Eddy Dissipation Concept for modelling the effect of turbulence on mean reaction rates [61]

Formation of nuclei and soot particles is computed from Tesner et al.'s empirical models [62]. The source terms are calculated from the particle number concentrations for nuclei C_N and soot particles C_S:

$$C_N=\rho\times A\times X_N \tag{3.67}$$

$$C_S=\rho\frac{Y_S}{m_p} \tag{3.68}$$

where the Avogadro's number is $A=6.02214199e23$.

m_p is the mass of a soot particle and is given by:

$$m_p = \rho_{soot} \pi d^3/6 \tag{3.69}$$

where ρ_{soot} is the density of the soot particle; d is the mean diameter of the soot particles.

Thus, the source terms for nuclei and soot formation can be modelled as:

$$\widetilde{S}_{nuclei,f} = n_0 + (f-g) C_N - g_0 C_N C_S \tag{3.70}$$

$$\widetilde{S}_{soot,f} = m_p (a - bC_S) C_N \tag{3.71}$$

n_0 is the spontaneous formation of radical nuclei from the fuel. It is modelled using the Arrhenius approach:

$$n_0 = a_0 f_c \rho Y_{fuel} \exp\left(-T_{A,0}/T\right) \tag{3.72}$$

where f_c is the mass fraction of carbon in the fuel material; f is the chain branching coefficient; g is the chain termination coefficient; g_0 is the linear termination coefficient of radical nuclei on the soot particles.

The model constants are provided as below in the particle number [part] physical dimensions:

$$\rho_{soot} = 2000 \left[kg/m^3\right] \tag{3.73}$$

$$d = 1.785e-8 \, [m] \tag{3.74}$$

$$a_0 = 1.35e37 \, [part/kg/s] \tag{3.75}$$

$$T_{A,0} = 90000 \, [K] \tag{3.76}$$

$$f - g = 100 \, [1/s] \tag{3.77}$$

$$g_0 = 1e-15 \left[m^3/s/part\right] \tag{3.78}$$

$$a = 1e5 \, [1/s] \tag{3.79}$$

$$b = 8e-14\left[m^3/s/part\right] \tag{3.80}$$

The source terms of combustion nuclei $\widetilde{S}_{nuclei,c}$ and soot particles $\widetilde{S}_{soot,c}$ are calculated from the fuel consumption rate $\widetilde{S}_{fuel}$ in $[kg/m^3/s]$ as:

$$\widetilde{S}_{nuclei,c} = \widetilde{S}_{fuel}\frac{\widetilde{X}_N}{\widetilde{Y}_{fuel}} \tag{3.81}$$

$$\widetilde{S}_{soot,c} = \widetilde{S}_{fuel}\frac{\widetilde{Y}_S}{\widetilde{Y}_{fuel}} \tag{3.82}$$

Chapter 4

Dump Diffuser Combustor

4.1 Introduction

A typical gas turbine combustor consists of a pre-diffuser, a casing annulus, and a flame tube. One of the main task of a combustor is to reduce the velocity of incoming air to generate favourable conditions for flame sustaining. However, parasitic total pressure loss is unavoidable throughout this process. Minimizing the total pressure loss whilst maximizing static pressure gain across the pre-diffuser has always been a primary concern of the combustor designer, although it is not rare that some certain aspects have to be compromised to achieve the best overall performance. Among the combustor architecture, the dump diffuser is a popular design choice due to its superiority in flow deceleration at the cost of some extra total pressure loss. As a result, the performance of the diffuser combustor has been investigated by various researchers.

Honami et al. [63] studied the effect of flame dome depth on the total pressure performance and flow behaviour. The inclined combustor wall was found to be the most effective configuration for a range of inlet flow conditioning. Carrotte et al. [64] compared the datum configuration with further three geometries, in which the distance between the pre-diffuser exit and the dome head was reduced. High values of total pressure loss was found to correlate with the short dump gap, i.e. the pre-diffuser exit is closer to the dome head. Ghose et al. [65] studied the effect of the pre-diffuser angles and the dump gap on the static pressure recovery. Dump gap was found to

have a significant effect in configurations with small pre-diffuser angles. Rahim et al. [66] investigated the effects of dome shapes on the recirculation zone and flow uniformity. The hemispherical dome liner was shown to perform better in comparison with two other tested dome shapes (ellipsoidal and vertical ellipsoidal). Carrotte et al. [67] presented test data for a dump and a short faired combustor diffuser system. The dump diffuser induced flow separation at pre-diffuser exit, although the recirculation loss was eliminated using the faired diffuser. On the other hand, the faired diffuser was more susceptible to aerodynamic instabilities. Walker et al. [37] examined the effects of three dump gap ratio levels, while keeping other geometries the same. They demonstrated that the component interaction decreases as the dump gap increases, provided that the cowl flow is fixed. He et al. [68] investigated a dump diffuser system with large liner depth ratio and high dome flow rate in the representative geometry of a modern lean-burn combustor. The loss coefficient was found to decrease as dump gap increased. Dump gap ratio in the range of 1.2 to 2.8 was found to have a relatively low loss coefficient compared to other configurations. Fishenden and Stevens [69] were amongst the earliest researchers investigating the effects of an annular combustor-dump diffuser geometry including the pre-diffuser, flame tube, and the surrounding annuli. Srinivasan et al. [70] parametrically studied the effects of the dump gap dimension, the flow split, and the combustor channel height. The study found that the performance improved with the dome flow rate or the dump gap dimension. For a general understanding of flow phenomena in the combustor diffuser system, as well as the problems faced by the combustor designer, one is recommended to read the review by Klein [71]. The majority of previous studies in combustion performance have used clean flow conditioning at the inlet, i.e. the inlet flow is assumed to be uniform except for a few studies in which the interaction is the main subject of interest [72, 73, 74, 36]. Barker and Carrotte [72] performed the experiment on an annular test rig to study the effects of non-uniformities in the diffuser system. They concluded that the OGV wakes could pass through the dump cavity, such that the non-uniform pressure distribution was observed near the flame tube fuel injectors. Walker et al. [73] investigated the pre-

diffuser design approach for an aero-derivative land-based gas turbine using various numerical configuration fidelities, namely a 2D axisymmetric model with two outlets, a 3D model with two outlets, and a 3D model with three outlets (the extra outlet coming from the inclusion of the fuel injector flow). The 2D axisymmetric model was used extensively to provide a relatively quick and easy method of exploring various concepts. However, they also noted that the non-uniform pitchwise inlet conditions were missing in the 2D axisymmetric model, thus prompted Walker and his colleagues to further investigate the 3D models with more realistic flow features. Klein et al. [74] conducted an experiment on the effects of wakes at the compressor cascade exit. They found that the losses of the short annular dump-diffuser type combustor system increased significantly with the distance between the cascade and the diffuser system. Walker et al. [36] reported an experimental work on the interactions between the combustor aerodynamics and upstream components. They demonstrated that the cowl flow non-uniform variation could propagate upstream and further induced non-uniform variation amongst the compressor rows. In addition, the diffuser seemed to be more susceptible to separation at high injector flow rates. One therefore should not be surprised that the combustor system inlet flow can be subjected to a more complicated flow field from the compressor blade-row exit, which in turn can possibly trigger the early onset of flow instability within the pre-diffuser. The exit flow field of the compressor is non-uniform due to presence of wakes from upstream blade-row as well was the radial load bearing struts within the diffuser. In a linear cascade, the passage vortex forms due to the pressure gradient between the pressure surface of the reference blade and the suction surface of the adjacent blade and travels downstream. Due to the size of this vortex, the flow field entering the pre-diffuser inlet is no longer uniform. In a realistic compressor bladerow, the flow field is even more complicated with the passage vortex near the casing as well as the hub walls. The wakes from upstream bladerow will also convect downstream towards to the pre-diffuser inlet.

Having discussed about various past researches from the literature, it is evident that the effects of the dump diffuser combustor system geometry have been investigated extensively. On the other hand, the interactions between components as well as the investigations with a non-uniform inlet conditioning have been studied less often. The number of reports on the design approach for the case with non-uniform inlet conditioning is even more limited. However, due to the emerging popularity of the lean burn combustor, the component-to-component interactions will be likely more prominent. Thus, in the present chapter, the aerodynamics performance of the dump diffuser combustor system is of interest. Firstly, the validation test case of an asymmetric diffuser will be investigated and compared with the available experimental results. Then the effects of geometrical parameters such as the pre-diffuser divergence angle and the dump gap ratio will be investigated. In the second part of the study, the inlet conditioning will be perturbed to reflect the stronger effects of component-to-component interactions as mentioned before. Within this part, a symmetrical and asymmetrical incoming boundary layer with different thickness will be varied parametrically.

4.2 Validation of an Asymmetric Diffuser

For validation purposes, an asymmetric diffuser test case will be investigated first and compared with the available experimental results. The test case geometry is a two-dimensional diffuser with one side of the channel diverging from the inlet down to the exit. Figure 4.1 shows the detailed dimensions of the asymmetric diffuser test case. The chosen test case has been a popular choice of numerical validations for both Reynolds averaged Navier-Stokes (RANS) based model and Large Eddy Simulation (LES) model [75, 76] since the publication of its experimental results [77, 9].

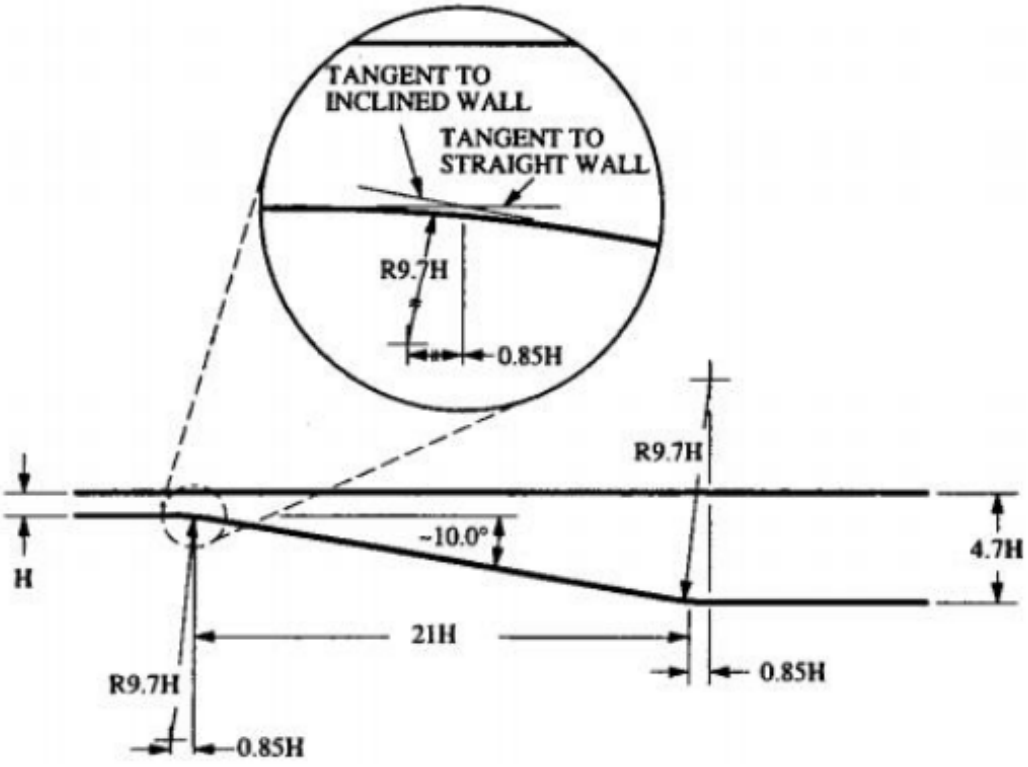

Figure 4.1: Illustration of the asymmetric diffuser test case geometry, reproduced from [9].

The asymmetric diffuser test case has the characteristics of flow separation and subsequent reattachment after the expansion region due to the inclined wall. As a result, a separation bubble forms on one side of the diffuser wall. Such physical phenomena are difficult to predict especially with RANS-based turbulence models because the separating and reattaching boundary layers are highly unstable. Nevertheless, this validation test case shares many similar flow characteristics that one would expect to observe in the annular dump diffuser combustor (the main topology of interest in the current work), namely turbulent flow separation and reattachment. Thus, it is necessary to first validate a suitable solver scheme as well as the choice of an appropriate turbulence model.

Figure 4.2 presents the overview mesh as well as the zoom-in mesh at the expansion region where the inclined wall originates. The mesh is unstructured hexahedral with clustered elements near the diffuser walls.

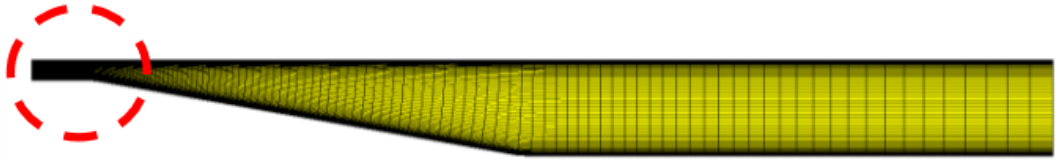

(a) Mesh overview.

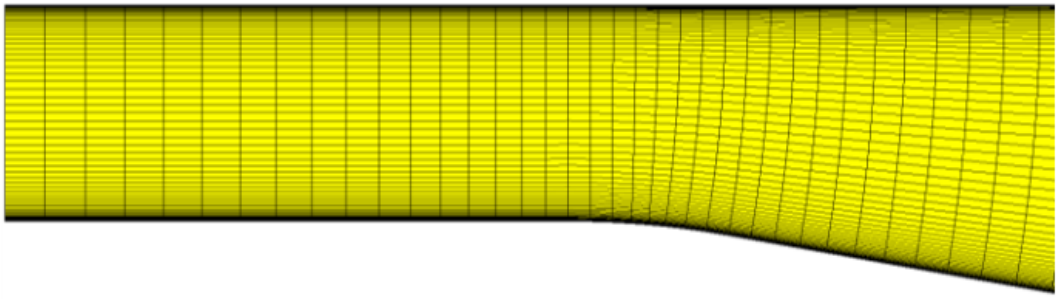

(b) Mesh closeup at the expansion region.

Figure 4.2: Mesh of the asymmetric diffuser test case.

The asymmetric diffuser test case computation is carried out with a given velocity profile at the inlet and atmospheric static pressure at the outlet. Figure 4.3 shows the comparison between the experimental results and the numerical results computed from various RANS-based turbulence models at the location of 12H (H is the diffuser inlet height, see Figure 4.1). It can be seen that the SST model predicts the best agreement with the experimental results among the investigated turbulence models. The standard $k-\varepsilon$ model and the RNG $k-\varepsilon$ model give a similar prediction, in which the separation zone on the diffuser wall (low vertical coordinate Y) has not been predicted. This observation means that the standard and the RNG $k-\varepsilon$ model predict the formation of separation zone more rearward than what was recorded in the experiment. Moreover, the velocity profiles predicted by those models seem to shift towards the inclined diffuser wall. The use of the EARSM $k-\varepsilon$ model has improved the shape of the velocity profile. Although the formation of separation zone is still not predicted correctly by the EARSM $k-\varepsilon$ model, it shows a significant improvement near the inclined wall compared to other ε-based models. Thus, the SST model will be chosen for subsequent investigations of the annular dump diffuser combustor due to its superiority in the predictive capability of flow separation and reattachment compared to the ε-based models.

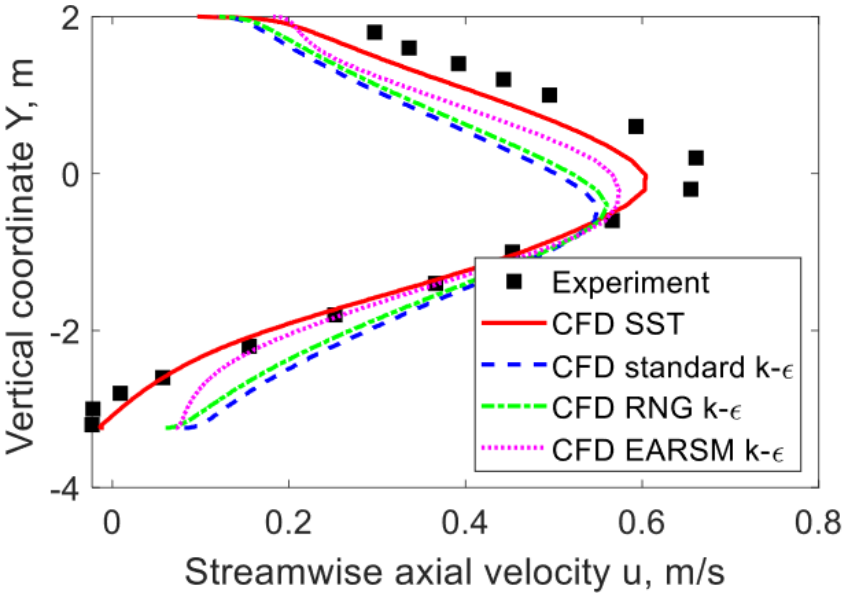

Figure 4.3: Comparison of streamwise velocity profiles obtained from the experiment and various RANS turbulence model.

4.3 Annular Dump Diffuser Combustor Geometrical Model

A typical simplified geometry of the annular dump diffuser combustor is adopted. The combustor model comprises of a straight-walled pre-diffuser, a dump gap, an inner annulus, and an outer annulus. Figure 4.4 illustrates the considered geometry and its geometrical parameters. This is a typical configuration that can be found in various researches [78, 68]. Table 4.1 presents the values and descriptions of the fixed geometrical parameters of the dumped diffuser configuration. The inner divergence angle θ_i is the angle between the inner diffuser wall and the ground. Similarly, the outer divergence angle θ_o is defined as the angle between the outer diffuser wall and the ground. Also depicted in Figure 4.4 is the dump gap, which is the distance between the diffuser outlet and the dome. The dump gap is represented by the ratio between the dump distance D and the diffuser outlet height h_2.

In the parametric studies, the inner and outer divergence angles θ_i and θ_o will be varied to study the effects of diffuser angle. In addition, the dump gap D will also be changed to investigate the effects of dump gap ratio $\frac{D}{h_2}$.

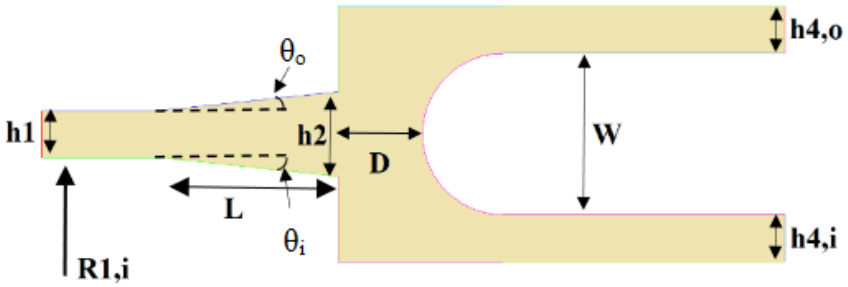

Figure 4.4: Simplified geometrical model of the annular dump diffuser combustor.

Parameters	Units	Values
Inlet height h_1	m	0.028
Inlet inner radius $R_{1,i}$	m	0.156
Flame tube depth W	m	0.0956
Inner annulus height $h_{4,i}$	m	0.028
Outer annulus height $h_{4,o}$	m	0.028

Table 4.1: Dump diffuser fixed geometrical parameters.

4.4 Annular Dump Diffuser Combustor Numerical Model Setup

4.4.1 Boundary conditions

The simulations have been carried out using the total pressure, total temperature, and flow angle at the inlet boundary conditions. At the outlet boundary, the static atmospheric pressure is used. The combustor inner and outer annulus casing are modelled as an adiabatic no-slip wall. The axisymmetric periodicity is applied at the two side interfaces, representing the truncated domain of the dump diffuser combustor geometry. These boundary conditions correspond to a simple experimental rig condition, as if the combustor geometry would be tested in a low-speed blow-down type wind tunnel. This makes the findings in the current work can be easily replicated and confirmed in a typical laboratory-sized wind tunnel.

4.4.2 Mesh sensitivity study

The computational domain is divided into seven blocks for optimum control of the mesh. It consists of each block for: a straight-walled inlet duct, angled pre-diffuser, dump gap, inner and outer dump diffuser corner, and inner and outer flame tube

annulus. Meshing is carried in ICEM to generate unstructured hexahedral mesh. The mesh quality is consistently checked to avoid highly skewed and high aspect ratio elements. The elements near the solid wall boundaries are refined to capture the boundary layer effect. The growth rate of element size is set to be 1.2 to ensure gradual expansion of adjacent cells. The final mesh size has about 21,000 elements in a 2D model. Figure 4.5 presents the 2D mesh for the annular dump diffuser computation. Clustered mesh near the walls can be observed, thus confirms the suitability of the resolved boundary layer region.

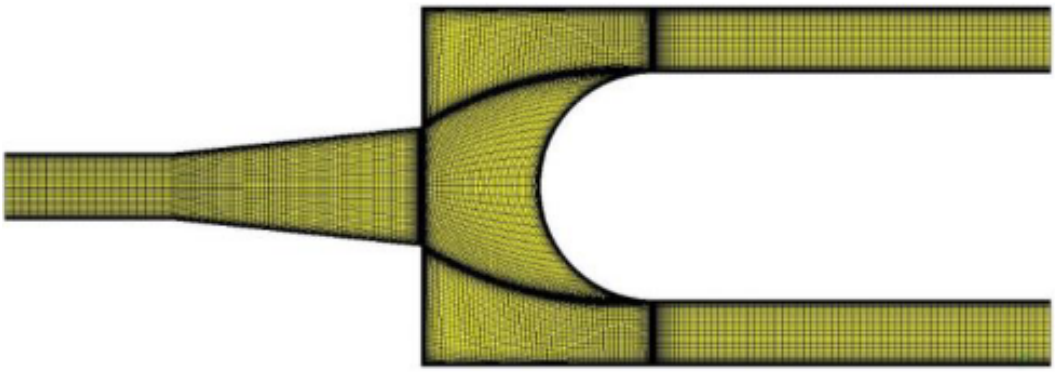

Figure 4.5: Two-dimensional mesh of the annular dump diffuser combustor model.

Mesh sensitivity study is carried out to ensure the chosen mesh level is sufficient to capture the relevant physics. A too coarse mesh is able to over-simplify the captured flow physics, while a too fine mesh is not desirable due to expensive computational resources. Figure 4.6 shows the results of mesh sensitivity study for three levels of mesh for a 2D configuration: coarse (5,500 elements), medium (21,000 elements), and fine (86,000 elements). As can be seen, the medium mesh provides a rather close prediction of the performance coefficients to the fine mesh. Therefore, the mesh sensitivity converges and the medium mesh level is sufficient for this study.

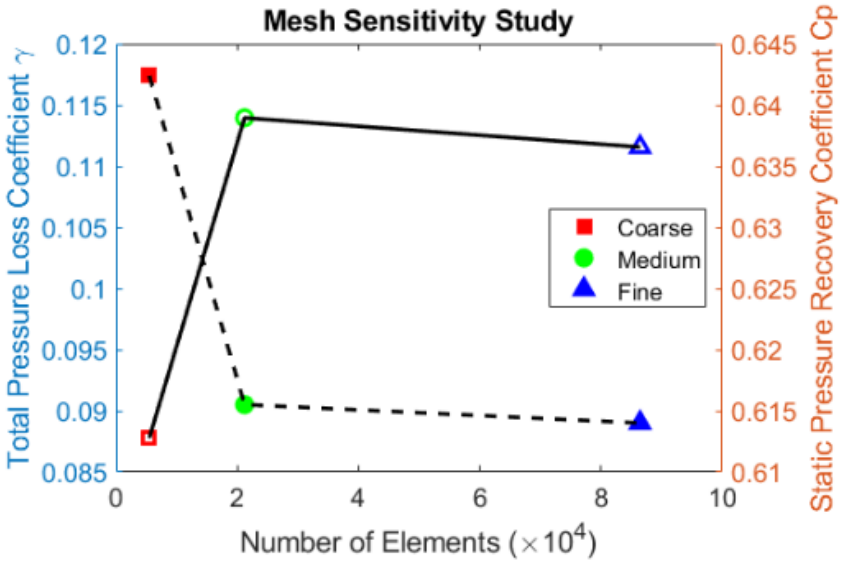

Figure 4.6: Mesh sensitivity study results of three mesh levels (– total pressure loss coefficient λ; — static pressure recovery coefficient C_p).

4.4.3 Data reduction

In the present work, the aerodynamics performance of the annular dump diffuser combustor is of interest. Two parameters are recorded and compared, namely the static pressure recovery coefficient C_p and the total pressure loss coefficient λ. These coefficients are calculated based on the measurement at the diffuser inlet and outlet. The coefficients are normalized with respect to the inlet dynamic head. Mass-averaged static pressure and total pressure are used for calculation. The formula for the calculation of static pressure recovery coefficient C_p is defined as in Equation 4.1:

$$C_p = \frac{m_{outlet}\bar{P}_{outlet} - m_{inlet}\bar{P}_{inlet}}{0.5 m_{inlet} V_{inlet}^2} \tag{4.1}$$

where m_{inlet} and m_{outlet} are mass flow at the inlet and outlet stations; $\bar{P}_{inlet}$ and $\bar{P}_{outlet}$ are averaged static pressure at the inlet and outlet stations.

In a similar manner, the total pressure loss coefficient λ is defined as:

$$\lambda = \frac{m_{inlet}\bar{P}_{0,inlet} - m_{outlet}\bar{P}_{0,outlet}}{0.5 m_{inlet} V_{inlet}^2} \tag{4.2}$$

where total pressure $P_0 = P + 0.5\rho v^2$; P is static pressure; ρ is density; v is fluid

velocity.

Note the difference in the nominator between Equation 4.1 and 4.2, i.e. the total loss is defined as the difference between the inlet station and the outlet station, denoting that stagnation pressure drop across the diffuser due to parasitic loss (due to boundary layer development, flow separation, etc). On the other hand, the static pressure rises across the diffuser due to the flow expansion. This velocity diffusion is the key enabler of flame stabilization.

4.5 Annular Dump Diffuser Combustor Clean Inflow

4.5.1 Basic aerodynamic of the dump diffuser combustor

The basic aerodynamics characteristics of the annular dump diffuser will be discussed first. Figure 4.7 shows the streamlines within an annular dump diffuser. There are two large vortices at the upper and lower corners, which is a result of the sudden expansion from the angled diffuser to the dump gap. Most of the flow is bent and fed to the flame tube annuli, while the rest contributes to the formation of vortices.

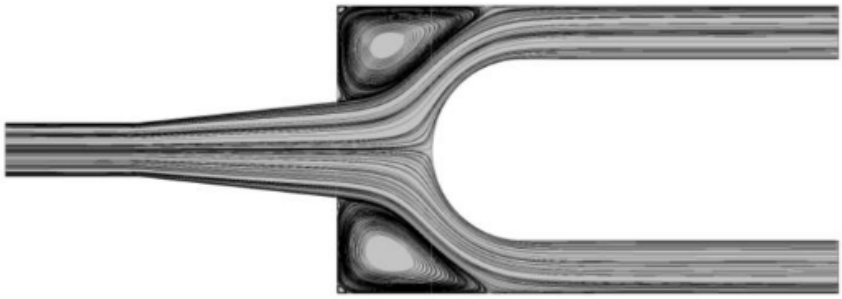

Figure 4.7: Flow streamlines of the annular dump diffuser combustor.

Figure 4.8 presents the enlarged vector field near the upper corner of the annular dump diffuser. The main vortex rotates counter-clockwise (denoted as red arrow) when the flow expands from the pre-diffuser outlet to the outer flame tube annuli. There are two vortices of much smaller size (denoted as blue circle) at the sharp expansion of the pre-diffuser and at the top left corner of the dump diffuser. The former vortex is formed by the sharp and sudden expansion flow. The latter vortex is formed by the interaction of the main vortex with the corner walls. However, these

two vortices are much smaller than the main vortex, thus their influences on the combustor performance should be negligible compared to the main vortex.

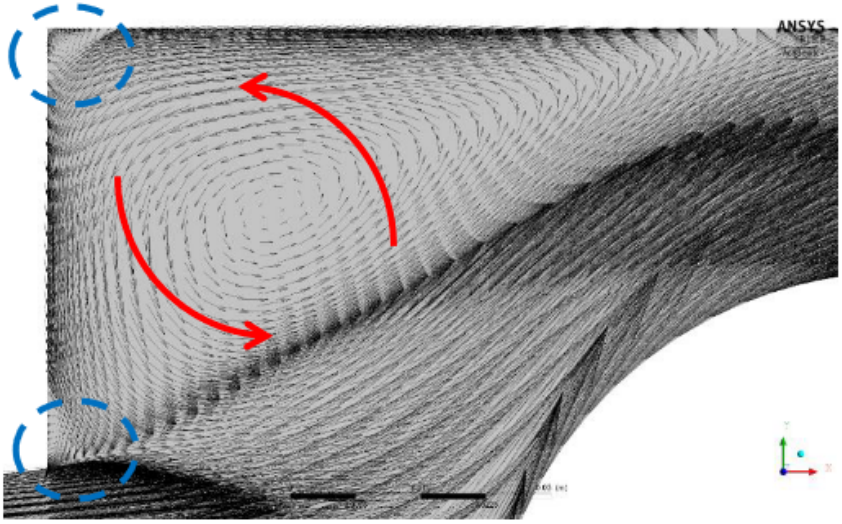

Figure 4.8: Flow vector of the annular dump diffuser combustor.

Figure 4.9 presents the total pressure loss coefficient contour of the annular dump diffuser. The main sources of loss are attributed to the two vortices at the corner dump gap. The total pressure loss can be seen to convect downstream of the flame tube annuli along the combustor walls. As a result, the flow at the flame tube annuli outlet is highly skewed.

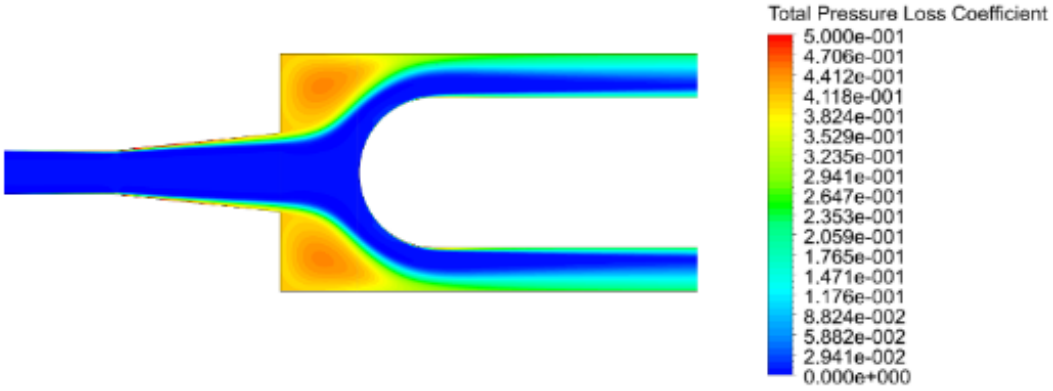

Figure 4.9: Total pressure loss contour of an annular dump diffuser combustor.

4.5.2 Effect of diffuser angle

Having examined the basic aerodynamics features of the dump diffuser combustor, we further explore the effects of the geometrical parameters on its performance. In this section, the inner and outer divergence angles θ_i and $theta_o$ are chosen for the parametric study. Four combinations of the inner and outer divergence angles used in this investigation is shown in Table 4.2.

θ_i	θ_o	**Mean diffuser angle =** $0.5 \times (\theta_o - \theta_i)$
6^0	6^0	0^0
4^0	7.5^0	1.75^0
2^0	9^0	3.5^0
0^0	10.5^0	5.25^0

Table 4.2: Investigated diffuser angle configurations.

The diffuser angles are chosen such that the pre-diffuser is gradually skewed upwards to increase the mean diffuser angle, which is defined as the average of the difference between the outer and inner divergence angle. Figure 4.10 shows the effect of mean diffuser angle on the static pressure recovery coefficient, whereas Figure 4.11 presents that on the total pressure loss coefficient. The figures also compare the results for three different values of dump gap ratio.

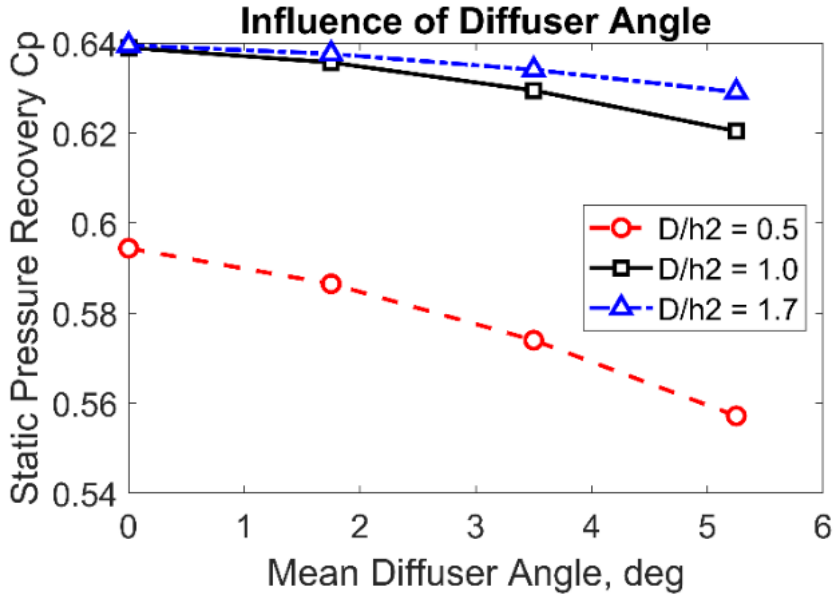

Figure 4.10: Flow streamlines of the annular dump diffuser combustor.

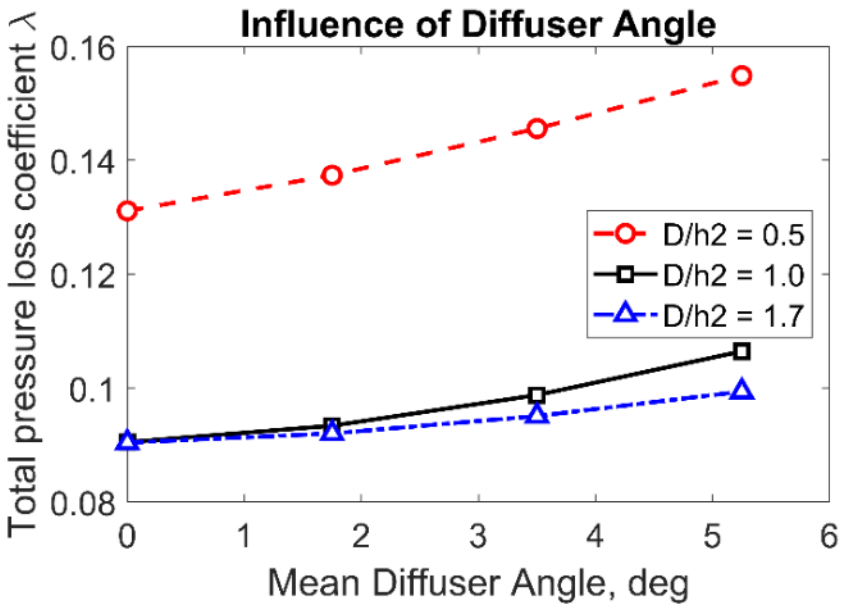

Figure 4.11: Flow streamlines of the annular dump diffuser combustor.

It can be seen that the static pressure recovery coefficient C_p decreases as the mean diffuser angle increases at all investigated dump gap ratio (Figure 4.10). However, the rate of static pressure recovery coefficient reduction decreases as the dump gap ratio increases. On the other hand, the rate of total pressure loss coefficient rise λ decreases as the dump gap ratio increases (Figure 4.11). Figure 4.12 further presents the total pressure loss contour for the considered configurations with different combination of diffuser angles. As the pre-diffuser is skewed outwards due to an increase in the mean diffuser angle, the vortex in the inner dump gap corner gradually incurs more loss (e.g. Figure 4.12d compared to Figure 4.12a). This is attributed to an increase in flow turning required for the flow to bend and feed to the inner flame tube annuli. Therefore, the total pressure loss of the whole system rapidly increases when the mean diffuser angle increases. As a result, the curved/canted pre-diffuser is generally not favourable due to low static pressure recovery coefficient and high total pressure loss. However, this is sometimes inevitable because the mechanical cant is necessary to bridge the gap between the compressor and turbine radius. This adverse effect can be diminished by using a higher dump gap ratio at the cost of increasing the overall length of the combustor system.

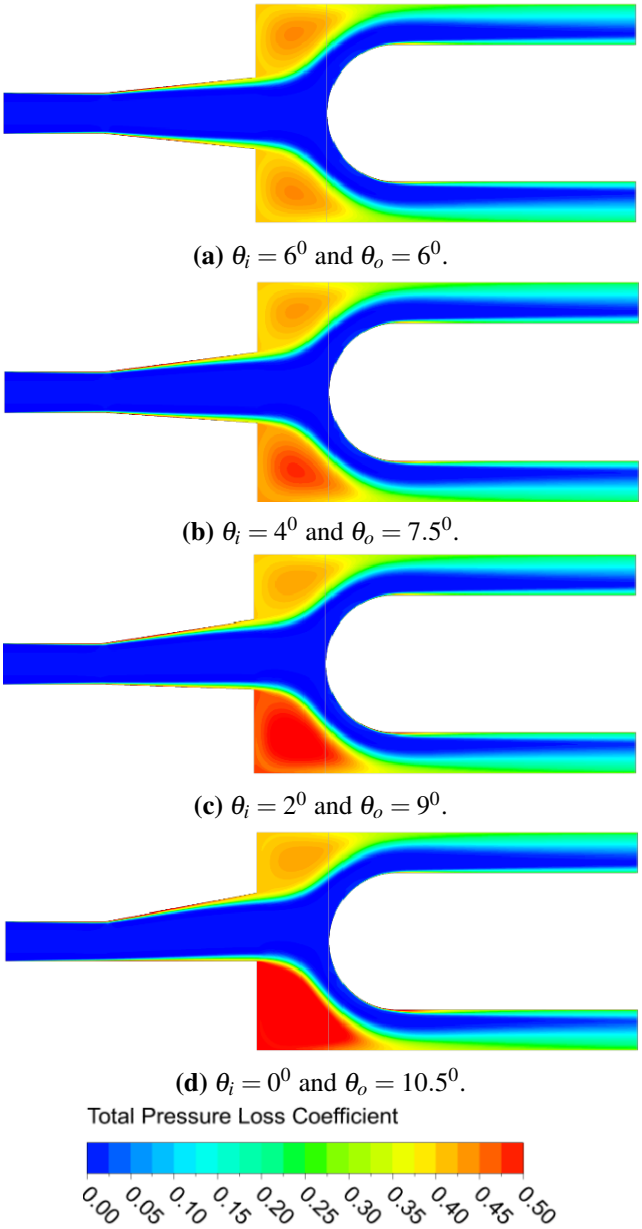

(a) $\theta_i = 6^0$ and $\theta_o = 6^0$.

(b) $\theta_i = 4^0$ and $\theta_o = 7.5^0$.

(c) $\theta_i = 2^0$ and $\theta_o = 9^0$.

(d) $\theta_i = 0^0$ and $\theta_o = 10.5^0$.

Figure 4.12: Total pressure loss contours for different diffuser angles at nominal dump gap ratio ($\frac{D}{h_2} = 1$).

4.5.3 Effect of dump gap ratio

In this section, the dump gap ratio is the chosen parameter of interest to explore the effects of geometrical parameters. Three values of dump gap ratio will be used in this study: $\frac{D}{h_2}$ = 0.5, 1.0, and 1.7. Similarly to the previous study, the computational results at different values of mean divergence angle will also be presented to investigate the trend.

Figure 4.13 shows the effect of dump gap ratio on the static pressure recovery coefficient C_p, whereas Figure 4.14 presents the effect of dump gap ratio on the total pressure loss coefficient λ. It can be observed that the static pressure recovery coefficient increases as the dump gap ratio increases for all mean diffuser angle configurations. On the other hand, the total pressure loss coefficient decreases as the dump gap ratio increases. The rate of change in performance parameters between the dump gap ratio $\frac{D}{h_2} = 0.5$ and $\frac{D}{h_2} = 1.0$ is drastic, whereas the rate of change from dump gap ratio $\frac{D}{h_2} = 1.0$ to $\frac{D}{h_2} = 1.7$ is mild.

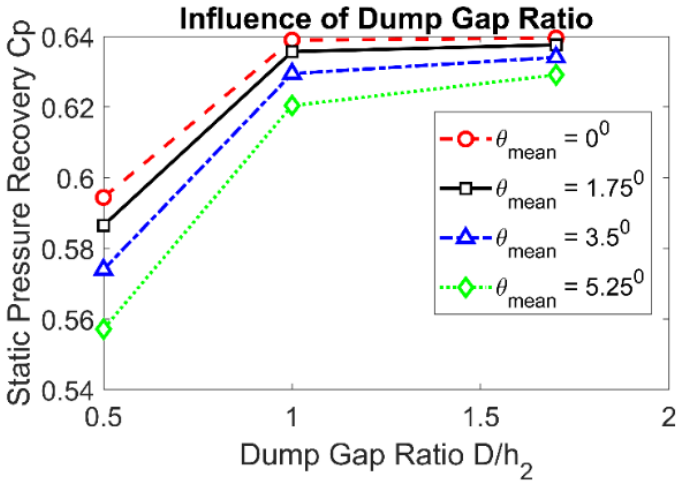

Figure 4.13: Effect of dump gap ratio on the static pressure recovery coefficient C_p with various mean diffuser angles.

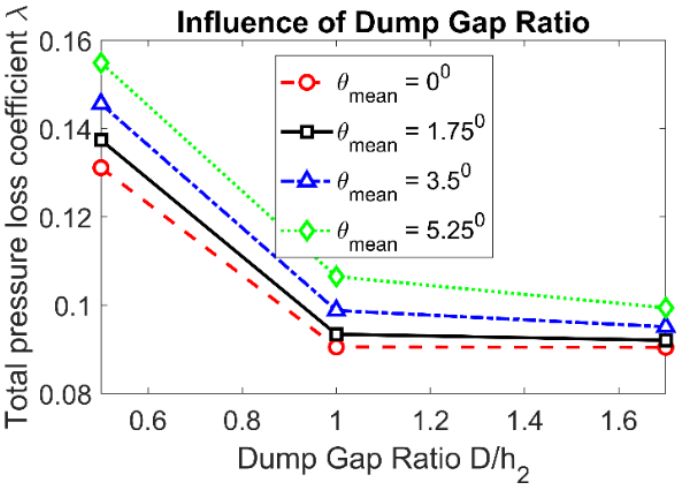

Figure 4.14: Effect of dump gap ratio on the total pressure loss coefficient λ with various mean diffuser angles.

Figure 4.15 further presents the total pressure loss contour for the considered configurations with different dump gap ratio. As the dome is closer to the pre-diffuser exit due to the reduction in the dump gap ratio, the vortex in the inner dump gap corner incurs a more significant loss (e.g. Figure 4.15a). This is attributed to an increase in flow curvature that forces the expanded flow to quickly feed to the flame tube annuli. Therefore, the total pressure loss of the whole system rapidly increases when the dump gap ratio decreases. As a result, the very low dump gap configuration (e.g. Figure 4.15a) is not favourable due to low static pressure recovery coefficient and high total pressure loss despite of the much shorter overall length. On the other hand, the high dump gap ratio (e.g. Figure 4.15c) does not also show any significant improvement in the aerodynamics performance. It only stretches the dump gap vortices without affecting much the level of total pressure loss. Hence, there exists an optimum value of dump gap ratio that gives a good amount of aerodynamics performance without incurring a high overall length of the combustor system.

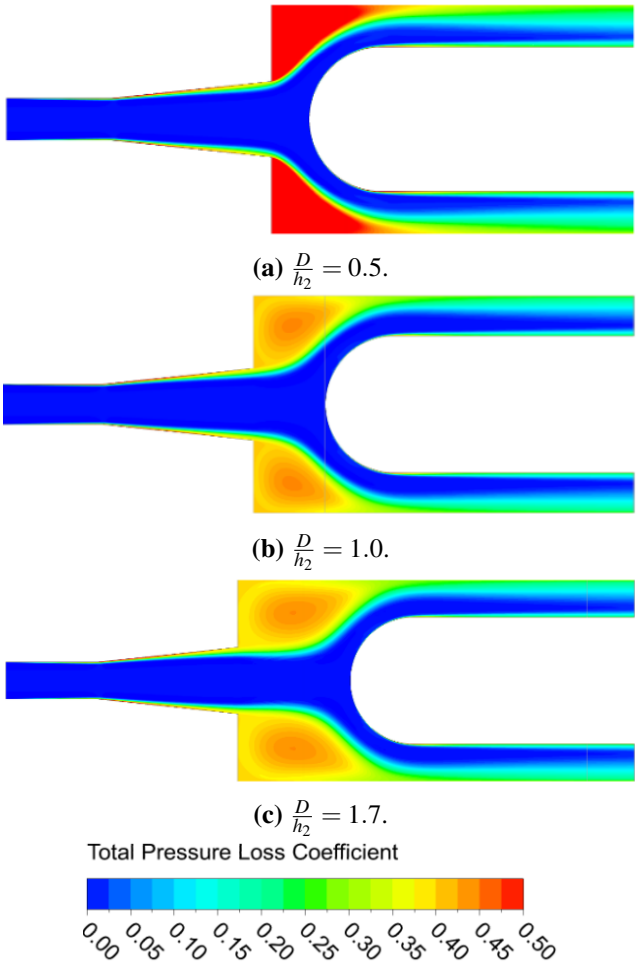

(a) $\frac{D}{h_2} = 0.5$.

(b) $\frac{D}{h_2} = 1.0$.

(c) $\frac{D}{h_2} = 1.7$.

Figure 4.15: Total pressure loss contour for different dump gap ratio at nominal diffuser angle ($\theta_i = 6^0$ and $\theta_o = 6^0$).

4.6 Annular Dump Diffuser Combustor Non-Uniform Inlet

4.6.1 Effects of boundary layer thickness

At the compressor blade row inlet, the boundary layer thickness can vary between 5% and 40% of the blade span [79]. Downstream the compressor blade row, the boundary layer thickness increases due to the formation of secondary flow. Because the outlet guide vane (OGV) blade row just before the dump diffuser combustor system is typically short, the ratio of the boundary layer thickness to the OGV blade span is therefore rather high. As a result, the dump diffuser combustor system would have to experience a strong non-uniform inflow with a rather thick boundary layer. Nevertheless, in the previous computational investigation, the simulations were carried out using a clean inflow conditioning, i.e. the inlet velocity profile is constant in the radial direction. As discussed before, in a more realistic conditions, there will be always a boundary layer of different thicknesses due to the incoming boundary layer from the compressor blade row upstream. However, it is also noted that the exact thickness and state of the incoming boundary layer is hardly known in real machines. In a simple rig test, this can be roughly determined. The inlet boundary layer thickness and state has been seen to affect the turbomachinery performance significantly [80, 81].

In the second part of the current work, simulations will be carried out with a non-uniform inlet conditioning, which takes into account the radial distribution of the incoming inlet velocity. The velocity profile is set up assuming the collateral velocity relationship, determined by the following equation:

$$\frac{v^*}{V} = \left(\frac{y}{\delta}\right)^{1/7} \tag{4.3}$$

where v^* is the local velocity in the boundary layer; V is the freestream velocity; y is the local distance in the boundary layer; δ is the thickness of the boundary layer.

Figure 4.16 shows the comparison for the inlet velocity profile with different boundary layer thickness considered. It can be observed that the region of low near-wall velocity increases with the inlet boundary layer thickness. If the uniform inlet profile is used, velocity at all radial positions would be equal to that at freestream.

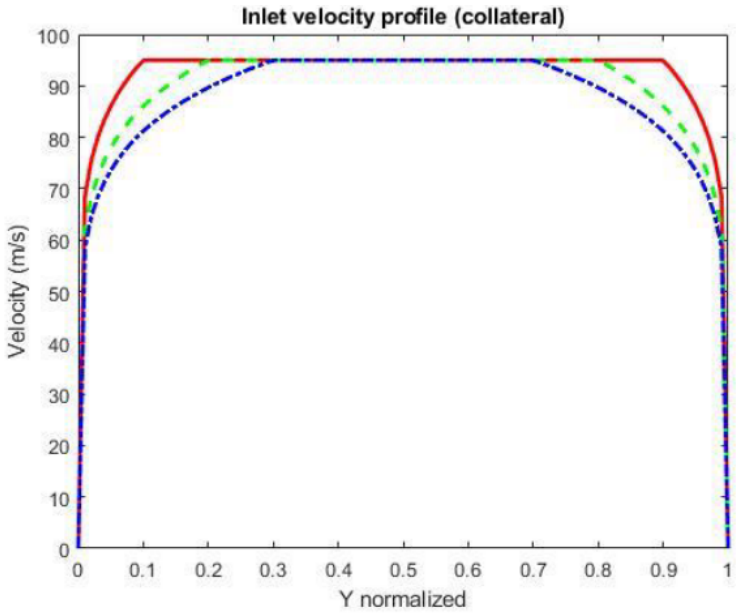

Figure 4.16: Inlet velocity profile with different incoming boundary layer thicknesses.

Figure 4.17 presents the effect of inlet boundary layer thickness on the static pressure recovery coefficient, while Figure 4.18 shows the effect of inlet boundary layer thickness on the total pressure loss coefficient. The studies are investigated with two mean diffuser angle configurations. It can be seen that the increase of inlet boundary layer thickness would lead to consistent detrimental effects. Both configurations with different diffuser angle show that increasing inlet boundary layer thickness results in reduction of static pressure recovery coefficient and increase in total pressure loss. The rate of static pressure coefficient reduction and total pressure loss increase seems to be linearly correlated with the size of inlet boundary layer thickness.

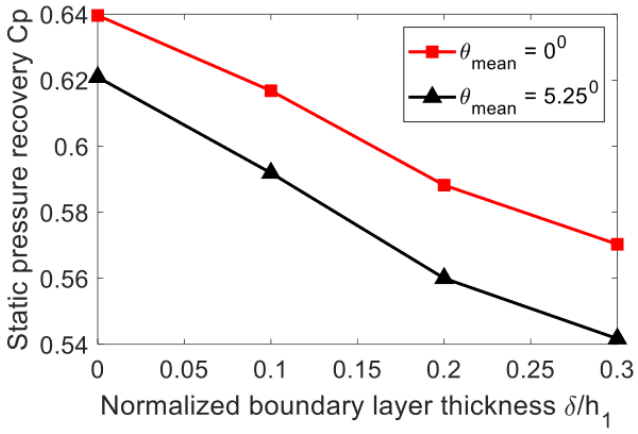

Figure 4.17: Effect of inlet boundary layer thickness on the static pressure recovery coefficient C_p.

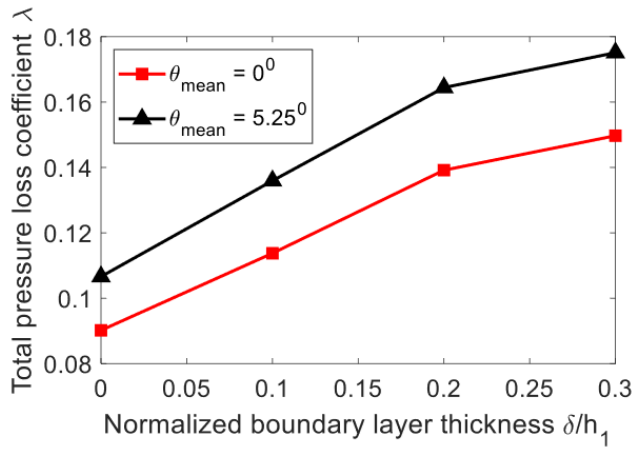

Figure 4.18: Effect of inlet boundary layer thickness on the total pressure loss coefficient λ.

Figure 4.19 further compares the total pressure loss with a clean inflow condition and with the non-uniform inlet of boundary layer thickness $\frac{\delta}{h_1} = 0.3$. As expected, the high total pressure loss region increases rapidly with the increase of inlet boundary layer thickness. It is important to note that not only the loss core is attributed to the corner dump gap but also attributed to the low velocity region near-wall in the pre-diffuser. This low velocity flow field stems from the inlet boundary layer and convects downstream. Due to the retarded flow region near-wall, the bulk free-stream flow now has to act as if the flow curvature is much higher, thus leading to a higher parasitic loss.

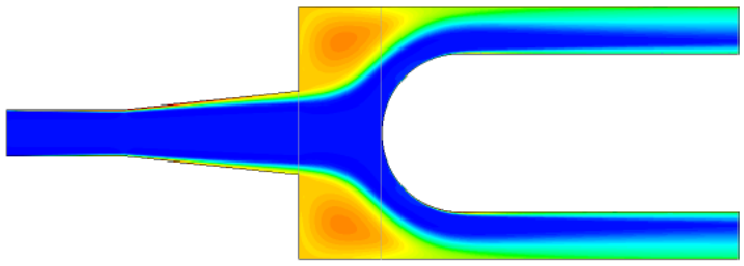

(a) $\frac{\delta}{h_1} = 0.0$ (clean inflow).

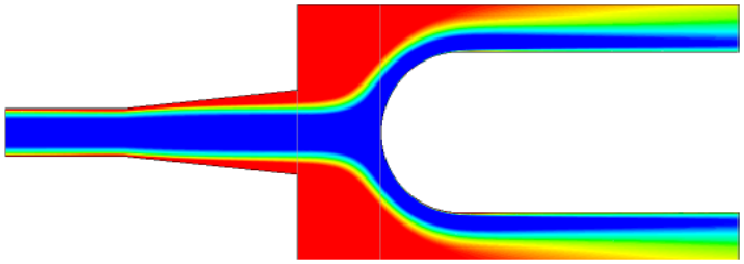

(b) $\frac{\delta}{h_1} = 0.3$ (non-uniform inflow with boundary layer thickness).

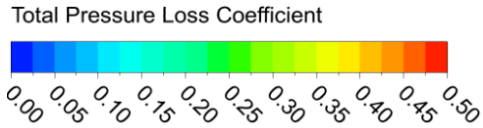

Figure 4.19: Total pressure loss contour for a clean inflow against a non-uniform inflow due to inlet boundary layer thickness at nominal diffuser angle ($\theta_i = 6^0$, $\theta_o = 6^0$) and nominal dump gap ratio ($\frac{D}{h_2} = 1.0$).

4.6.2 Effects of boundary layer symmetricity

Although we have had useful observations from comparison between the clean inflow and non-uniform inflow due to inlet thickness boundary layer, it is noted that the incoming flow profile can also be asymmetrical due to the strong three-dimensional flow at the compressor bladerow exit. In this section, we further explore the non-uniform inflow with the asymmetrical velocity profile. It is in contrast to the symmetrical inlet boundary layer profile in the previous computational investigation. Herein, the "top only" asymmetrical inlet boundary layer profile means that the velocity deficit region only presents near the outer annulus casing; whereas the "bot only" asymmetrical inlet boundary layer profile means that the velocity deficit region only presents near the inner annulus casing. Figure 4.20 shows the effect of asymmetrical boundary layer profile on the static pressure recovery coefficient, while Figure 4.21 presents the effect of asymmetrical boundary layer profile on the total pressure loss. Note that the results also show the comparison for three values of inlet boundary layer thickness $\frac{\delta}{h_1} = 0.1$, 0.2 and 0.3.

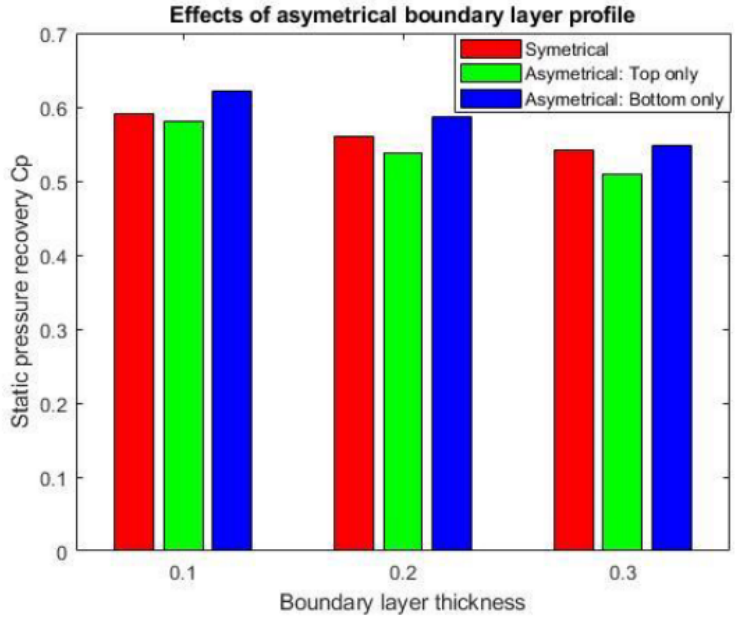

Figure 4.20: Effect of asymmetrical inlet boundary layer thickness on the static pressure recovery coefficient C_p.

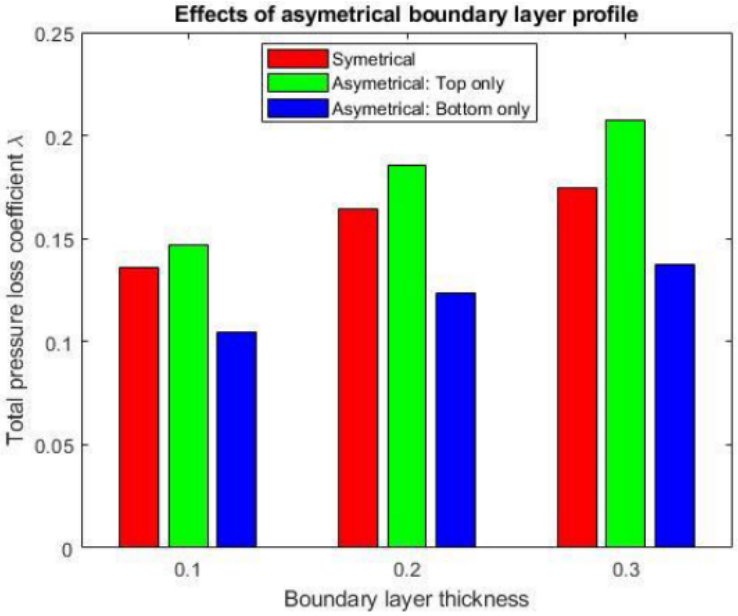

Figure 4.21: Effect of asymmetrical inlet boundary layer thickness on the total pressure loss coefficient λ.

Figure 4.22 further presents the total pressure loss contours for the symmetrical and asymmetrical inlet boundary layer profile. The “top only” asymmetrical boundary layer profile shows the highest loss core in the corner dump gap, clearly in agreement with the previous discussion. The presence of the asymmetry can be observed by tracking the total pressure loss in the near-wall region. In Figure 4.22b and Figure 4.22c, the asymmetrical total pressure loss distribution in the pre-diffuser can be seen.

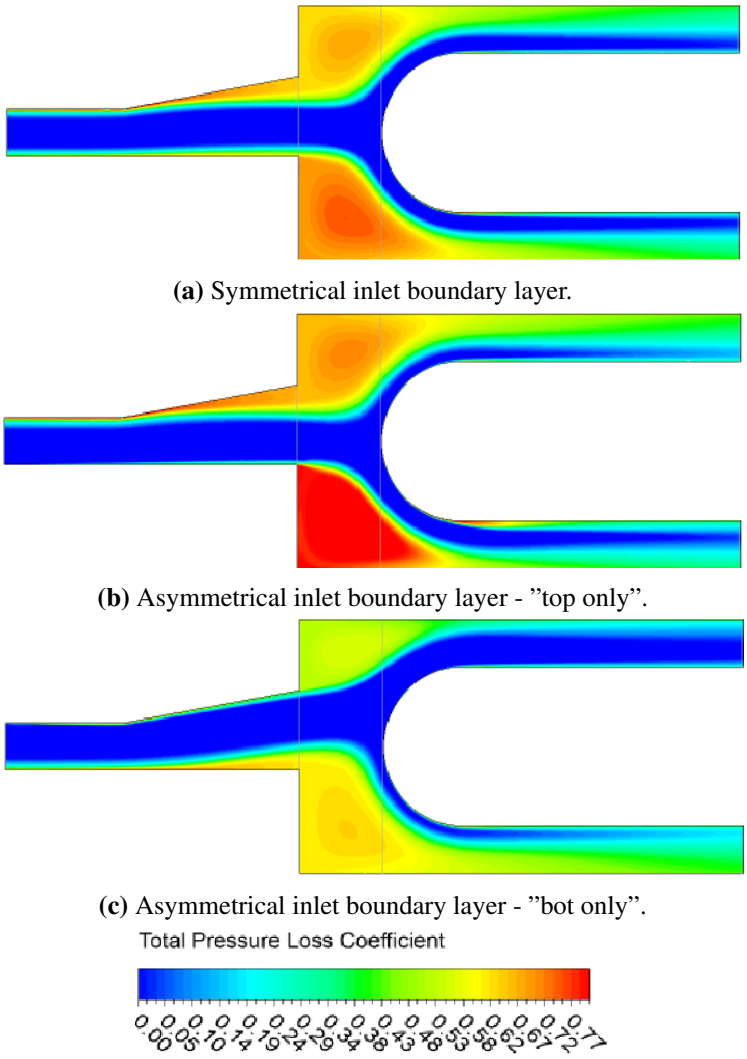

(a) Symmetrical inlet boundary layer.

(b) Asymmetrical inlet boundary layer - ”top only”.

(c) Asymmetrical inlet boundary layer - ”bot only”.

Figure 4.22: Total pressure loss contours for asymmetrical inlet boundary layer at upwards canted diffuser angle configuration ($\theta_i = 0^0$ and $\theta_o = 10.5^0$).

The finding that the "bot only" asymmetrical inlet boundary layer profile has the best performance is important to note. The dump diffuser shown in this example is canted upwards due to he high mean diffuser angle, in resemblance with the real configuration of the combustor system. Bear in mind that the dump diffuser combustor system is always subject to the non-uniform inflow from the compressor OGV exit. The ideal situation is that the inlet profile thickness in the pre-diffuser can be reduced substantially such that the flow field approaching the clean inflow condition and achieving the best performance. However, this would require some passive/active suction or bleed holes, which will complicate the design and affect the system cost and weight. Using the result presented in the current work, it is shown that there is a possibility for the combustor designer to design the pre-diffuser with an asymmetrical inlet profile. This can be done by modifying the OGV geometry asymmetrically, bleeding only the outer annulus casing wall, or the combination of the two methods. Considering the integrated OGV/pre-diffuser design method is a proven technology [82, 83], which has been adopted in the real machines (as in Rolls Royce Plc), the finding in this current work opens a new design space for the designer, potentially leading to a more efficient combustor system.

4.7 Summary

The present chapter consists of two parts. In the first part, the effects of the dump diffuser combustor geometry on its performance has been investigated. Two geometrical parameters have been chosen to explore the effects of the combustor geometry, namely the pre-diffuser divergence angle and the dump gap ratio. The following observations are made based on the series of computational results:

- With an increase in the mean diffuser angle, the static pressure recovery coefficient decreases and the total pressure loss increases. Thus, the more curved the pre-diffuser is, the lower performance capability the combustor system has.

- With an increase in the dump gap ratio, the static pressure recovery coefficient increases and the total pressure loss decreases. Thus, the longer the distance

between the pre-diffuser exit and the dome head is, the higher performance capability the combustor system has.

- If the weight and length of the combustor system is accounted for in decision making, there exists an optimum configuration with desired aerodynamics performance.

In the second part of the present chapter, the effects of symmetrical and asymmetrical inlet boundary layer thickness have been investigated by perturbation of the inlet radial boundary conditions. The following observations are made:

- With an increase in inlet boundary layer thickness, both static pressure recovery coefficient and total pressure loss coefficient decreases. The rate of reduction seems to be linearly correlated with the size of inlet boundary layer thickness.

- With the change in inlet boundary layer asymmetry, the "bot only" configuration outperforms the other configurations. This is effectively the situation in which the inner annulus casing wall has a thicker inlet boundary layer thickness compared to its outer annulus casing wall counterpart.

- The finding opens a new design space for the combustor designer to design a more efficient combustion system based on the conditions at the compressor OGV exit. This can be done by modifying the OGV three-dimensional blade shape to have a thinner velocity deficit zone near the outer annulus casing. Alternatively, this can be realized using the suction/bleed holes only on the outer annulus casing walls. The combination of the two aforementioned approaches would be also expected to be more effective. With the suggested design technique, we hope that the asymmetrical approach will be more beneficial than the conventional design method in terms of weight and saving of passive/active suction and bleed.

Chapter 5

Modeling Reacting Flow in a Micro-Gas Turbine Combustor

5.1 Introduction

In the renewable energy sector, micro-gas turbines are used for electricity production. These turbines offer the advantage of being able to run on alternative fuels such as biogas, hydrogen, liquid biofuels, and so on, along with a low capital cost. The literature review by De Robbio [84] highlighted the growing role of micro-gas turbines in distributed electric and thermal energy generation from renewable sources. The review also described the integration of micro-gas turbines with other energy conversion systems such as solar fields, ORCs, and fuel cells. Banihabib and Assadi [85] recognized the potential of micro-gas turbines in the rapidly growing decentralized energy market due to their low emissions, fuel flexibility, and low maintenance. The authors discussed the challenges in improving the operational flexibility, reliability, and availability of micro-gas turbines while maintaining low environmental impact. Ji et al. [86] demonstrated the potential use of micro-gas turbines as range extenders for electric vehicles to replace diesel-based engines. Micro-gas turbines are also used as propulsors in unmanned aircraft. Capata and Saracchini [87] conducted experiments on a miniaturized turbine for radio-controlled vehicles that run on different fuels and showed that a propane-butane mixture is more economically advantageous than kerosene. Habib et al. [88] investigated the

effects of adding biofuel to Jet A and found that the addition reduced static thrust and specific fuel consumption but increased thermal efficiency. An optimum mixture reduced CO and NO pollutant emissions without a significant reduction in static thrust. Large and Pesyridis [89] explored the potential of improving the performance of existing micro turbojet gas turbine engines by converting them into turbofans.

To meet stringent environmental regulations, alternative fuels have been extensively investigated, as demonstrated by the above literature. Another aspect that has been relatively overlooked is the impact of micro-gas turbine design variables on emissions. Okafor et al. [90] experimentally examined the effects of fuel injection angle, combustor inlet temperature, equivalence ratio, and ambient pressure on flame stabilization and NO_x emissions. They showed that inclined fuel injection resulted in improved flame stability and lower NH_3 and NO_x emissions compared with vertical injection along the combustor central axis. Zong et al. [91] proposed an external combustion air adjustment method to control the reaction zone fuel-air ratio under off-design loads. The results showed that the combustion air adjustment system reduced CO emissions but increased NO_x emissions due to a longer residence time in the reaction zone. Lefebvre [92] found that the hydrogen and/or aromatics content in the fuel composition had a significant impact on flame radiation and liner wall temperature but only a slight effect on CO and NO_x emissions. Chmielewski et al. [93] showed that the addition of water to the default engine fuel moderately decreased fuel consumption and significantly reduced NOx emissions. Chmielewski and Gieras [94] conducted an experimental and numerical study that showed that a variable dilution holes area design concept can increase outlet total temperature by 25% while reducing NO_x and CO emissions by 40%.

Soot is a crucial pollutant emission for micro-gas turbines. These are small particles produced during hydrocarbon fuel combustion and are carcinogenic. Soot also affects the performance of gas turbines by reducing the lifespan of components due to the burning of deposited soot on the turbine surfaces. According to Naegeli et al. [95], the flame temperature significantly increases soot concentration, with a decrease in the H/C ratio leading to an even stronger increase in soot concentration.

Rault et al. [96] observed an increase in soot formation in 10% ethanol blend flames compared with original Jet A-1 flames in their experiments, which was attributed to changes in the flame structure.

Micro-gas turbines have several major components besides the combustor, including a compressor and a turbine. Interactions between these components can impact the performance and emission characteristics of the turbine. In the previous chapter, the effects of diffuser design and compressor outlet flow on the aerodynamic performance of the combustor were studied. Results showed that the diffuser–combustor integrated design, developed with the compressor outlet flow taken into account, had potential for improved performance. In real-life operation, micro-gas turbines face numerous sources of uncertainty, such as variations in boundary layer thickness, manufacturing variations in blade rows [80, 79, 81, 97, 98, 99], and more. These uncertainties, combined with interactions between components, can significantly impact performance. For instance, the combustor outlet flow results in a non-uniform inlet flow to the turbine stages [26, 100], and the combustor hot streak can degrade the aerothermal performance of the turbine [101, 102, 103]. This chapter presents the first part of a more comprehensive project aimed at understanding the fundamental aerothermal performance and emission characteristics of a micro-gas turbine model and finding ways to improve its operation. The study includes simulating a reacting combustor flow in conjunction with aerodynamic simulation of other gas path components. The current chapter focuses on the combustor with a reacting flow, investigating the effects of aerodynamic boundary conditions and fuel injection parameters in detail.

5.2 Test Case Descriptions

5.2.1 Geometry

The micro-gas turbine adopted in the current work is of turbojet type. It is built upon the KJ66 micro-gas turbine model [10]. Its typical use is for small radio-controlled unmanned aerial vehicles. This model and its modified variant [104, 11, 44] have been investigated extensively by other researchers due to the availability of its

geometrical and operational information. Figure 5.1a shows the cross-section and Figure 5.1b shows the whole view of the three-dimensional CAD model of the micro-gas turbine. As can be seen, this micro-gas turbine model comprises of a single-stage centrifugal compressor, an annular combustion chamber, a single-stage axial turbine, and an exhaust. The combustion chamber, which is the focus in the current work, is a reverse-flow type. It has several vaporizing tubes inside the chamber. The fuel feed supply pipes are not modeled for simplicity, and the liquid fuel is injected inside the vaporizing tubes. The droplet breakup models then convert the liquid fuel into the gaseous fuel by the vaporization process.

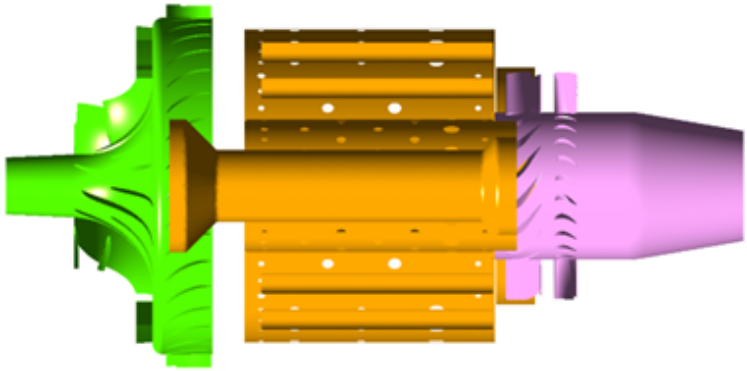

(a) Cross-section view.

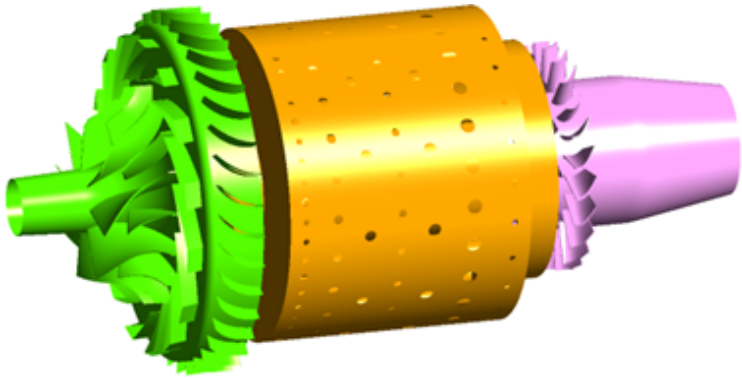

(b) Whole view.

Figure 5.1: Three-dimensional CAD model of the micro-gas turbine.

Figure 5.2 illustrates the flow paths inside the combustor to aid readers' visualization of the reversed combustor concept. Firstly the flow exits the compressor and enters the combustion chamber from the top left of the diagram. The flow divides into two streams: one in the axial direction towards the turbine and one in the radial direction towards the shaft. When the 1st stream flows across the combustion

chamber inner wall, a portion of the flow is bled into the combustor core through the dilution holes on the inner wall. The rest of the 1st stream goes towards the rear end and reverse into the vaporising tube, thus this type of architecture is known as reversed combustor. Inside the vaporising tube, the fuel vaporisation is modelled using the droplet breakup model and thus no nozzle geometry is resolved. The gaseous fuel mixes with air inside the vaporising tube. The mixture exits to the core where the flame sustains. Regarding the 2nd stream, the flow also moves downstream in the axial direction. When it passes the lower part of the combustion chamber walls, air is drawn into the core via the dilution holes and the lower walls are cooled. The combustion products in the core then goes to the turbine stage via the outlet.

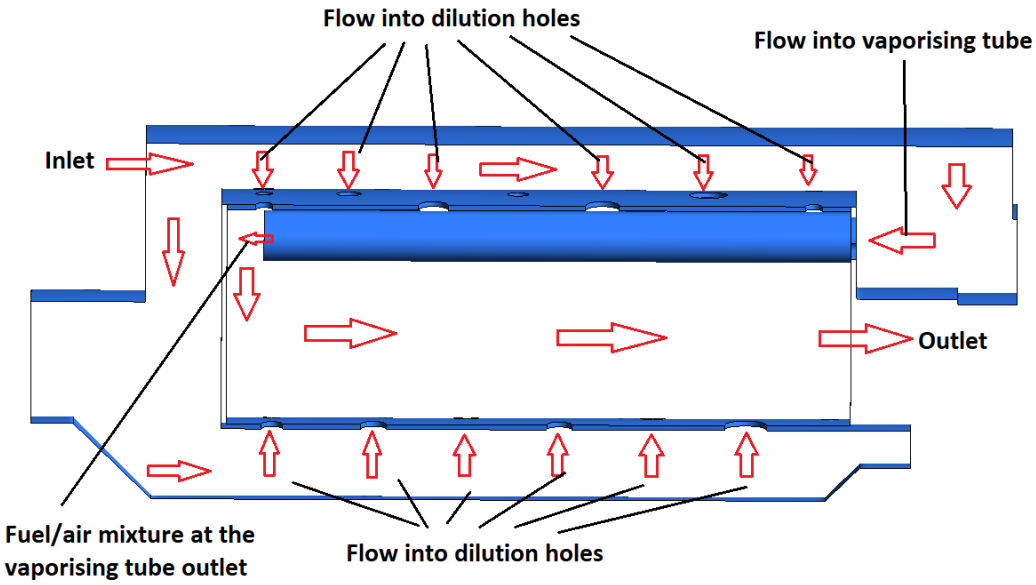

Figure 5.2: Schematic illustration of the combustor flow paths.

5.2.2 Computational Domain and Mesh

Only the combustion chamber is investigated in the current work. Figure 5.3 shows the computational domain and mesh of the combustion chamber. The computational domain lies between the compressor outlet/combustor inlet interface and the turbine inlet/combustor outlet interface. Only a single sector is modelled in the current work to reduce the computational cost. With a closer look at Figure 5.3a, the outer and inner walls of the combustion chamber can be visualized clearly. On the inner walls of the combustion chamber, there are several dilution holes of varying sizes and

locations. These holes provide air supply to complement the fuel combustion as well as cooling the combustion chamber walls. The combustion chamber geometry is meshed using the software ICEM. The surface meshes are quad-dominant and the volume meshes are hexa-dominant to ensure the high quality.

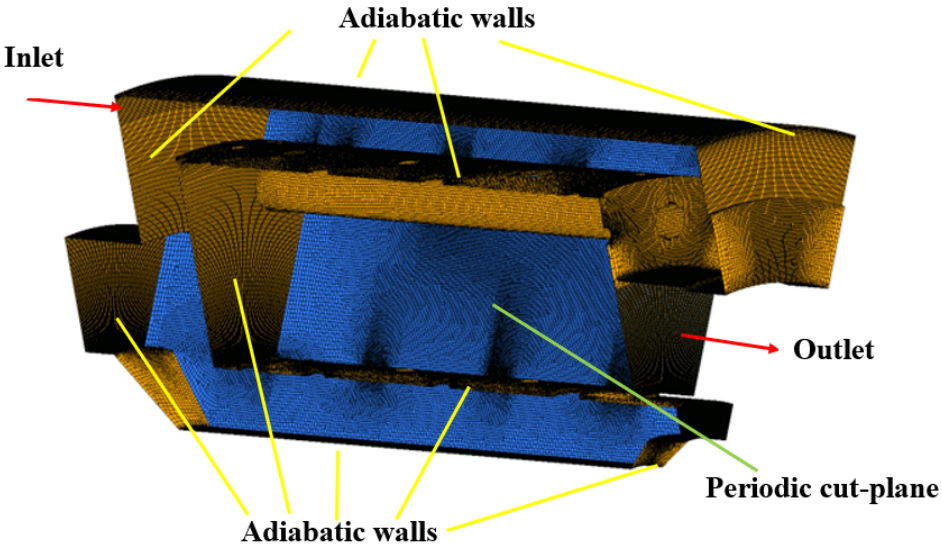

(a) Side view.

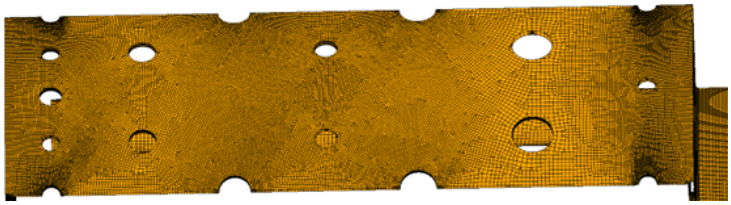

(b) Top view.

Figure 5.3: Computational domain and mesh of the combustion chamber sector.

5.2.3 Simulation setup and boundary conditions

A single-sector computational model of the combustion is used, with the two outermost interfaces set with rotational periodicity. At the combustor inlet, total pressure, total temperature, and flow angles are specified. At the combustor outlet, the static pressure is specified. These boundary conditions are uniform in the baseline case, aligned with the average values obtained from a whole engine simulation at the maximum thrust operating conditions. Liquid Jet-A fuel is injected inside the vaporizing tube at a specified mass flow rate, with specified injection angle and velocity. All wall surfaces are modelled as adiabatic no-slip surfaces.

5.2.4 Mesh sensitivity study

A mesh sensitivity study is crucial to ensure that the numerical results are not dependent on the mesh size. In this study, the mesh size is gradually refined until the quantities of interest change slightly. There are two global parameters that were used to assess the convergence: the combustion efficiency and the average soot mass fraction. The average soot mass fraction is simply obtained by performing mass flow weighted averaging of the soot mass fraction at the combustor outlet. The combustion efficiency is calculated from the equation below:

$$T_{04} = T_{03} + \frac{\eta_{cc} \cdot f \cdot HV}{c_{pg}} \tag{5.1}$$

where T_{04} is the average total temperature at the combustor exit; T_{03} is the average total temperature at the combustor inlet; η_{cc} is the combustion efficiency; f is the fuel-to-air ratio; $HV = 43.1 MJ/kg$ is the heating value for Jet-A fuel; c_{pg} is the gas specific heat.

Total temperature can be calculated as following:

$$T_0 = T + \frac{V^2}{2c_p} \tag{5.2}$$

where T_0 is the total temperature; T is the static temperature; V is the fluid velocity; c_p is the specific heat capacity.

Figure 5.4 presents the results of the mesh sensitivity study. The two quantities of interest are combustion efficiency (Figure 5.4a) and soot concentration at the combustor outlet (Figure 5.4b). The results indicate that the numerical predictions changed significantly from 1 to 3 million mesh elements. Beyond 3 million mesh cells, the results do not change considerably, and the results are deemed to be mesh independent. Although the bulk average values appear to be mesh independent, the local distribution and pattern of the total temperature field and soot concentration will also be checked.

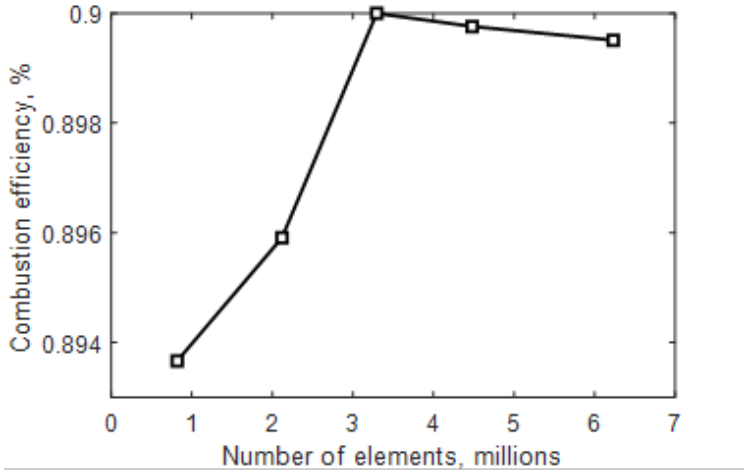

(a) Combustion efficiency.

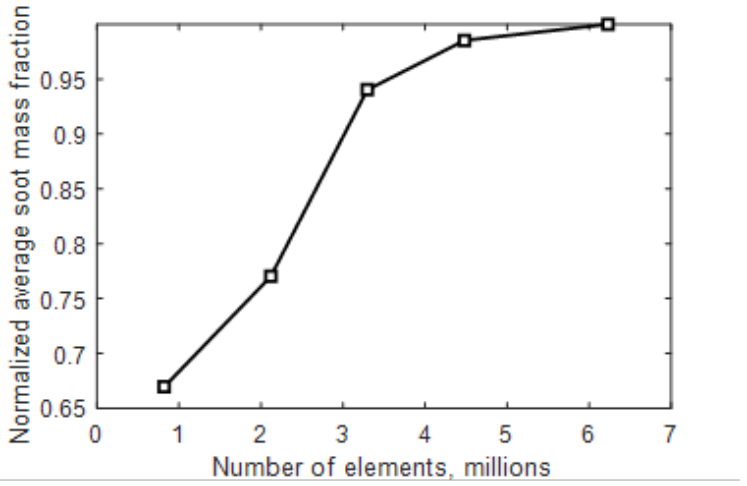

(b) Soot mass fraction.

Figure 5.4: Results of mesh sensitivity study for the combustion chamber simulation with a reacting flow.

Both combustion efficiency and soot formation are sensitive to the temperature distribution at the outlet. In the next steps, the total temperature distribution at the combustor outlet is further examined. Figure 5.5 shows the total temperature contours at the combustor outlet for different mesh size configurations. Firstly, a hot spot is evident, characterized by a high temperature zone at mid-span. As seen, the spatial extent and temperature level of the hot spot reduce with mesh refinement. The configurations shown in Figure 5.5c, 5.5d, and 5.5e are qualitatively similar, reinforcing the previous observation regarding combustion efficiency. As a result, the mesh with 4.5 million elements for a single sector is chosen as the final mesh for

the current study considering the balance of accuracy and computational cost.

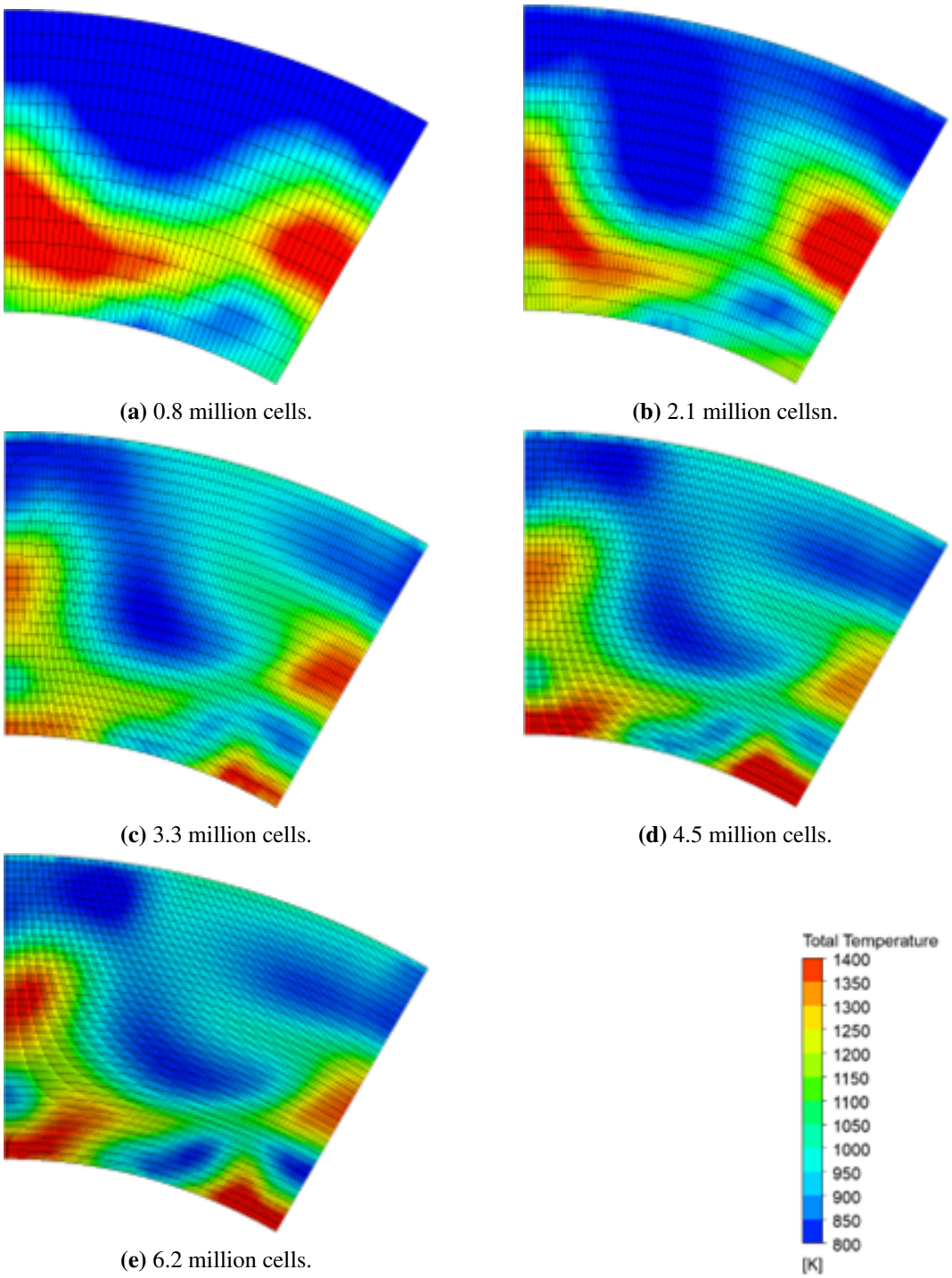

(a) 0.8 million cells.

(b) 2.1 million cellsn.

(c) 3.3 million cells.

(d) 4.5 million cells.

(e) 6.2 million cells.

Figure 5.5: Combustor outlet total temperature contour of different mesh size configurations.

5.2.5 Validations

In this section, the simulation method is validated using data from the public domain, including experiments by Schreckling [10] and numerical throughflow simulations by Yang et al. [11]. Two parameters, engine thrust and exhaust temperature, are compared.

The exhaust temperature is calculated as the mass flow weighted average static temperature at the exhaust nozzle exit. The thrust is calculated as the momentum change across the engine, assuming the pressure at the nozzle exit is equal to the freestream pressure:

$$F = \dot{m}_e V_e - \dot{m}_0 V_0 \tag{5.3}$$

where $\dot{m}_e$ is the exit mass flow rate; $\dot{m}_0$ is the inlet mass flow rate; V_e is the mass flow weighted average exit gas velocity; V_0 is the mass flow weighted average inlet gas velocity.

Figure 5.6 displays the validation results for engine thrust and exhaust temperature. The chosen operating point in the current work, at maximum thrust around 120,000 rpm, is slightly under-predicted for thrust and slightly over-predicted for exhaust temperature, but both are close to the expected results. A detailed analysis of the whole engine model is not the focus of this study and is presented in a separate report. The validation results confirm the validity of the CFD simulation approach used in this study. Further validations for the turbomachinery gas path for popular test geometries have been carried out using the same code and simulation method. However, they are not shown in the present work and will be released in future works that involved turbomachinery components.

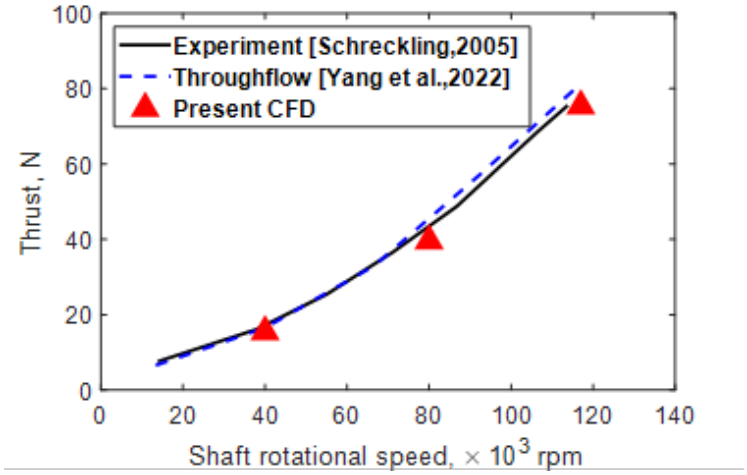

(a) Engine thrust.

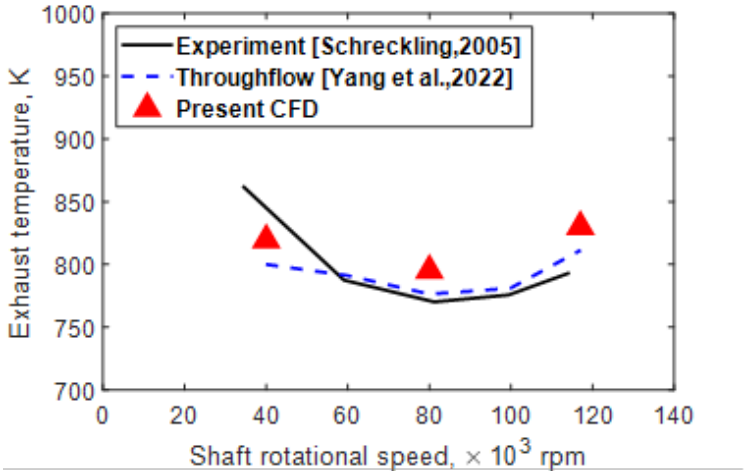

(b) Exhaust temperature.

Figure 5.6: Full engine validation results against the experiment of Schreckling [10] and throughflow simulations of Yang et al. [11].

5.3 Main Results

In this section, the main results of the current work is discussed. Firstly, the base-line configuration is analyzed to understand the fundamental flow mechanism within the micro-gas turbine combustor. Then, sensitivity studies of the outlet boundary conditions and fuel injection parameters are conducted. This study investigates the aero-thermal performance and soot emission characteristics of the micro-gas turbine combustor under different design and operating conditions.

5.3.1 Baseline configuration

Figure 5.7 shows the streamwise velocity contour at the cross-sectional surface of the combustion chamber with streamlines overlaid to aid visualization of the flow field. The streamwise velocity is high at both the inlet (compressor–combustor interface) and outlet (combustor–turbine interface). The flow field after passing the inlet is divided into two main paths. The first path follows the streamwise direction to the rear of the combustion chamber along the upper part of the chamber and then goes through the vaporization tube to mix with the fuel, demonstrating the reverse-flow combustor concept. The second flow path goes downward and then follows the streamwise direction along the lower part of the chamber. Part of the flow goes through the dilution holes as it travels in the streamwise direction. The combustion chamber has unique dump corners, characterized by low velocity and swirling flow zones, which retard the incoming flow from the compressor to a velocity suitable for combustion and maintaining the flame. As a result, it can be seen that the flow inside the chamber core has low velocity and high swirling flow, promoting efficient fuel mixing and combustion.

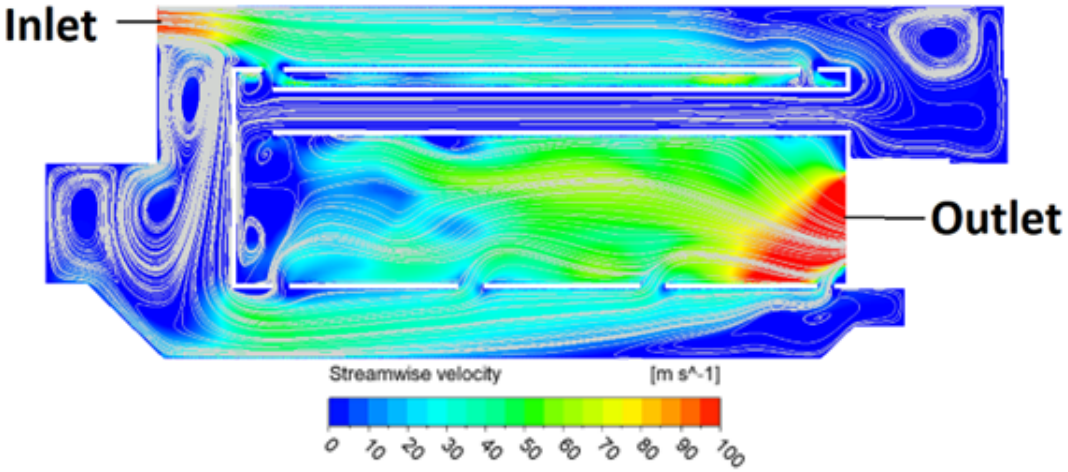

Figure 5.7: Streamwise velocity contour at the combustion chamber cross-section surface.

Figure 5.8 shows the streamwise temperature contour at the cross-section surface of the combustion chamber. The flame can reach up to 2400–2600 Kelvin degrees at the chamber core. It is interesting to note that the flame has the tendency to move down-ward, which would interact with the lower inner combustor casing. Thus, this part of the combustion chamber is prone to overheating if the cooling system is not designed properly.

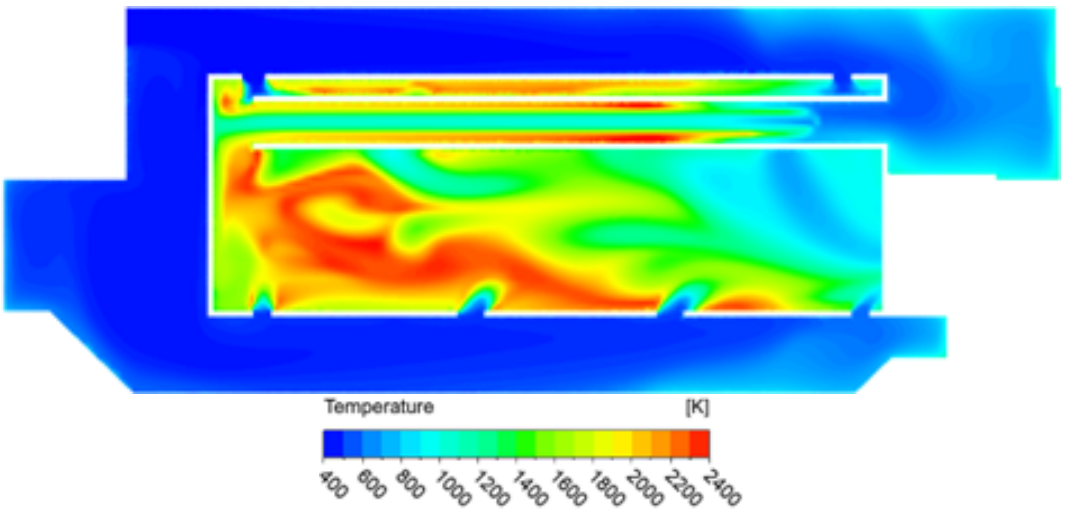

Figure 5.8: Streamwise temperature contour at the combustion chamber cross-section surface.

Figure 5.9a and Figure 5.9b show the total temperature and the soot concentration at the combustor outlet, respectively. A hot-spot can be seen at mid-span (Figure 5.9a), which is responsible for the hot streak that travels downstream to the turbine stage and reduces the nozzle guide vane's lifetime. In this micro-gas turbine model, there is also an end-wall hot-spot. Like the mid-span hot spot, it can overheat the turbine hub casing, reducing the performance and lifetime of the micro-gas turbine system. The soot concentration contour (Figure 5.9b) has a similar spatial distribution compared with the total temperature contour (Figure 5.9a), confirming that soot formation is highly correlated with the local temperature field.

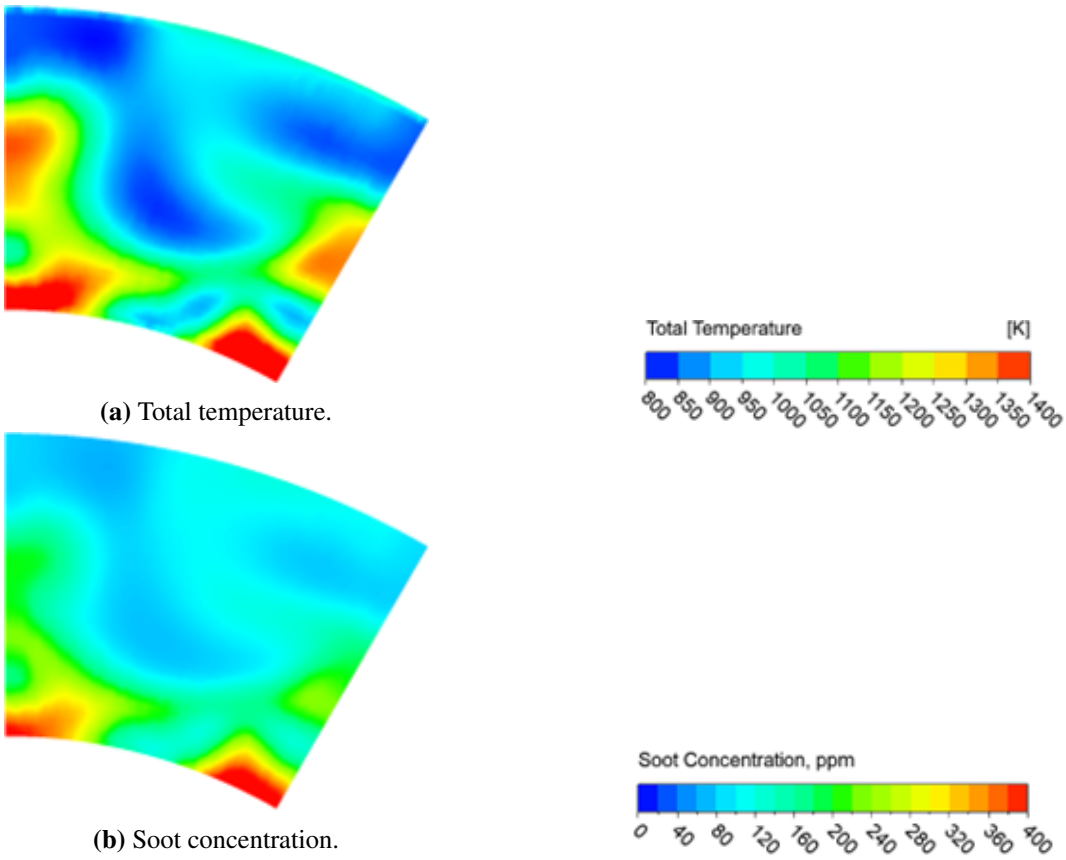

(a) Total temperature.

(b) Soot concentration.

Figure 5.9: Combustion chamber outlet contours.

5.3.2 Effects of outlet flow non-uniformity

In this section, the impact of outlet boundary conditions on the micro-gas turbine combustor is analyzed. The baseline configuration uses a uniform outlet static pressure boundary condition, which corresponds to the average value obtained from the whole engine model analysis. However, the presence of downstream nozzle guide vanes (NGVs) creates a pressure field upstream that affects the combustor simulation do-main. Figure 5.10 displays the pressure contour at the combustor–turbine interface in the fully coupled simulation model, showing an increase in pressure in certain circumferential and radial locations corresponding to the potential field of the turbine vanes. The results from the baseline configuration with uniform outlet pressure are compared with those obtained from the simulation with the non-uniform outlet pressure boundary condition.

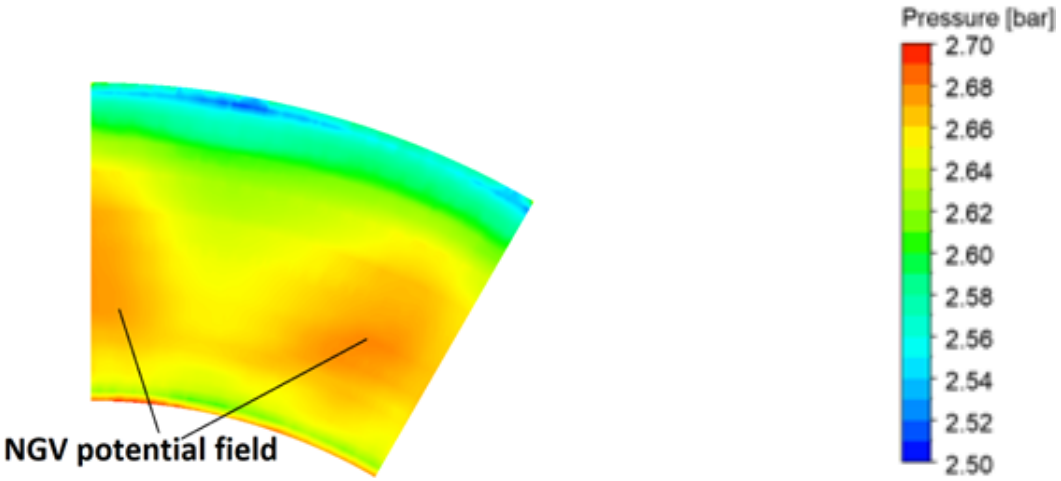

Figure 5.10: Combustion chamber outlet contours.

Figure 5.11 shows the contour of the total temperature at the combustor outlet under uniform (Figure 5.11a) and non-uniform (Figure 5.11b) outlet pressure boundary conditions. Both simulations exhibit similar spatial distributions, featuring mid-span and end-wall hot-spots. However, the non-uniform outlet simulation predicts a higher temperature at the combustor outlet, reflecting the zones with increased static pressure as seen in Figure 5.10. This aligns with the ideal gas law, which states that pressure levels are proportional to temperature.

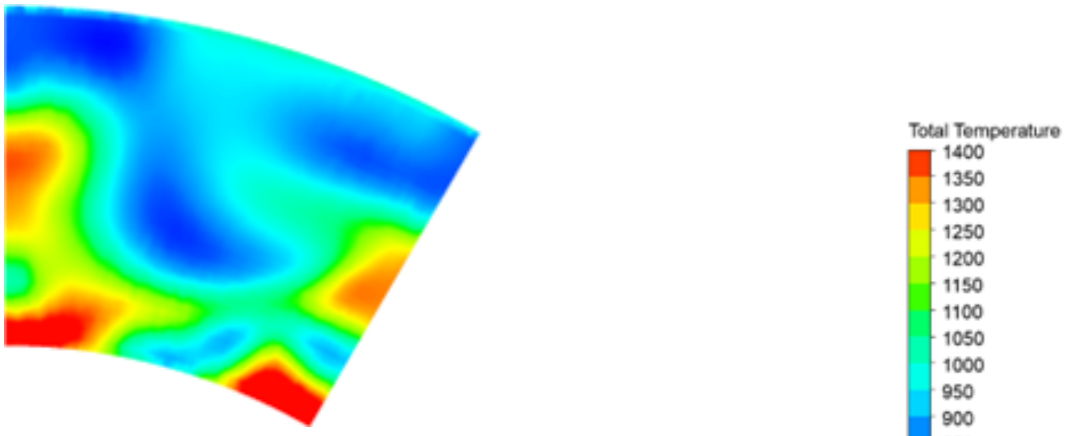

(a) Uniform pressure outlet boundary condition.

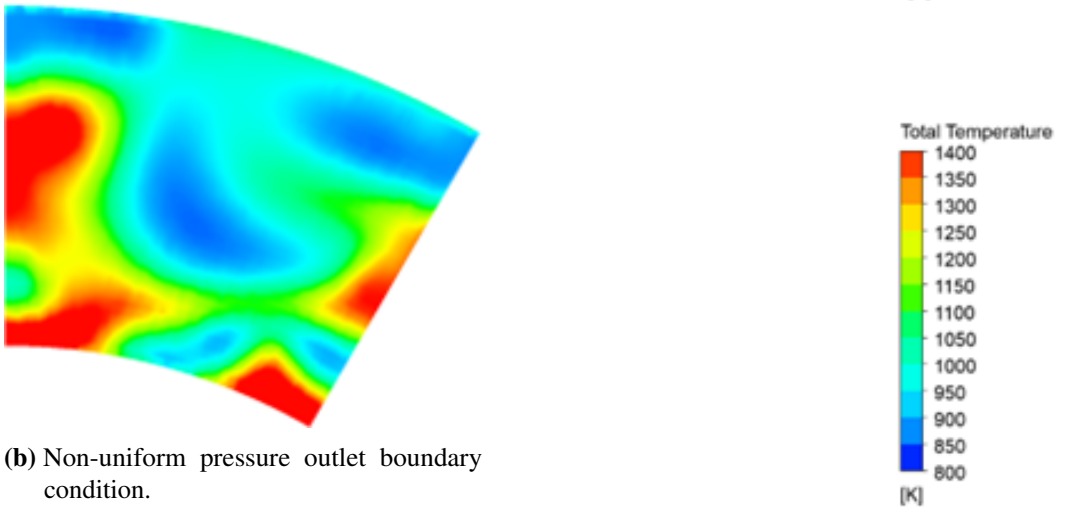

(b) Non-uniform pressure outlet boundary condition.

Figure 5.11: Effects of combustor outlet pressure uniformity boundary conditions on the outlet total temperature.

Figure 5.12 compares the circumferential distribution of the total temperature at the mid-span of the combustor outlet. The total temperature is defined as:

$$T_0 = T + 0.5V^2/c_p \tag{5.4}$$

where T_0 is the total temperature; T is the static temperature; V is the velocity magnitude; c_p is the gas specific heat.

Figure 5.12 shows the total temperature at a constant radial location (mid-span), normalized by the value of inlet total temperature specified in the boundary condition.

The overall shape of the total temperature remains similar in the circumferential direction, which supports the previous observation shown in Figure 5.11. The total temperature levels in the non-uniform outlet case are generally higher than in the uniform case. Notably, the circumferential location of the trough shifts from around 0.6 in the uniform case to around 0.5 in the non-uniform case. Although not discussed in detail in this paper, the circumferential location of the hot spot has a significant impact on the heat transfer in the downstream turbine stage.

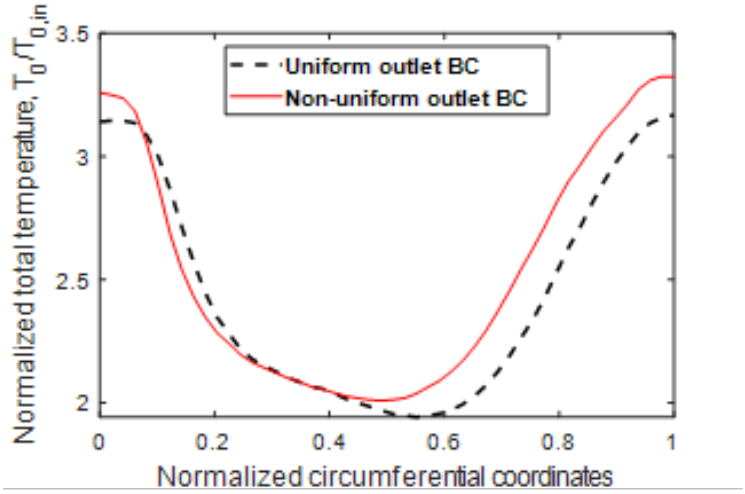

Figure 5.12: Total temperature circumferential distribution at the combustor outlet mid-span.

Figure 5.13 shows the contour of the soot concentration at the combustor outlet under uniform (Figure 5.13a) and non-uniform (Figure 5.13b) outlet pressure boundary conditions. The general spatial distribution is similar among the two simulations. The soot concentration (Figure 5.13) is highly correlated to the total temperature shown in Figure 5.11.

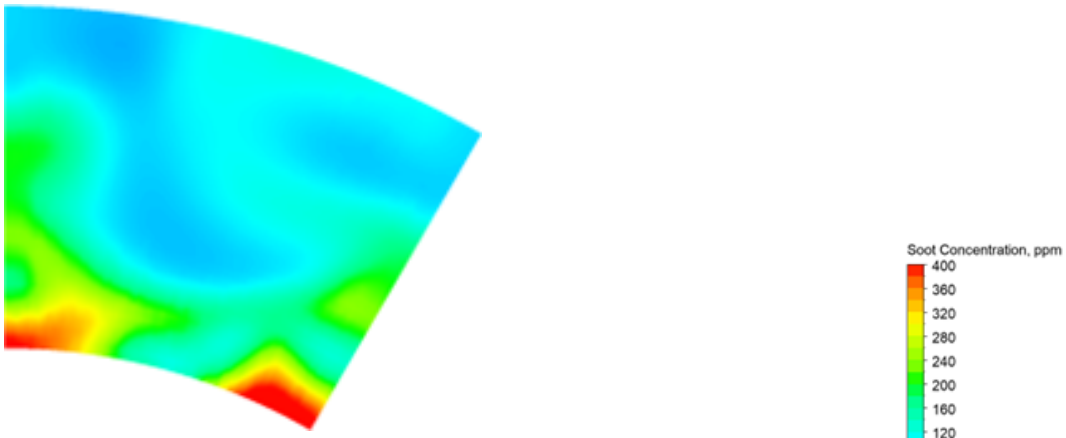

(a) Uniform pressure outlet boundary condition.

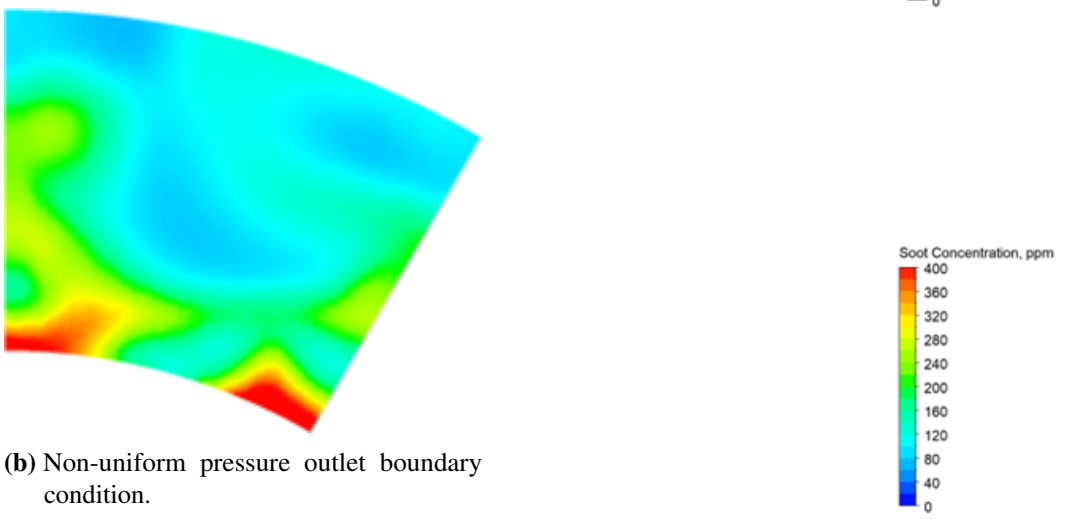

(b) Non-uniform pressure outlet boundary condition.

Figure 5.13: Effects of combustor outlet pressure uniformity boundary conditions on the outlet soot concentration.

Figure 5.14 compares the circumferential distribution of the soot concentration at the mid-span of the combustor outlet. The soot concentration levels in the non-uniform outlet case are slightly higher than in the uniform case. Notably, the circumferential location of the trough shifts from around 0.6 in the uniform case to around 0.5 in the non-uniform case. Figure 5.14 shows a better qualitative

comparison that is difficult to clearly observe in Figure 5.13.

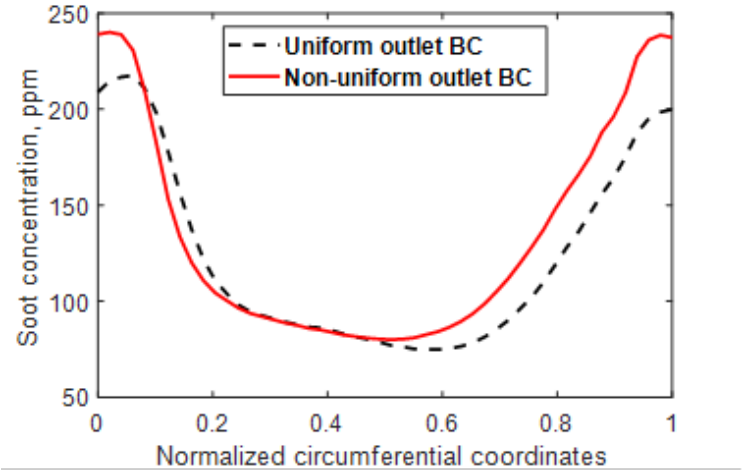

Figure 5.14: Soot concentration circumferential distribution at the combustor outlet mid-span.

Table 5.1 compares the combustor efficiency and the average soot concentration of the two simulations with uniform and non-uniform outlet pressure boundary condition. It can be seen that the uniform case has a slightly higher combustor efficiency while having about 9% lower soot concentration at outlet. Therefore, it can be concluded that the uniform outlet pressure boundary condition overestimates the combustion efficiency, while underestimating the soot concentration. This finding suggests that a fully coupled combustor–turbine is highly desired for a better prediction of performance and emission characteristics. If the individual component is to be simulated in a separate manner due to the simulation time and cost prohibitive requirements, exchange of the boundary conditions need to be performed for at least a few iterations.

	Uniform Outlet BC	**Non-uniform Outlet BC**
Combustor efficiency	0.9002	0.8928
Average soot concentration, ppm	134.283	146.426

Table 5.1: Comparison between uniform outlet BC and non-uniform outlet BC.

5.3.3 Effects of fuel-to-air ratio

In this section, the effects of fuel-to-air ratio is analyzed in more details. It is de-fined as the ratio of the Jet-A fuel mass flow rate to the engine air mass flow rate:

$$FAR = \frac{\dot{m}_{fuel}}{\dot{m}_{air}} \tag{5.5}$$

where FAR is the fuel-to-air ratio; $\dot{m}_{fuel}$ is the fuel mass flow rate; $\dot{m}_{air}$ is the engine air mass flow rate.

In fact, the fuel-to-air ratio is not an explicit control parameter. Depending on the operating point of the engine, a specific fuel mass flow rate is consumed corresponding to a given shaft rotational speed. Thus, the fuel mass flow rate is typically unknown, and is calculated iteratively to match the compressor power and the turbine power for a given shaft rotational speed. As is common practice, for example, in [105], the fuel mass flow rate was calculated using the secant root-finding method:

$$\dot{m}_{fuel,n+1} = \dot{m}_{fuel,n} + \left(\dot{W}_{c,n} - \dot{W}_{t,n}\right) \times \frac{\dot{m}_{fuel,n} - \dot{m}_{fuel,n-1}}{\left(\dot{W}_{c,n} - \dot{W}_{t,n}\right) - \left(\dot{W}_{c,n-1} - \dot{W}_{t,n-1}\right)} \tag{5.6}$$

where $\dot{W}_c$ is the compressor power; $\dot{W}_t$ is the turbine power; n is the time step n^{th}.

A similar iterative approach was also adapted in [11]:

$$\dot{m}_{fuel,n+1} = \frac{-1 - RP_{n-1}}{RP_n - RP_{n-1}} \times \left(\dot{m}_{fuel,n} - \dot{m}_{fuel,n-1}\right) + \dot{m}_{fuel,n-1} \tag{5.7}$$

where RP is the ratio of turbine power to the compressor power; n is the time step n^{th}.

Therefore, the investigation of the fuel-to-air ratio in this section can also be regarded as the investigation of the micro-gas turbine's performance at different working conditions along the operating line. Figure 5.15 shows the effect of fuel-to-air ratio on the combustion efficiency. The trend is clearly linear with an increase in the combustion efficiency when the fuel-to-air ratio decreases. Because the investigated range of fuel-to-air variation is actually small (note that the x-axis is normalized against a baseline fuel-to-air ratio), the trend in Figure 5.15 appears to be linear. A similar linear trend was also observed in [106].

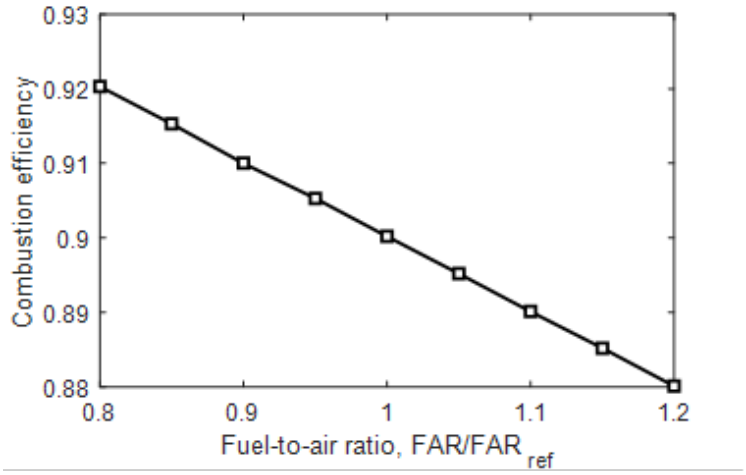

Figure 5.15: Effect of the fuel-to-air ratio on the combustion efficiency.

Because the combustion efficiency is strongly related to the total temperature values, we next analyze the total temperature distribution pattern. Figure 5.16 shows the circumferential distribution of the total temperature at the mid-span of the combustor outlet for different fuel-to-air ratios, which characterize the mid-span hot-spot. Changes in the fuel-to-air ratio significantly affect not only the level of the outlet temperature but also its pattern. As the fuel-to-air ratio decreases, both the peak and trough temperature decrease, indicating a reduction in the severity of the hot-spot at the combustor–turbine interface. Notably, the relative circumferential location of the peak and trough total temperature also change. It should be noted that the combustor and nozzle guide vane circumferential locations remain fixed for all investigations.

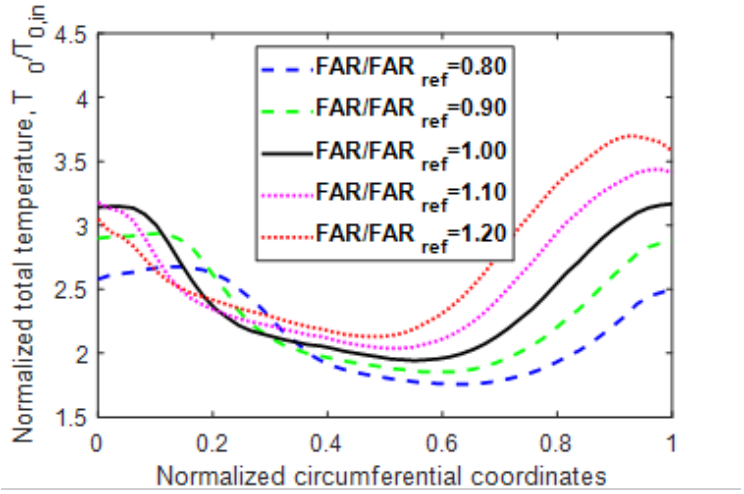

Figure 5.16: Total temperature circumferential distribution at the combustor outlet mid-span for different values of fuel-to-air ratio.

Figure 5.17 shows the average soot concentration at the combustor outlet for different values of fuel-to-air ratio. This time a non-monotonic relationship is observed. The optimum value of fuel-to-air ratio in terms of soot emissions is around 1.05, slightly larger than the baseline value in the current study. For fuel-to-air ratio values smaller or larger than this optimum value, the amount of soot emissions increase. Decreasing the fuel-to-air ratio tends to have a higher rate of soot formation.

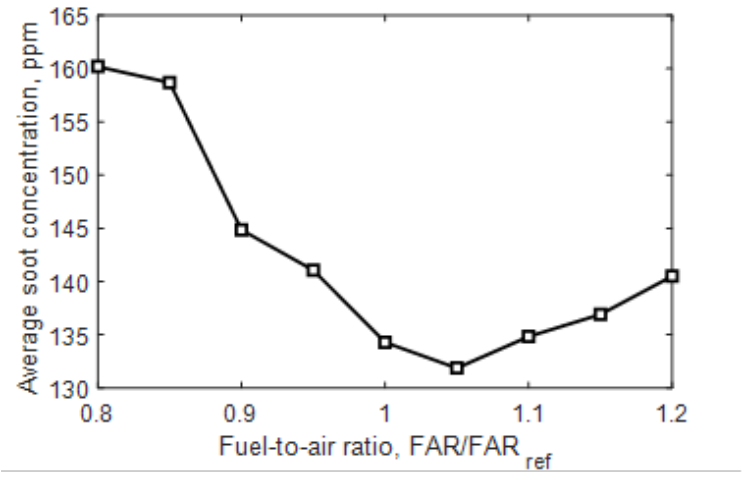

Figure 5.17: Effect of the fuel-to-air ratio on the soot concentration.

5.3.4 Effects of fuel injection velocity

Fuel injection velocity is another control parameter to be considered. In reality, fuel injection velocity can be realized by modifications of the fuel injector geometry (for example those in [107]). However, due to the simplification of spray modeling adopted in the present work, parametric changes in fuel injection velocity can be calculated directly. Figure 5.18 shows the effect of fuel injection velocity on combustion efficiency. The trend line remains almost constant with no significant change when fuel injection velocity is modified, indicating that fuel injection velocity has no impact on the combustion efficiency.

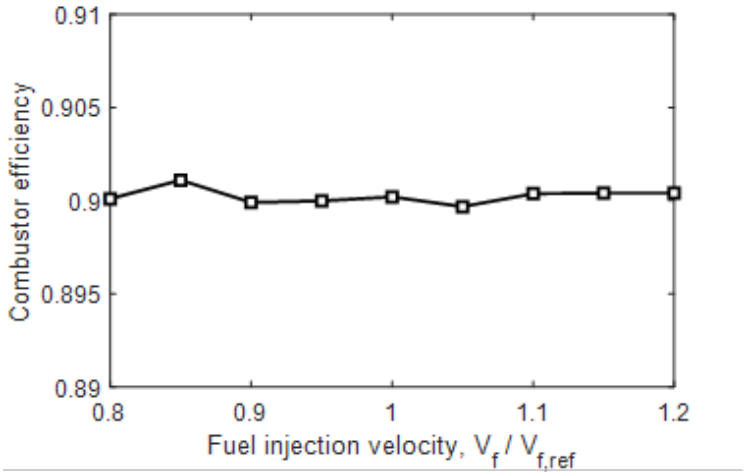

Figure 5.18: Effect of the fuel injection velocity on the combustion efficiency.

Similarly to the previous study, the total temperature distribution at the outlet is analyzed. Figure 5.19 shows the total temperature distribution in the circumferential direction at the combustor outlet mid-span for different values of fuel injection velocity. No significant change in temperature can be observed with different fuel injection velocities. The curves almost lay on top of each other. This confirms the observation form the combustion efficiency calculation (Figure 5.18), that is, the fuel injection velocity has no significant impact on the combustion efficiency.

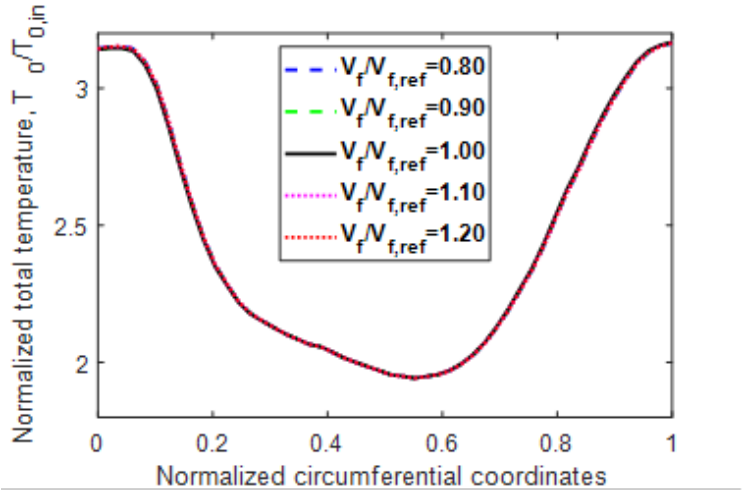

Figure 5.19: Total temperature circumferential distribution at the combustor outlet mid-span for different values of fuel injection velocity.

Figure 5.20 shows the average soot concentration for different values of fuel injection velocity. Although a non-linear pattern is observed, the trend is monotonic. As the fuel injection velocity decreases, the average soot concentration consistently increases. However, the rate of increasing is highest near the baseline value. Further away from the baseline injection velocity, the average soot concentration changes moderately. This trend can be partly explained by the fuel residence time. As the fuel injection velocity decreases, the fuel particles stay longer in the combustion zone, leading to a higher soot concentration.

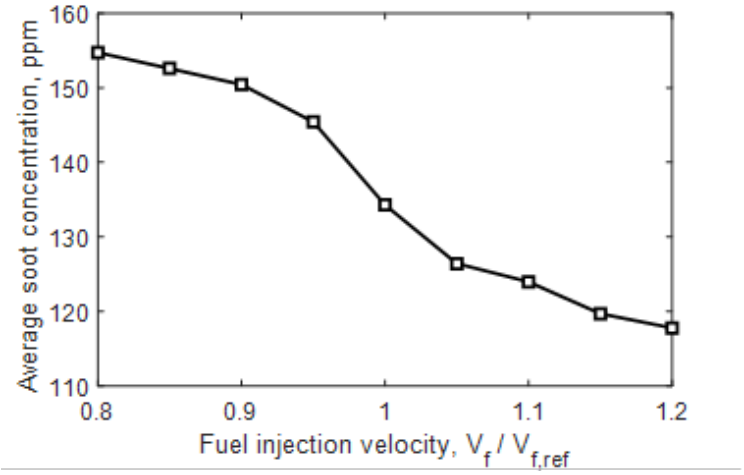

Figure 5.20: Effect of the fuel injection velocity on the soot concentration.

Therefore, it can be observed that the fuel injection velocity is a promising control parameter. For a slightly higher fuel injection velocity, the combustor efficiency remains almost the same, while soot emissions reduced significantly. The finding suggests that a relatively high injection velocity fuel injector design concept can potentially reduce soot emissions.

5.4 Summary

The current chapter explored the aerothermal performance and emission characteristics of a micro-gas turbine combustor, with a focus on its potential use in radio-controlled unmanned aerial vehicles. There are few works available in the public domain that attempt to model simultaneously the aerothermal performance and emissions of a micro-gas turbine. A comprehensive CFD model was developed in the work to model the reacting flow in the combustion chamber. The numerical model of the whole engine was validated against the experimental data and the throughflow model at the maximum thrust condition, which is also the operating point investigated in the current work.

Based on the numerical results and analyses presented in the current work, it can be concluded that the aerothermal performance and emission characteristics of the micro-gas turbine combustor are strongly influenced by various parameters. The main points are summarized below:

- Non-uniform outlet pressure can occur at the combustor–turbine interface due to the potential field of downstream nozzle guide vanes. It increases the maximum temperature at the hot spot. Combustor efficiency slightly decreases, and soot emissions significantly increase for the simulation with non-uniform outlet pressure boundary condition. The findings suggest that a two-dimensional boundary condition is required for the combustor simulation instead of an average value obtained from the cycle analysis for an improved prediction. The uniform outlet boundary condition simulation overestimates the calculation of the combustion efficiency and underestimates the soot emissions prediction.

- A lower fuel-to-air ratio results in a higher combustion efficiency. The fuel-to-

air ratio has a significant impact on the hot-spot temperature level and location, with an increase in maximum temperature as the fuel-to-air ratio increases. The fuel-to-air ratio has a non-monotonic effect on the soot emissions. The optimum value is around 1.05 times the baseline value. Any fuel-to-air ratio smaller or larger than the optimum value results in higher soot emissions.

- The fuel injection velocity has insignificant impact on both the combustion efficiency and the hot-spot level and location. The fuel injection velocity has a monotonic but non-linear relationship with soot emissions. As the fuel injection velocity decreases, soot emissions consistently increase.

The findings of the current chapter provide valuable information for improving the performance and emission characteristics of micro-gas turbine combustors. In the next steps, the interaction between the combustor and the turbine is further analyzed in more detail, based on the promising results preliminarily obtained in the current work. To meet the objectives of the project, potential modifications of the existing micro-gas turbine design shall be explored to mitigate the adverse effects.

Chapter 6

Modeling Combustor-Turbine Interaction with Reacting Flow

6.1 Introduction

Micro-gas turbines are widely used within the renewable energy sector to generate electricity as well as the aviation industry to facilitate propulsion. Nonetheless, these micro-gas turbines still mainly rely on fossil fuels for operation as of today, which has significantly contributed to global warming over recent decades. In response, governments have established the ambitious objective of achieving net zero emissions by 2050 to mitigate the effects of climate change. Ongoing technological advancements are dedicated to enhancing the efficiency and fuel adaptability of micro-gas turbines through continuous technological innovation.

In a micro-gas turbine engine, the interaction between a combustor and an immediate downstream turbine stage is of particular importance. The turbine blades must withstand substantial aerothermal and mechanical loading. Turbine blades' structural integrity tend to be the limiting factor of a micro-gas turbine. Thus, many researchers have attempted to investigate the combustor-turbine interaction. Miki et al. [100] used the Open National Combustion Code to simulate a 1/15 sector of the realistic combustor and first stage high-pressure turbine. They performed three different cases: 1) without the vane, 2) and 3) with the vane at different clocking conditions. They found that presence of the vane caused a noticeable difference

in the flowfields. Clocking did not significantly affect the combustor flow field but altering the migration of the hot streaks. Raynauld et al. [108] used a CFD solver that was able to deal with both reacting and compressible flow to simulate one sector of the combustor-turbine system. They demonstrated that the common approach based on spatial-temporal averaging to generate constant pressure boundary conditions at the combustor outlet would affect the predicted accuracy inside the combustion chamber. Koupper et al. [109] performed the Large Eddy Simulation on a single periodic sector of a combustor with two vanes system. They found that vane clocking has a noticeable effect on the hot streak transport in the turbine stage. The vane potential effect did not change the temperature patterns noticeably but significantly affect the radial and azimuthal mass flow distribution. Lo Presti et al. [110] simulated a full-annulus of a three-stage turbine with multi-species to resemble the combustion mixture composition. The results showed that the unsteady inlet boundary conditions increased the mixing, leading to a more uniform temperature profile. Duchaine et al. [111] performed Large Eddy Simulation on a single periodic sector of a combustor and a turbine stage system. The authors showed the difference in the turbulence from the combustion chamber that was not injected properly to the turbine stage if the turbine stage alone simulation was used. As a result, the blade thermal load predictions were significantly affected, while the stage expansion was not affected. Flaszynski et al. [112] used the Spalart-Allmaras and Explicit Algebraic Reynolds Stress turbulence models for a combustor-turbine system with different clocking positions. They observed that the vane potential effect is weak, however the clocking significantly affects the van temperature and flow conditions. Miki et al. [113] compared the sequential single-component simulation method against the fully-coupled simulation method for a combustor-turbine system. Although the mean combustor flowfields were similar between the two methods, there was a significant difference in the hot-streak distributions. The predicted turbine efficiencies also differed by 7% between the two methods. Salvadori et al. [114] compared the decoupled and loosely coupled approaches in simulating the combustor-turbine system. They demonstrated the importance of evaluating the

aerothermal performance using realistic boundary conditions, with 22% differences observed in Nusselt number prediction between the two methods. Verma et al. [115] evaluated the effectiveness of the joint simulation method against the co-simulation method for modeling combustor-turbine interaction. They concluded that the co-simulation was less accurate for aerothermal prediction because each vane was exposed to a similar temperature distribution.

Only a few combustor-turbine interaction studies attempt to model the combustion process and multi-species transportation. Nguyen et al. [116] studies the aero-thermodynamic processes, formation of nitrate and sulfate aerosol precursors, and the influence of chemical processes on aero-thermodynamics. They demonstrated that the chemical process had significant impact on the flow aero-thermodynamics, with up to 16.9% discrepancy for temperature prediction and 38.8% for flow velocity. Perpignan et al. [117] used Computational Fluid Dynamics (CFD) and Chemical Reactor Network (CRN) simulations to analyze the progress of NOx and CO species through a turbine stator with uniform boundary conditions. They found that the inclusion of the turbine stator is important for accurate prediction of pollutant emission prediction.

The present study is a part of a more comprehensive project aimed at understanding the fundamental aerothermal performance and emission characteristics of a micro-gas turbine engine and finding ways to improve its operation [12, 13]. In the previous published work of the authors [13], the combustor with a reacting flow was investigated. The authors have identified various aerothermal performance and emission characteristics of a micro-gas turbine combustor. The current work is a further study aiming to investigate the combustor-turbine interaction in more detail. Based on the above literature review, it is clear that the combustor-turbine interaction potentially has a non-negligible impact on both the aero-thermodynamic and emission characteristic. However, due to limited computational resources, numerical models must be simplified typically by imposing a periodicity condition and a decoupled combustor-turbine domain. Such simplifications may have an impact on the prediction accuracy and must be quantified. In addition, the combustion process

and transportation of multi-species flow through the turbine stage has rarely been modeled, also due to the constrained resources. Therefore, the present work adopts a fully-coupled whole-annulus with reacting flow to investigate the combustor-turbine interaction in a micro-gas turbine engine. The whole annulus domain will be modelled without any periodicity condition imposed, and the turbine and the combustor domains will be directly linked in a single simulation (i.e., full coupling). As a result, the combustion process and the transportation of multi-species flow will be modelled in both the combustor and the turbine stage. If the local temperature inside the turbine is sufficiently high, it will promote further combustion inside the turbine domain. This complex interplay among the flow field, aerothermal performance, and pollutant emissions can thus be systematically explored and evaluated.

6.2 Test Case Descriptions

6.2.1 Geometry

The current study employs a turbojet-type micro-gas turbine, based on the KJ66 micro-gas turbine model [10]. Originally designed for application in small radio-controlled unmanned aerial vehicles, this turbine model and its modified versions [104, 11, 44] have been extensively investigated by other researchers due to the accessibility of both its geometric and operational details. This micro-gas turbine model is composed of several key components: a single-stage centrifugal compressor, an annular combustion chamber, a single-stage axial turbine, and an exhaust. The combustion chamber follows a reverse-flow configuration and incorporates multiple vaporizing tubes at the core. To maintain simplicity of the model, the fuel feed supply pipes are omitted from the model, and instead, liquid fuel is introduced into the vaporizing tubes. Through the utilization of droplet breakup models, the liquid fuel is subsequently converted into gaseous fuel via a vaporization process.

6.2.2 Computational Domain and Mesh

The simulation domain in the current work comprises of the combustion chamber, the turbine stage, and the exhaust. Figure 6.1a illustrates the computational domain and mesh of the combustion chamber, while Figure 6.1b illustrates that of the turbine stage. A whole annulus model without any periodic interface assumption is adopted in this study. The combustion chamber domain and the turbine stage domain are directly coupled in a single simulation without any partitioning.

In Figure 6.1a, the reversed flow-type combustor architecture can be visualized more in detail. On the inner walls of the combustion chamber, there are several dilution holes of varying sizes and locations. These holes provide air supply to complement the fuel combustion as well as cooling the combustion chamber walls. For a more simplistic visualisation of the flow paths, one can refer to Figure 5.2. The flow paths are described here again for completeness. The flow enters the combustor from the top left of Figure 6.1a and divides into two streams: one in the axial direction towards the turbine and one in the radial direction towards the shaft. When the 1st stream flows across the combustion chamber inner wall, a portion of the flow is bled into the combustor core through the dilution holes on the inner wall. The rest of the 1st stream goes towards the rear end and reverse into the vaporising tube. Inside the vaporising tube, the Jet-A liquid fuel is turned into gaseous form using the droplet breakup model without the need to resolve the nozzle geometry. The gaseous fuel mixes with air inside the vaporising tube. The mixture exits to the core where the flame sustains. Regarding the 2nd stream, the flow also moves downstream in the axial direction. When it passes the lower part of the combustion chamber walls, air is drawn into the core via the dilution holes and the lower walls are cooled. The combustion products in the core then goes to the turbine stage via the outlet. The combustion chamber geometry is meshed using the software ICEM. The surface meshes are quad-dominant and the volume meshes are hexa-dominant. The full-annulus model of the combustion chamber comprises of about 36 million cells.

In Figure 6.1b, half annulus of the turbine stage can be observed with more

clarity. The stator vane is in blue colour and the rotor vane is plotted in magenta colour. Only one vane and one blade are plotted. The remaining vanes and blades are only showed in white at the hub. The boundary layers around the turbine blades are resolved for accurate modelling of viscous effects. The rotor blade also comprises of a clearance height with sufficient mesh resolution in the tip gap region. Mesh is also clustered near the hub and shroud endwalls. The software TurboGrid is used to mesh the turbine stage geometry with fully hexagonal elements. Each blade passage comprises of about 500 thousand elements, typically to the resolution used in other turbomachinery simulations in the literature [81, 97, 98, 99, 118, 119, 101]. The whole annulus model of the stator blade row comprises of 4.4 million cells, while that of the rotor blade row consists of 9.4 million cells. In total, the whole combustor-turbine domain consists of nearly 50 million cells.

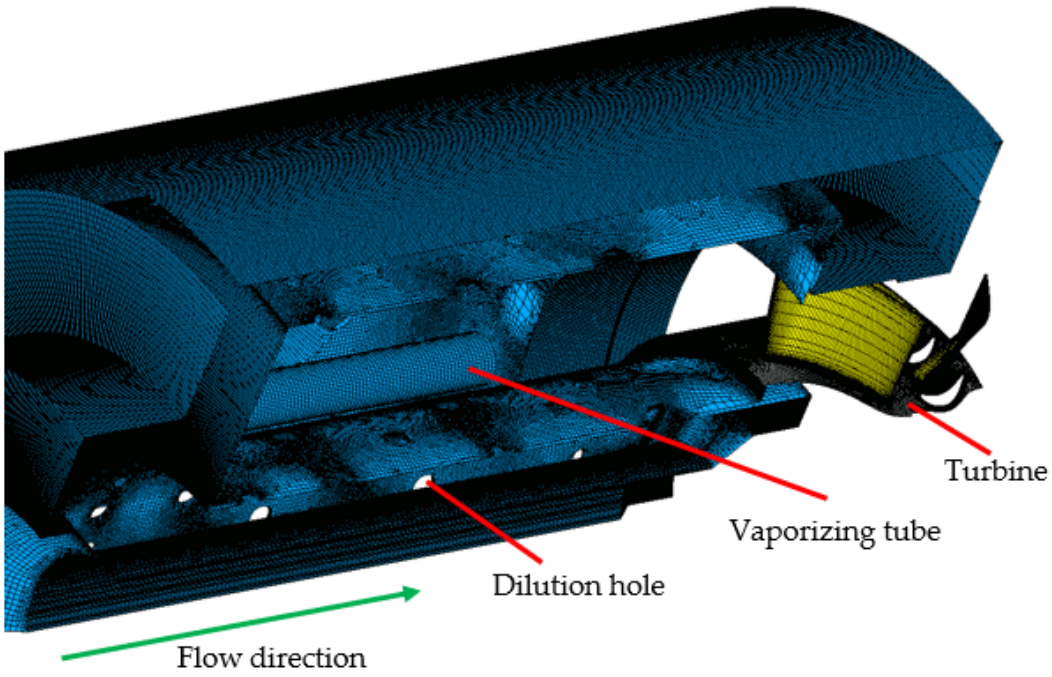

(a) Combustion chamber mesh

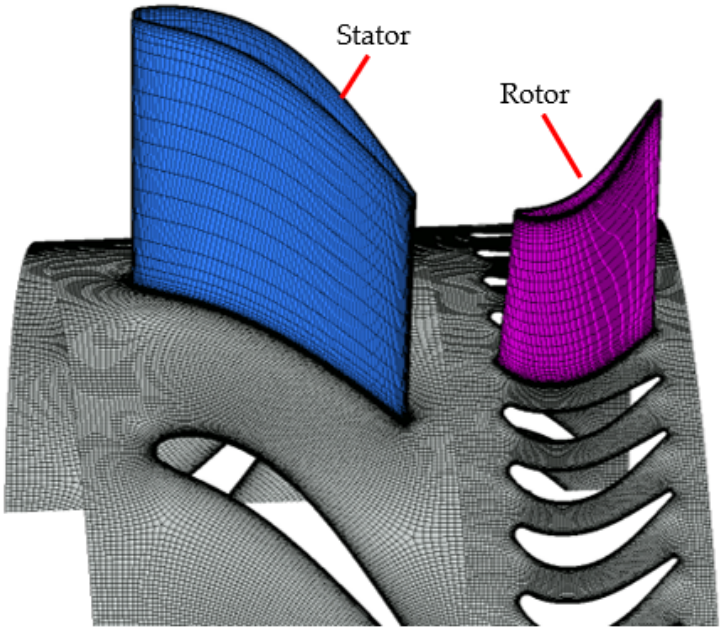

(b) Turbine stage mesh.

Figure 6.1: Computational domain and mesh of the coupled combustor-turbine simulation.

6.2.3 Simulation Setup and Boundary Conditions

Figure 6.2 illustrates the boundary conditions applied on the combustor-turbine simulation domain. A whole annulus model is adopted, thus no periodic conditions need to be specified. The combustion chamber and the turbine stator blade row are both stationary and directly coupled, thus the interface between the two sub-domains can be treated as a conventional interface. On the other hand, the turbine rotor blade row rotates at a specified rotational speed. Therefore, the interface between the stator and the rotor blade row needs more special treatment. In the current study, the "Frozen Rotor" approach is used. At the combustor inlet, total pressure, total temperature, and flow angles are specified. At the exhaust outlet, the static pressure is specified. Liquid Jet-A fuel is injected inside the vaporizing tube at a specified mass flow rate, with specified injection angle and velocity. All wall surfaces are modelled as adiabatic no-slip surfaces. To study the clocking effects, the turbine stator blade row is rotated while the combustion chamber domain remains in the original position.

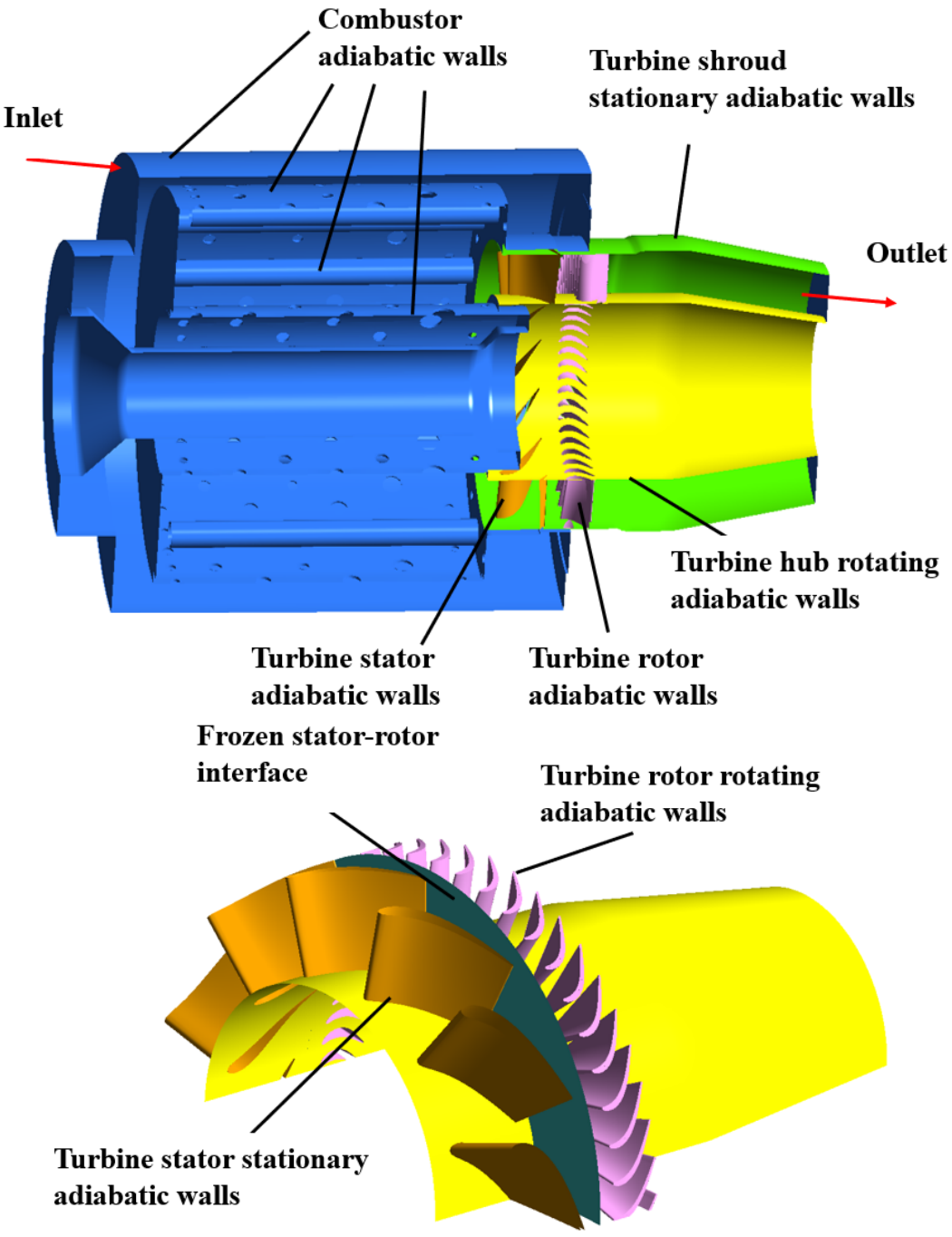

Figure 6.2: Computational domain and boundary conditions of the coupled combustor-turbine simulation (half annulus cut-plane view).

6.3 Decoupled vs Coupled Simulation Methods

As pointed out in the literature, the combustor-turbine interaction is commonly investigated using the decoupled simulation method due to the constraint of computational resources. This practice is encouraged by the thought that the decoupled simulation can converge quickly in a few iterations and the result is supposed to be similar to that of the fully-coupled simulation. Prior to the main analyses of the fully-coupled simulation results, firstly the comparison between the decoupled and fully-coupled simulation approaches are compared.

Figure 6.3 illustrates the sequential decoupled simulation method workflow for the simulation of combustor-turbine interaction. The key idea of this approach is the split of the combustor-turbine into two sub-domains, where each sub-domain is treated like a standalone simulation. The two domains are connected via the exchange of inlet/outlet boundary conditions at each iteration step.

In the first iteration step, the combustor is simulated with an assumed uniform outlet static pressure boundary condition. Once the combustor simulation finishes, the total pressure and total temperature distribution at the combustor outlet is obtained. This total pressure and total temperature field act as the inlet boundary conditions for the subsequent turbine stage simulation. Once the turbine stage simulation finishes, an iteration step finishes. In the next iteration step, a static pressure field at the turbine inlet is derived from the previous turbine stage simulation, which acts as the new outlet static pressure boundary condition for the next combustor simulation. This process continues for a few iterations until the solution fields converge. It is noted that combustion and multi-species transport are modelled within the combustor domain only. The turbine stage domain is modelled with air ideal gas.

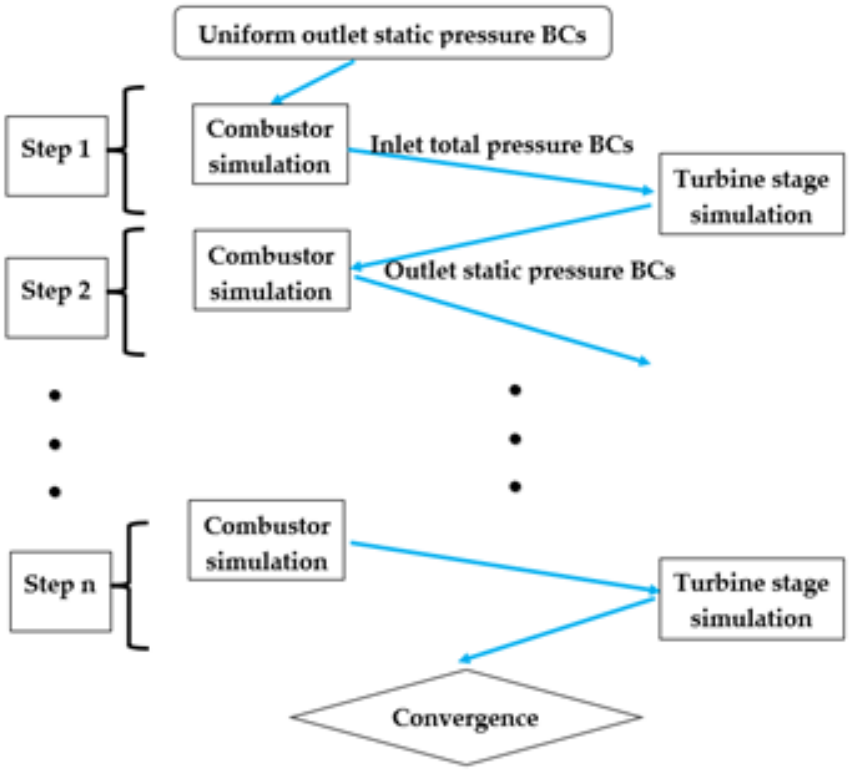

Figure 6.3: Sequential decoupled simulation method workflow.

In contrast, Figure 6.4 illustrates the coupled simulation method workflow for the simulation of combustor-turbine interaction. The combustor domain and the turbine stage domain are directly coupled in space and time. During each pseudo-timestep, both domains are solved and driven toward the converged solution. Unlike the sequential decoupled simulation approach, combustion and species transport modelling are applied for the whole combustor-turbine domain. As a result, the combustion process and transport of the combustion gases can be observed inside the turbine domain.

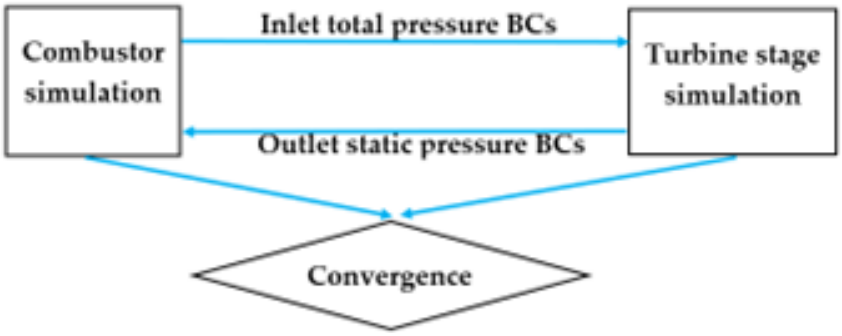

Figure 6.4: Coupled simulation method workflow.

Figure 6.5 compares the combustor efficiency calculated using the sequential decoupled approach against the coupled simulation approach. The prediction of the decoupled approach begins to stabilize after the 3rd iteration, however it still needs more iterations to converge to an acceptable error. The converged solution of sequential decoupled approach is different to that from the coupled approach, with about 1.5% error. It has been noted that combustion and species transport modeling are the same in the combustor domain for both decoupled and coupled approaches. The only difference comes from the boundary conditions at the combustor-turbine interface.

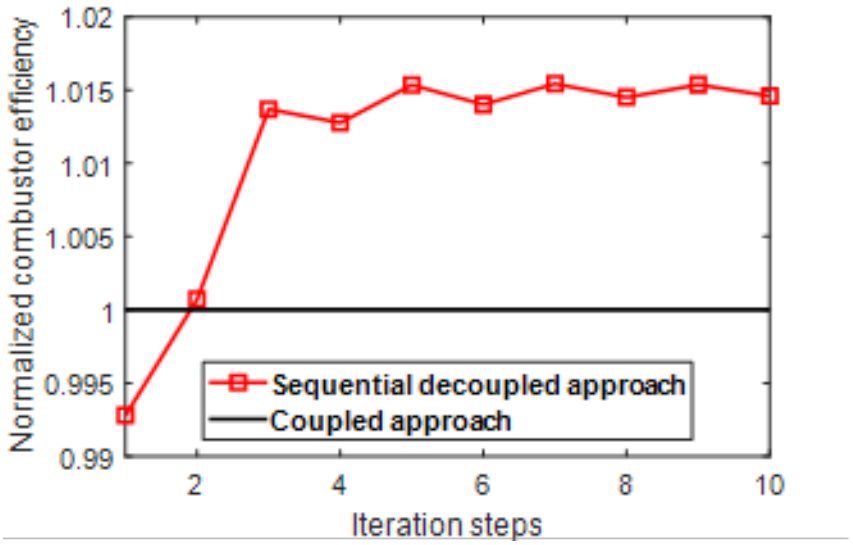

Figure 6.5: Combustor efficiency predicted by decoupled and coupled simulation approaches.

Figure 6.6 shows the comparison of turbine efficiency calculated using the sequential decoupled approach against the coupled simulation approach. The prediction of the decoupled approach begins to stabilize after the 3rd iterations however it still needs more iterations to converge to an acceptable error. The converged solution of sequential decoupled approach is different to that from the coupled approach, with about 4% error. It has been noted that the combustion and species transport modeling inside the turbine domain are applied in the coupled approach but not in the decoupled approach. The discrepancy between the two approaches not only stems from the boundary conditions at the combustor-turbine interface but also from the effects of multi-species gases in the turbine domain. As a result, it can be concluded that combustion and species transport modeling are important for a combustor-turbine interaction investigation. The sequential decoupled approach, although initially appeared to be more efficient due to truncated domain modeling, turns out to be less efficient (due to a number of iterations required to achieve coupling convergence) and less accurate (due to the lack of modeling combustion and species transport effects in the turbine domain) compared to the coupled approach. The numerical prediction within the turbine domain is more significantly affected by the choice of simulation coupling approach, while the numerical predictions within the combustor domain is slightly affected as the result of upstream propagation from the turbine domain.

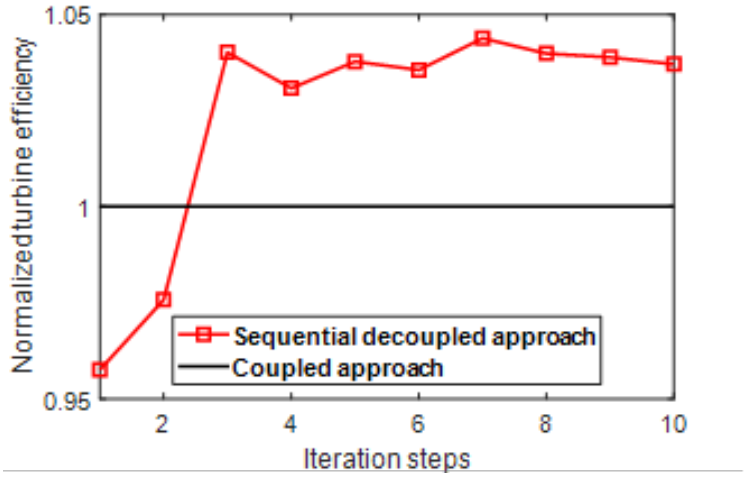

Figure 6.6: Turbine efficiency predicted by decoupled and coupled simulation approaches.

6.4 Aerothermodynamics and Soot Transportation across the Turbine Stage

In this section, the flow vortical structure across the turbine stage is investigated more in detail. Figure 6.7 shows the iso-surfaces of temperature T = 1300K across the turbine stage. Because the temperature diffuses across the first turbine vane blade row, the constant temperature iso-surfaces do not appear in the rotor blade row. In Figure 6.7a, the hot-streak originates from the mid-passage circumferential location. As a result, the high-temperature vortical structure moves in between two stator blades. On the other hand, Figure 6.7b shows the movement of hot streak vortical structure for the case with leading edge impingement. The vortical structure comes into contact and wraps around the stator blades.

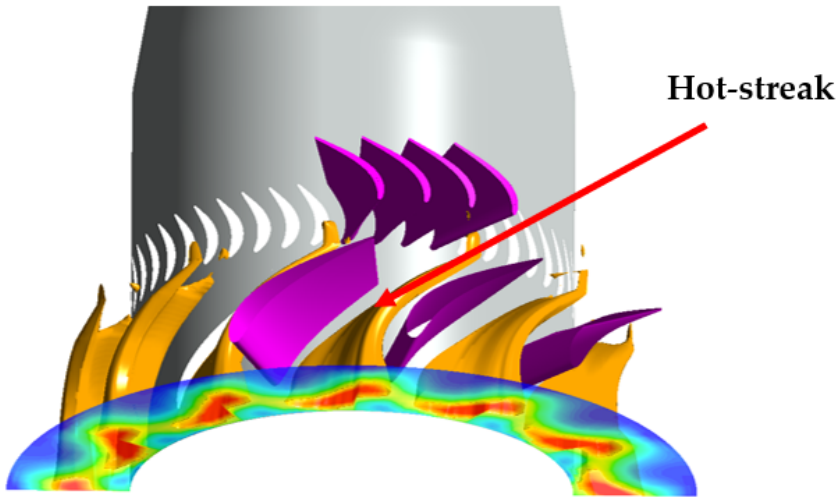

(a) Mid-passage hot-streak configuration.

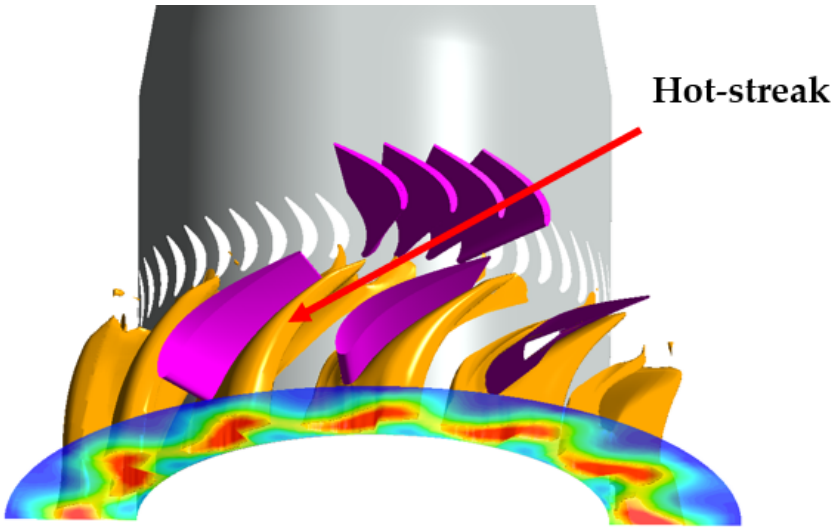

(b) Leading-edge impingement hot-streak case.

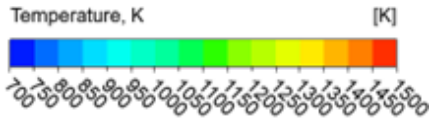

Figure 6.7: Turbine inlet temperature and iso-surface of T=1300K.

Because of the circumferentially relative location of the hot-streak vortical flow structure presented in Figure 6.7, the turbine vanes (stators) are exposed to different incoming flow temperature. Figure 6.8 shows the turbine vane wall temperature on the suction surface (SS) for the mid-passage hot-streak case (Figure 6.8a) and the leading-edge hot-streak case (Figure 6.8b). It can be seen clearly that the hot-streak impingement on the leading-edge (Figure 6.8b) significantly increases the turbine vane wall temperature. The affected area tends to be at the lower half span and it is more significant near the leading edge (LE). The high-temperature area diminishes as the flow approaches the blade trailing edge (TE). The high-temperature area exhibits the characteristic of the vortical flow structure wrapping around the turbine vane shown in Figure 6.7b. In addition, the lift-up area near the hub wall resembles that of the secondary passage vortex in the turbine cascade [101].

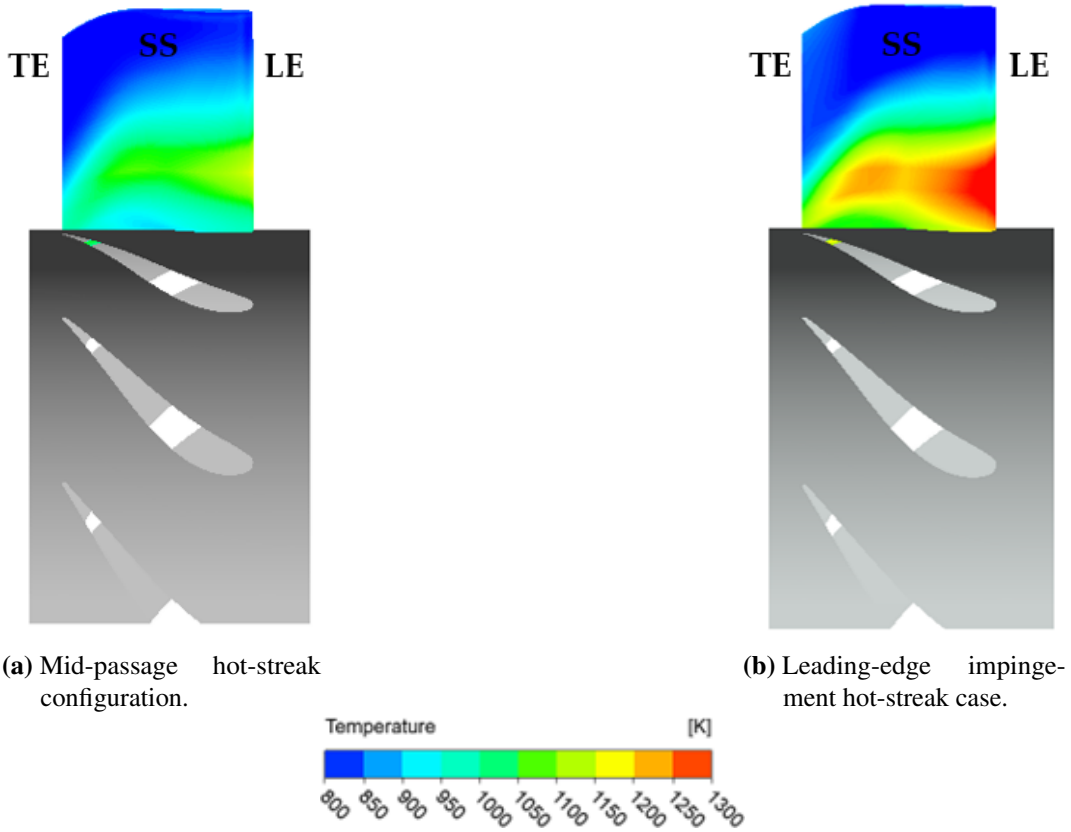

(a) Mid-passage hot-streak configuration.

(b) Leading-edge impingement hot-streak case.

Figure 6.8: Turbine stator blade suction surface wall temperature for different hot-streak configurations.

On the other hand, Figure 6.9 shows the turbine vane wall temperature on the pressure surface (PS) for the mid-passage hot-streak case (Figure 6.9a) and the leading-edge hot-streak case (Figure 6.9b). Similarly to what has been observed from Figure 8, the leading-edge impingement case (Figure 6.9b) exhibits a significantly higher wall temperature compared to the mid-passage case (Figure 6.9a). The most affected area is also the lower half span and near the leading edge (LE). Combining the observations from Figure 6.8 and Figure 6.9, it can be deduced that the relative location of the hot-streak impingement and the turbine vane significantly affects the blade aerothermal performances. Exposure of high wall temperature will lead to a shorter turbine life span due to increasing thermal stress.

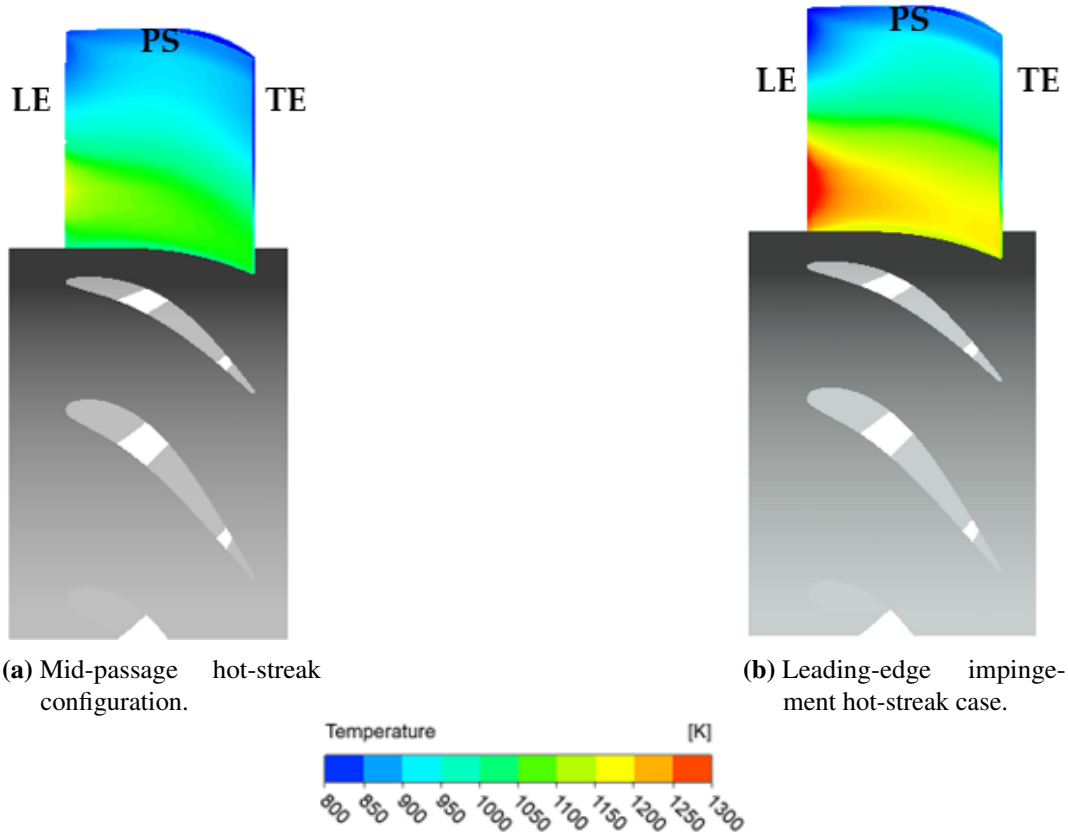

(a) Mid-passage hot-streak configuration.

(b) Leading-edge impingement hot-streak case.

Figure 6.9: Turbine stator blade pressure surface wall temperature for different hot-streak configurations.

Figure 6.10 shows the contour of the fuel Jet-A concentration at the axial location of turbine stator inlet. Non-zero Jet-A gaseous fuel concentration downstream the combustor outlet suggests that fuel is not entirely combusted inside the combustor domain. Unburnt fuel propagates downstream across the turbine stage, carried by the vortical structures seen previously (e.g. Figure 6.7). Fuel concentration is highest in the mid-span region and its distribution resembles that of the hot streak vortex.

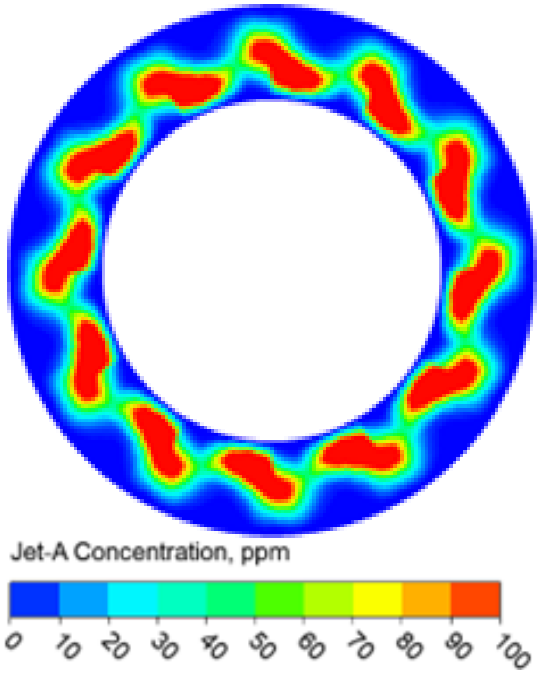

Figure 6.10: Jet-A concentration at turbine stator inlet, representing the amount of unburned fuel.

Figure 6.11 illustrates the transportation of unburned Jet-A fuel after the combustion chamber for case a) with hot streak passing through the passage and case b) with hot streak impinging onto the turbine vane leading edge. Firstly, Jet-A fuel concentration clearly decays along the axial flow direction, indicating that combustion still takes place after the combustor and inside the turbine stage. The rate of decay of Jet-A fuel is rapid with most of the unburned fuel combusted after passing the turbine vane row. It is interesting to visualize that Figure 6.11a and Figure 6.11b show two different decaying characteristics. In Figure 6.11a, the zone of large unburned Jet-A concentration passes through the turbine vane row with less decay compared to Figure 6.11b, where the zone impinges onto the vane leading edge. Halfway

through the turbine vane row, Jet-A decays more significantly in Figure 6.11b. After the turbine vane row, the flow goes onto the next turbine rotor row, at which Jet-A concentration is almost fully combusted in both cases.

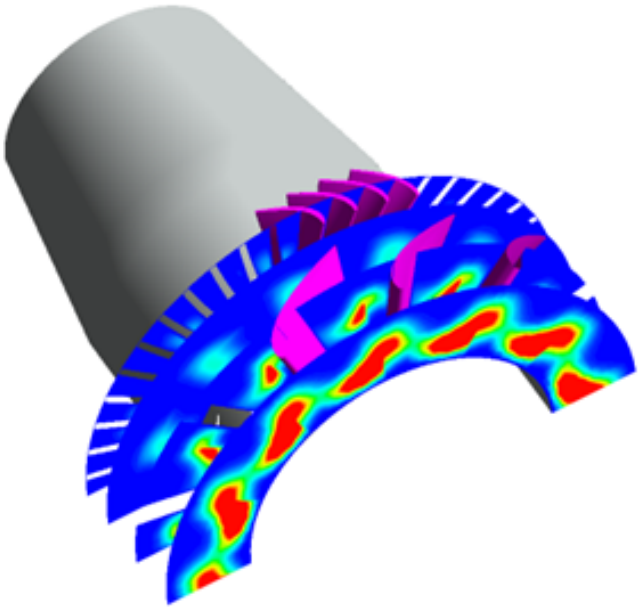

(a) Mid-passage hot-streak configuration.

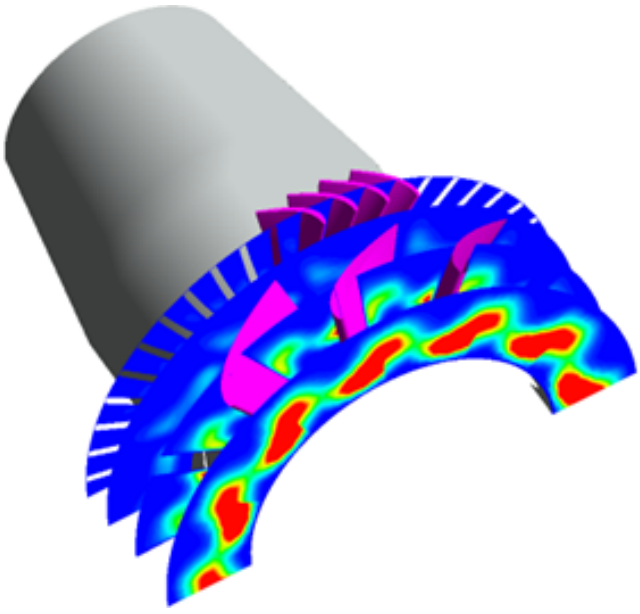

(b) Leading-edge impingement hot-streak case.

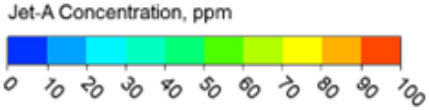

Figure 6.11: Unburned jet-A fuel transportation across the turbine stage for different hot-streak configurations.

Figure 6.12 shows the average Jet-A fuel concentration distribution across the turbine stage. The averaging is performed as mass flow weighted at a constant axial location for all circumferential and radial value points. For both leading-edge and mid-passage hot-streak case, the Jet-A fuel concentration decays rapidly after the combustor outlet. However, the decay rate is discernible across the blade rows, with a more significant rate for the leading-edge hot-streak configuration. This is due to the leading-edge impingement effect described above, where the vortical structure carries unburned fuel, impinges on the turbine vane, and enhances the secondary combustion process in the turbine stage. For both cases, the Jet-A fuel concentration after the turbine stage almost diminishes to zero suggesting that the combustion process finishes.

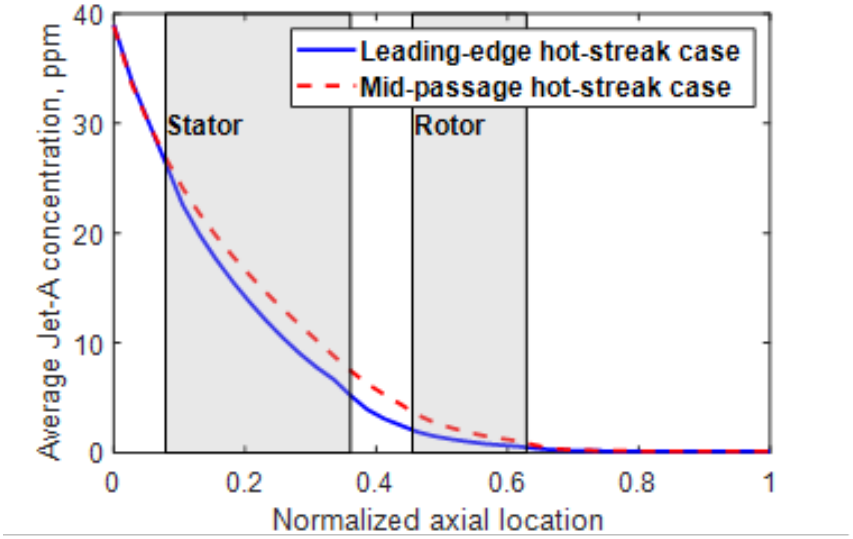

Figure 6.12: Decay of Jet-A fuel concentration across the turbine stage.

Figure 6.13 illustrates the formation and transportation of soot after the combustor for case a) with hot streak passing through the passage and case b) with hot streak impinging onto the turbine vane leading edge. From the combustor study, we know that as the combustion process takes place, Jet-A concentration decreases and combustion products such as soot concentration increases. From Figure 6.12, we observe that Jet-A concentration decreases as the flow goes through the turbine stage. As a result, it is expected that soot concentration would increase across the turbine stage. In Figure 6.13, the additional soot formation cannot be clearly observed and

the soot transportation pattern is also not clearly discernible between Figure 6.13a and Figure 6.13b. The common characteristics in both cases are such that the soot distribution preserves their shapes across the turbine vane row but diffuses across the turbine rotor row.

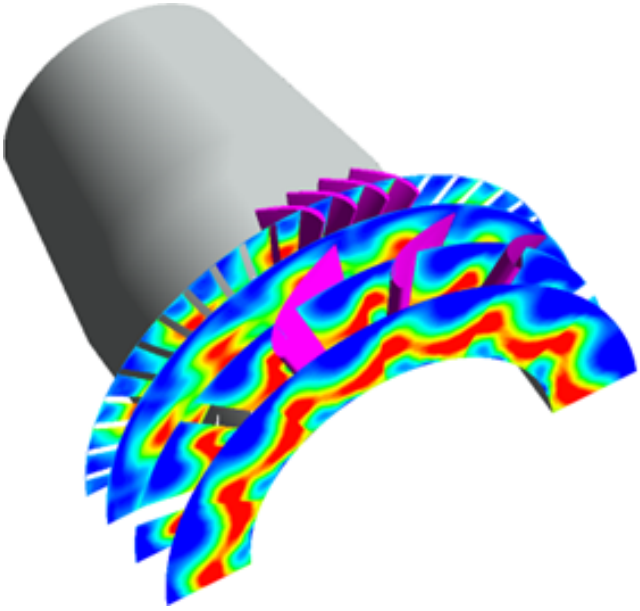

(a) Mid-passage hot-streak configuration.

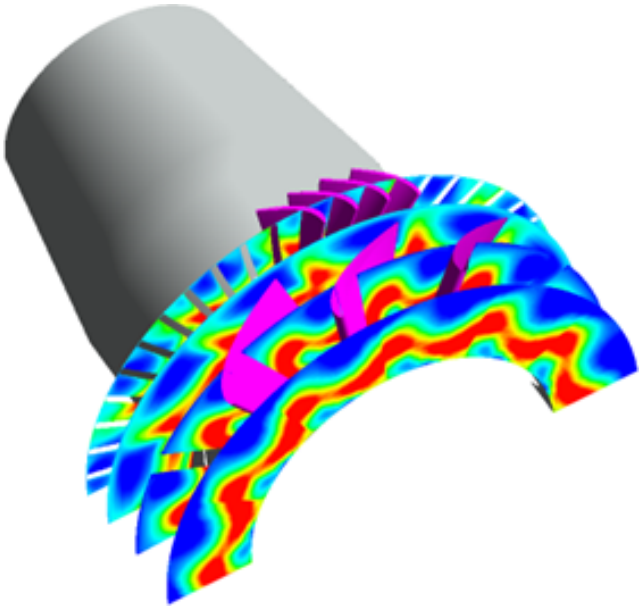

(b) Leading-edge impingement hot-streak case.

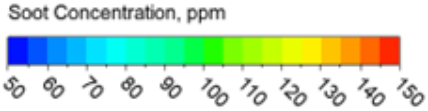

Figure 6.13: Soot evolution and transportation across the turbine stage for different hot-streak configurations.

Figure 6.14 shows the average soot concentration distribution across the turbine stage. The averaging is performed as mass flow weighted at a constant axial location for all circumferential and radial value points. The overall trend is the same for both leading-edge and mid-passage hot-streak cases with a linear increase in soot concentration as the flow travels downstream. The soot concentration of the leading-edge hot-streak case is slightly higher than that of the mid-passage hot-streak case for all axial locations across the turbine stage.

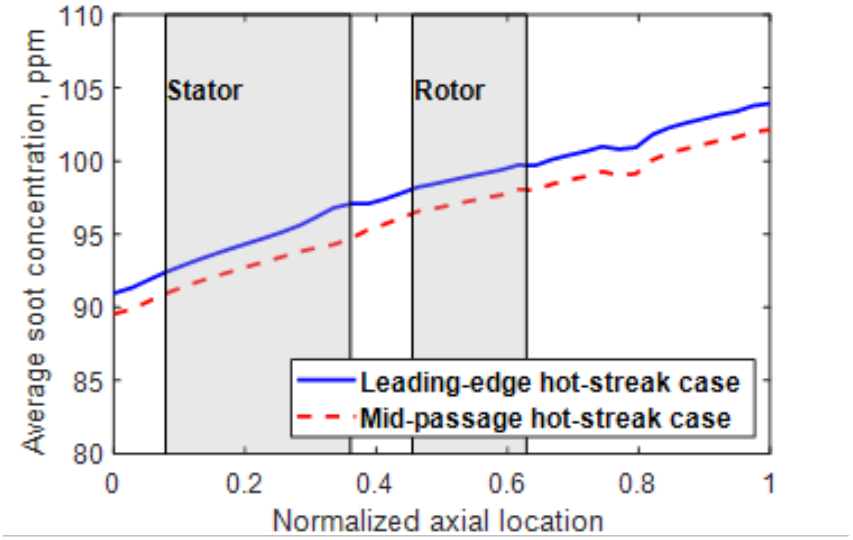

Figure 6.14: Accumulation of soot concentration across the turbine stage.

6.5 Effects of Stator Clocking

In the previous section, the relative circumferential location of hot-streak impingement and the turbine vane have been shown to have pronounced effects on the micro gas turbine aerothermal performance and emission characteristics. In this section, the relative circumferential location will be investigated in more detail using the design variable known as clocking. Clocking is the control of relative location between the combustor and the turbine stator, which effectively implies the control of the circumferential location of hot-streak relative to the turbine vane. Each revolution of the clocking period is defined as th

$$\Phi = \frac{N_b}{2\pi} \tag{6.1}$$

where Φ is the angle in radians of each complete clocking revolution; N_b is the number of turbine vanes in the blade row.

Figure 6.15 illustrates the clocking concept. Both combustion chamber and turbine vanes are stationary components, however their relative circumferential locations can be a design variable (i.e. clocking). In Figure 6.15, θ is the circumferential direction and x is the axial direction. The vaporising tubes in the combustion chamber can act as the anchor points, while the turbine vanes can move circumferentially. Figure 6.15a demonstrates the example of mid-passage clocking configuration and Figure 6.15b demonstrates the example of leading-edge impingement clocking configuration. Physical realisation of the clocking design can be done by adjusting the assembly of the stationary components.

For each complete clocking revolution, multiple clocking positions will be simulated and compared to investigate the clocking effects.

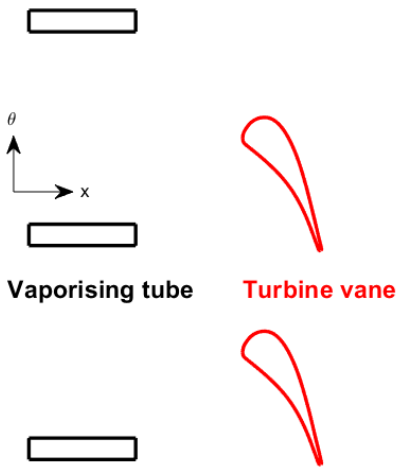

(a) Mid-passage clocking configuration.

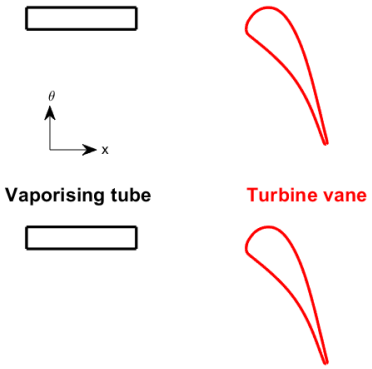

(b) Leading-edge impingement clocking configuration.

Figure 6.15: Illustration of the clocking concept (not to scale).

6.5.1 Combustor efficiency

In present simulations, clocking positions are adjusted by changing the circumferential location of the turbine vane blade row while keeping the combustor stationary. Firstly, the effects of stator clocking on the combustor efficiency are investigated. The combustion efficiency is calculated from the equation below:

$$T_{04} = T_{03} + \frac{\eta_{cc} \cdot f \cdot HV}{c_{pg}} \tag{6.2}$$

where T_{04} is the average total temperature at the combustor exit; T_{03} is the average total temperature at the combustor inlet; η_{cc} is the combustion efficiency; f is the

fuel-to-air ratio; $HV = 43.1MJ/kg$ is the heating value for Jet-A fuel; c_{pg} is the gas specific heat.

Figure 6.16 shows the variation of normalized combustor efficiency with clocking positions. It can be seen that the combustor efficiency varies in a sinusoidal pattern with a very small amplitude. Figure 6.16 suggests that clocking effects propagate upstream and affect the combustor aerothermodynamics although its impact is small. The peak of the sinusoidal curve in Figure 6.16 is the case with hot-streak leading-edge impingement, while the trough is the case with hot-streak mid-passage impingement. The interaction between the downstream combustor flow and the turbine vanes seems to slightly enhance the combustor efficiency.

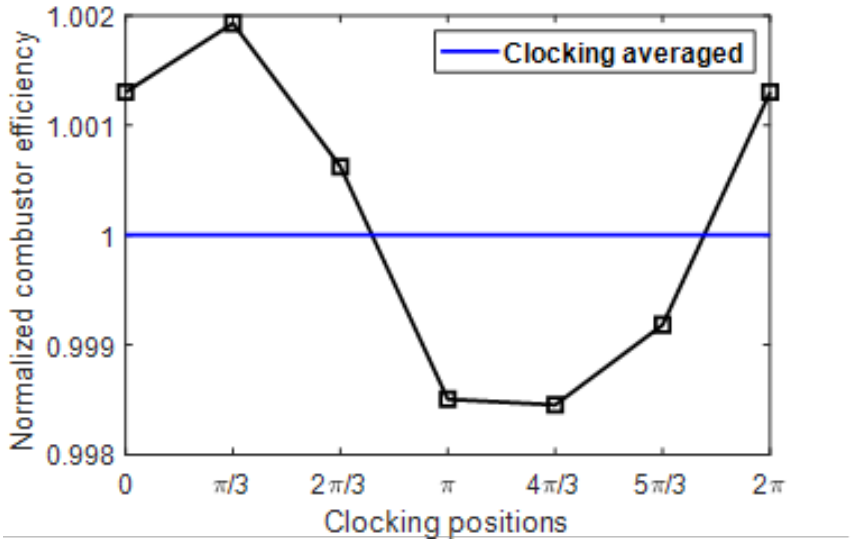

Figure 6.16: Effects of clocking on the normalized combustor efficiency.

6.5.2 Turbine aerodynamics efficiency

Figure 6.17 shows the variation of normalized turbine aerodynamic efficiency with clocking positions. The turbine isentropic efficiency η is calculated as:

$$\eta = \frac{1 - Tr}{1 - Pr^{\frac{\gamma-1}{\gamma}}} \tag{6.3}$$

where Tr and Pr are the temperature ratio and pressure ratio across the turbine stage, respectively; γ is the ratio of the specific heats.

The turbine aerodynamic efficiency varies largely in a sinusoidal pattern with a small amplitude. Although the flow field and vortical structure are quite different among the clocking positions (as seen in previous discussions), the turbine aerodynamic efficiency is not significantly affected. This is attributed to the effects of the rotor operation, which diffuses the flow significantly and enhances mixing. The peak of the near sinusoidal curve in Figure 6.17 is the case with hot-streak leading-edge impingement, while the trough is the case with hot-streak mid-passage impingement. There is a sudden jump between the clocking position $\Phi = \frac{4\pi}{3}$ and $\Phi = \frac{5\pi}{3}$ but the origin of this variation is not well understood. In general, the interaction between the downstream combustor flow and the turbine vanes seems to slightly enhance the turbine efficiency.

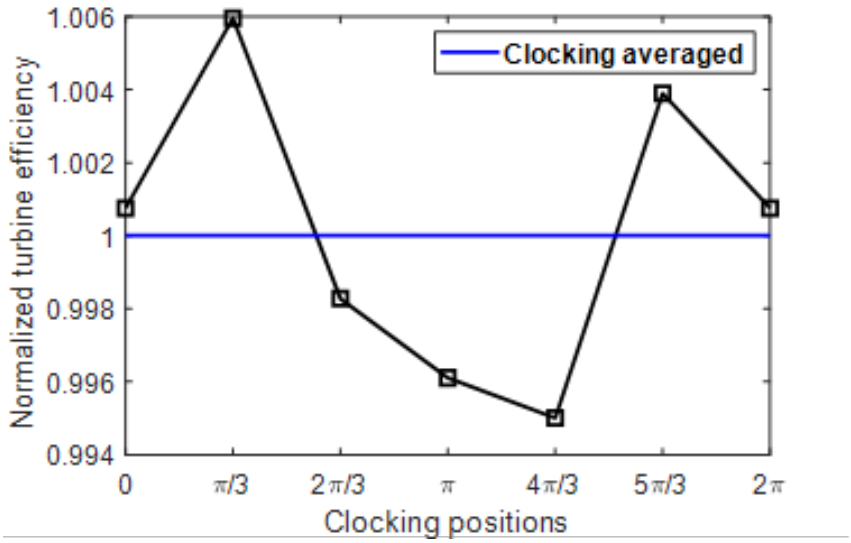

Figure 6.17: Effects of clocking on the normalized turbine efficiency.

6.5.3 Turbine heat transfer

Figure 6.18 shows the clocking effects on the normalized area-averaged turbine stator wall temperature. The stator wall temperature changes dramatically with clocking positions and exhibits a sinusoidal pattern. The peak of the sinusoidal curve in Figure 6.18 is the case with hot-streak leading-edge impingement, while the trough is the case with hot-streak mid-passage impingement. This confirms our qualitative observations in the previous section about the effects of hot-streak location on the turbine stator wall temperature.

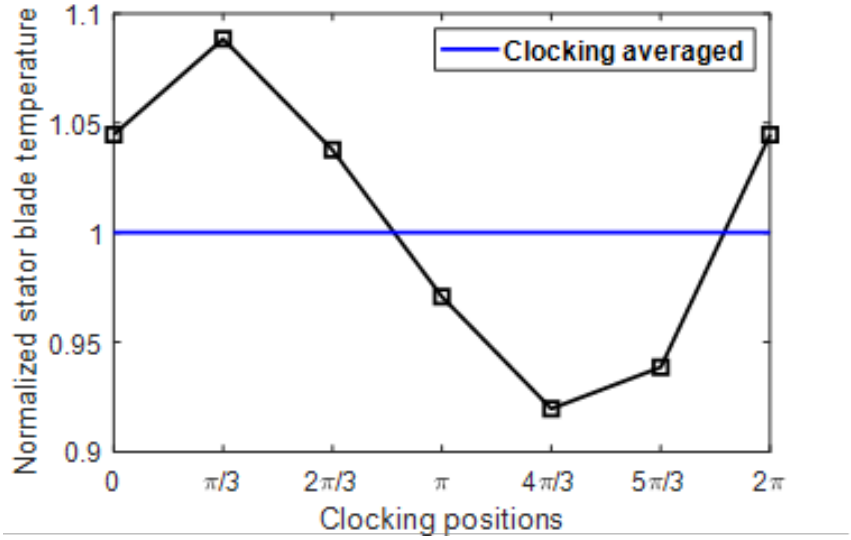

Figure 6.18: Effects of clocking on the normalized area-averaged turbine stator wall temperature.

Figure 6.19 shows the clocking effects on the normalized area-averaged turbine rotor wall temperature. It is quite interesting to observe that the rotor wall temperature only slightly changes with clocking positions, unlike previous observations with the stator wall temperature (Fig. 6.18). This effect might be attributed to two sources: 1) the significant decay of bulk flow temperature when passing through the stator blade row and 2) the rapid diffusion and mixing effects of the rotor with rotational effects in action. The peak of the sinusoidal curve in Figure 6.19 is the case with hot-streak leading-edge impingement, while the trough is the case with hot-streak mid-passage impingement.

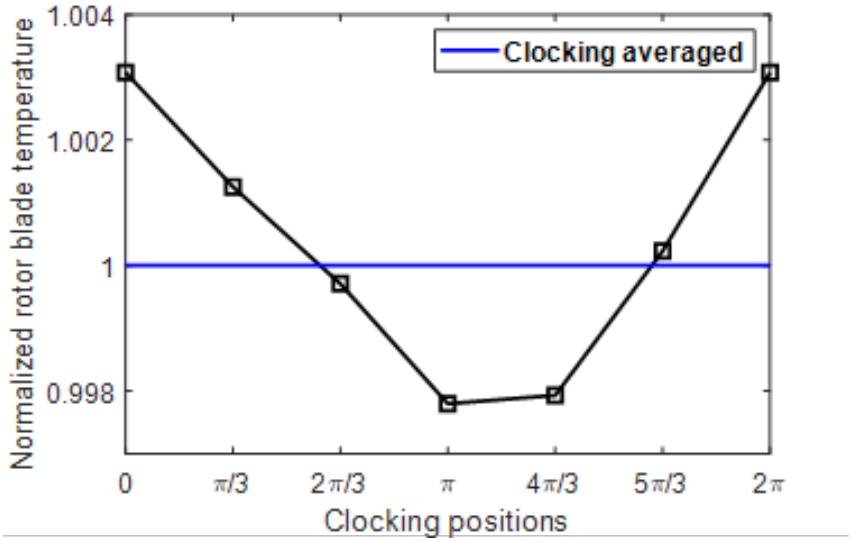

Figure 6.19: Effects of clocking on the normalized area-averaged turbine rotor wall temperature.

Combining the observations in Figure 6.18 and Figure 6.19, it can be deduced that the heat transfer performance of the turbine stator blade row is significantly affected by the clocking effects. The rotor heat transfer performance is only slightly affected.

6.5.4 Soot formation

Figure 6.20 illustrates the variation of normalized soot emissions with clocking positions. Soot emission varies in a sinusoidal pattern with a rather small amplitude. The peak of the sinusoidal curve in Figure 6.20 is the case with hot-streak leading-edge impingement, while the trough is the case with hot-streak mid-passage impingement, in agreement with the previous findings. This is due to the combustion of unburned fuel in the turbine stage and mixing enhancement due to the hot-streak leading-edge impingement. It is additional evidence that the complex interplay of the flow field can affect the pollutant emission characteristics.

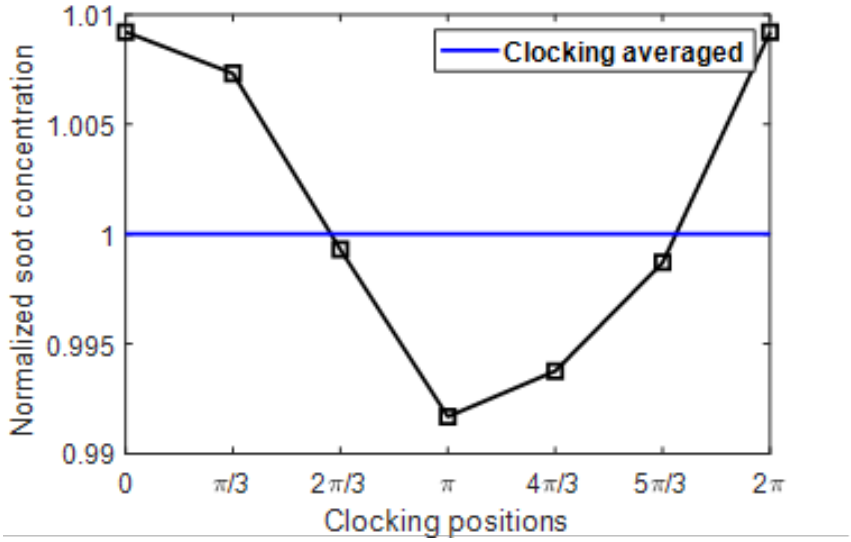

Figure 6.20: Effects of clocking on the normalized soot concentration.

6.6 Summary

In the present chapter, the interaction between the combustor and the turbine is investigated more in detail with a focus on the clocking effects. Both studies are parts of a more comprehensive project aimed at understanding the fundamental aerothermal performance and emission characteristics of a micro gas turbine model and finding ways to improve its operation. A complex Computational Fluid Dynamics (CFD) model was developed in this project that has the capability to model the reacting flow in the combustion chamber and its transportation downstream across the turbine stage. The model is high-fidelity with the full coupling between the combustor and the turbine stage domain. In addition, the annular domain is modelled as a whole annulus without any truncation in the domain and there is no use of periodic boundary conditions. With such high modelling fidelity, the present study provides many useful insights and understanding into the interaction between the combustor and the turbine stage with a particular focus on the complex interplay among the flow field, aerothermal performance, and soot emissions. The main points are briefly summarized below:

- The sequential decoupled modeling approach is not as accurate as the fully-coupled modeling approach because the unburnt fuel at the combustor outlet

continues its combustion process in the turbine stage and the upstream propagation effect is not fully captured. Both predictions of aerothermal performance and emission characteristics are affected by the choice of modeling approach. At first the sequential decoupled approach seems to be more efficient since only a few coupling iterations are needed. However, the present study shows that the sequential decoupled simulation approach will struggle to converge to a tight tolerance because the flow field settles slowly in response to the continuous changes in boundary conditions. The fully-coupled simulation approach is more accurate and easier to converge at the cost of high memory due to a large simulation domain.

- Unburned gaseous Jet-A fuel travels downstream of the combustion chamber and into the turbine stage domain within the vortical flow structure. The combustion process still takes place inside the turbine domain. The Jet-A fuel concentration decays rapidly across the turbine domain, while soot concentration increases linearly.

- The relative circumferential location of the combustion chamber and the turbine vane (clocking effects) has been shown to affect the aerothermodynamics and pollutant emissions of the micro-gas turbine. The leading-edge impingement hot-streak configuration is favored in terms of improving aerodynamic efficiency. On the other hand, the mid-passage hot-streak configuration is favored in terms of reducing aerothermal heat load and reducing soot emissions. Although all aerothermodynamic and pollutant emissions parameters are affected by the clocking effects, the turbine vane heat load is the most significantly affected parameter (up to 10% for the peak and trough compared to the averaged value).

Chapter 7

Conclusions and Future Works

7.1 Conclusions

In this thesis, an extensive numerical investigation into the aerothermodynamic mechanisms of a micro-gas turbine with realistic geometry was undertaken, revealing several pivotal findings.

Chapter 4 introduced the dump diffuser combustor as a fundamental representation of a gas turbine combustion chamber. This exploration revealed that geometrical parameters, particularly the pre-diffuser divergence angle and the dump gap ratio, play a significant role in determining aerodynamic performance. Simultaneously, the study also showcased the potential of the inlet boundary layer adjustments. By manipulating its thickness and radial skewness, designers can unlock avenues for enhanced performance, especially when synergized with the compressor vane exit flow conditions.

Progressing to Chapter 5, the aerothermal performance and emission characteristics of a micro-gas turbine combustor were analyzed. This investigation unveiled that standard cycle-based boundary conditions might not accurately represent the complex flow dynamics. As a result, combustion efficiency and soot emission evaluations can be inaccurate. Furthermore, the dynamics of the fuel-to-air ratio emerged as a critical parameter, profoundly influencing combustion hot-spots, efficiency, and even soot emissions. Another intriguing discovery was the relationship between the fuel injection velocity and soot emissions. Although the former does not majorly

impact combustion efficiency, it does exhibit a significant correlation with soot emissions.

Transitioning to Chapter 6, the complex interaction between the combustor and the turbine was investigated with emphasis on the clocking effects. The study established that while sequential decoupled modeling appears initially promising, its accuracy deteriorates in comparison to a fully-coupled approach. This chapter also highlighted the flow path of unburned Jet-A gaseous fuel from the combustion chamber into the turbine stage, marking a sharp decline in Jet-A fuel concentration and a linear rise in soot emissions. Moreover, the circumferential positioning or ”clocking” of the combustion chamber in relation to the turbine vane emerged as a determinant factor influencing aerothermodynamics and pollutant emissions. Notably, the turbine vane heat load was identified as the most affected parameter by these clocking effects, with noticeable variations impacting performance.

7.2 Answers to Research Questions

Question 1: *What is the role of combustion modelling in the prediction of micro-gas turbine performance?*

Answer 1: Combustion modelling can influence the prediction of aerodynamic performance of the turbine stage. Unburned fuel can travel downstream the turbine vane, creating a higher temperature field and affecting affecting the heat transfer performance.

Question 2: *How do components in a micro-gas turbine interact with each other?*

Answer 2: The combusted gas and unburned fuel can travel downstream from the combustion chamber to the turbine stage. The unburned fuel can continue the combustion in the stator row, creating further heat load on the turbine vane and more soot emissions. On the other hand, the potential effect of the turbine can affect the combustion flow field chamber upstream, results in an under-prediction of hot-spot peak temperature and soot emission.

Question 3: *Is it possible to exploit these component interactions to enhance*

performance and/or reduce emission?

Answer 3: Yes, clocking the combustion chamber and turbine vanes at a right angle can influence the aerothermodynamics performance and soot emission. Leading-edge hot streak impingement clocking would increase aerodynamic efficiency. On the other hand, mid-passage clocking would reduce the the turbine vanes' heat load and reduce soot emissions.

7.3 Strengths and Limitations of The Study

7.3.1 Strengths

The present thesis demonstrates results of a comprehensive project aimed at understanding the fundamental aerothermal performance and emission characteristics of a micro-gas turbine model and finding ways to improve its operation. A complex CFD model has been developed throughout the thesis that has the capability to model the reacting flow in the combustion chamber and its transportation across other components. The strengths of the proposed approach are:

- Realistic geometries: real micro-gas turbine geometries have been sourced, reconstructed, modelled, and validated in this thesis. This strength demonstrates the practicality of the thesis on further applications including analysis and design optimization of a complex machinery.

- Full coupling: all micro-gas turbine components are connected in a single mesh. Thus, flow field information pass easily across the interface without the need of a special interface treatment.

- Whole annulus: the whole annular bladerows are modelled, preventing the truncation errors due to the periodic boundary conditions. In addition, the whole annulus domain also facilitates easier component interfacing.

- Reacting flow: unlike various prior investigations in the open literature where unreacting flow model is used to evaluate the performance of a turbine stage, and even a combustor in some cases, the model presented in the thesis not only models reacting flow in the combustor but also models the transportation of

the multi-species gas across the turbine stage. The model enables observation of several important features such as the flow of unburned gaseous fuel and its subsequent reaction in the turbine domain.

- Soot modelling: another feature of the chosen modelling approach is the model of soot nucleation, formation, and transportation in both the combustor and turbine domains. As the pursuit of emission reduction continues to rise, the understanding of this subject matter attract more attention.

Thus, it can be seen that the numerical simulation approached adopted in the present thesis is complex and highly accurate with several physical processes and transport phenomena modelled.

7.3.2 Limitations

On the other hands, the chosen numerical simulation approach still have some limitations:

- Steady-state: the steady-state CFD solver is chosen, which greatly reduces the computational cost. However, the time-varying performance of the micro-gas turbine cannot be resolved. Nevertheless, the mean performance is typically the variable of interest. It is argued that the steady-state solution is different to the average of the time-varying solution. The extent of difference depends on the level of nonlinearity, which may come from the turbulence, the flame, combustion products formation and transport, and the interactions among them. Using the steady-state CFD solver, it is assumed that the nonlinearity level is small. This assumption might introduce some inaccuracies.

- Adiabatic walls: the adiabatic no-slip wall boundary conditions are used at the micro-gas turbine component surfaces. Although the no-slip wall boundary condition is accurate for viscous flow simulation, the use of adiabatic wall boundary condition neglect the effects of heat transfer to and from the walls. Since the combustion temperature is high, the heat transfer will be likely to conduct across the metal wall and increase their wall temperatures. As

a result, the exposed components will be exposed to high heat sources and their lifetime will be reduced. If the bulk aerodynamic performance is of interest, the adiabatic wall boundary condition shall be sufficient. If the metal temperature is required (e.g. for lifing purposes), the conjugate heat transfer model might be needed. The conjugate heat transfer model will increase the computational time and cost because the heat conduction across the metal surface needs to be solved, together with the external flow field.

- Computational memory and storage: the chosen numerical simulation approach requires a large amount of computational memory (RAM) and storage compared to the conventional uncoupled simulation approach or the reduced-order modelling. However, the results will be more accurate since less assumptions are made.

7.4 Suggested Future Works

Owing to time constraints and computational resource limitations, not all planned investigations were conducted. This section proposes recommendations for subsequent studies, building on the insights from this thesis.

7.4.1 Compressor-Combustor Interaction

The results from Chapter 4 underscored potential interactions between the compressor and the combustor. A comprehensive study of the interaction, akin to the method in Chapter 5, is encouraged.

7.4.2 High-Fidelity Turbulence Resolved

While the combustion chamber was modeled using a RANS-based solver due to constrained numerical simulation resources, it lacks accuracy. Especially for combustion flow, advanced turbulence resolved methods like Large Eddy Simulation (LES) or hybrid approaches such as Detached Eddy Simulation (DES) or Stress Blended Eddy Simulation (SBES) are essential. Adopting these methods would necessitate considerably more computational resources, especially for a whole-annulus fully-coupled domain.

7.4.3 Unsteady Bladerow Simulations

Further exploration of unsteady bladerow simulation methods should be sought for. In this thesis, the Frozen Rotor approach was adopted. Models like the sliding plane offer deeper insights into instantaneous component interactions.

7.4.4 Effects of Fuel Type

Given the significance in micro-gas turbine applications, assessing various fuel types (e.g., biofuels, hydrogen) is essential. The modeling framework presented in this thesis can be adapted to investigate fuel versatility in micro-gas turbine designs or to evaluate the viability of emerging fuels.

7.4.5 Different Operating Points

This thesis centered on the peak thrust operating condition. Investigating off-design points, especially at lower speeds, is essential. An exploration is needed to determine if the current findings remain relevant across diverse operating scenarios.

Bibliography

[1] J. Xiang. *Miniature gas turbines: numerical study of the effects of miniaturization on the performance of compressor*. PhD thesis, Nanyang Technological University, 2015.

[2] R. Pavri and G. D. Moore. Ger 4211-gas turbine emissions and control. *GE Power Systems*, 2001.

[3] A. H. Lefebvre. The Role of Fuel Preparation in Low-Emission Combustion. *Journal of Engineering for Gas Turbines and Power*, 117(4):617–654, 10 1995.

[4] Y. Liu, X. Sun, V. Sethi, D. Nalianda, Y.-G. Li, and L. Wang. Review of modern low emissions combustion technologies for aero gas turbine engines. *Progress in Aerospace Sciences*, 94:12–45, 2017.

[5] S. Jacobi, C. Mazzoni, B. Rosic, and K. Chana. Investigation of Unsteady Flow Phenomena in First Vane Caused by Combustor Flow With Swirl. *Journal of Turbomachinery*, 139(4):041006, 01 2017.

[6] B. Rosic, J. D. Denton, J. H. Horlock, and S. Uchida. Integrated Combustor and Vane Concept in Gas Turbines. *Journal of Turbomachinery*, 134(3):031005, 07 2011.

[7] J. Li, G. Page, and J. McGuirk. Coupled reynolds-averaged navier–stokes/large-eddy simulation for outlet guide vane and prediffuser flows. *AIAA Journal*, 53(3):678–691, 2015.

[8] A. D. Walker, J. F. Carrotte, and J. J. McGuirk. Enhanced External Aerodynamic Performance of a Generic Combustor Using An Integrated OGV/Prediffuser Design Technique. *Journal of Engineering for Gas Turbines and Power*, 129(1):80–87, 02 2006.

[9] C. U. Buice. *Experimental investigation of flow through an asymmetric plane diffuser*. Stanford University, 1997.

[10] K. Schreckling. *Home built model turbines*. Traplet Publications Limited, 2005.

[11] C. Yang, H. Wu, J. Du, H. Zhang, and J. Yang. Full-engine simulation of micro gas turbine based on time-marching throughflow method. *Applied Thermal Engineering*, 217:119213, 2022.

[12] H. Wang and K. H. Luo. Numerical Investigation of Dump Diffuser Combustor Performance at Uniform and Non-Uniform Inlet Conditions. In *Turbo Expo: Power for Land, Sea, and Air Volume 4B: Combustion, Fuels, and Emissions*, page V04BT04A030, 09 2020.

[13] H. Wang and K. H. Luo. Aerothermal performance and soot emissions of reacting flow in a micro-gas turbine combustor. *Energies*, 16(7):2947, 2023.

[14] H. Wang and K. H. Luo. Fully coupled whole-annulus investigation of combustor–turbine interaction with reacting flow. *Energies*, 17(4):873, 2024.

[15] A. H. Lefebvre and D. R. Ballal. *Gas turbine combustion: alternative fuels and emissions*. CRC press, 2010.

[16] W. S. Y. Hung. Accurate method of predicting the effect of humidity or injected water on nox emissions from industrial gas turbines. In *ASME Paper No. 74-WA/GT-6.*, 1974.

[17] M. B. Hilt and J. Waslo. Evolution of NOx Abatement Techniques Through Combustor Design for Heavy-Duty Gas Turbines. *Journal of Engineering for Gas Turbines and Power*, 106(4):825–832, 10 1984.

[18] D. McKnight. Development of a Compact Gas Turbine Combuster to Give Extended Life and Acceptable Exhaust Emissions. *Journal of Engineering for Power*, 101(3):349–357, 07 1979.

[19] G. Poeschl, W. Ruhkamp, and H. Pfost. Combustion With Low Pollutant Emissions of Liquid Fuels in Gas Turbines by Premixing and Prevaporization. In *Turbo Expo: Power for Land, Sea, and Air Volume 3: Coal, Biomass and Alternative Fuels; Combustion and Fuels; Oil and Gas Applications; Cycle Innovations*, page V003T06A044, 06 1994.

[20] G. Leonard and J. Stegmaier. Development of an Aeroderivative Gas Turbine Dry Low Emissions Combustion System. *Journal of Engineering for Gas Turbines and Power*, 116(3):542–546, 07 1994.

[21] S. A. Mosier and R. M. Pierce. Advanced combustion systems for stationary gas turbine engines. In *Proceedings of the second stationary source combustion symposium*, 1980.

[22] R. McKinney, A.t Cheung, W. Sowa, and D. Sepulveda. The pratt & whitney talon x low emissions combustor: revolutionary results with evolutionary technology. In *45th AIAA aerospace sciences meeting and exhibit*, page 386, 2007.

[23] R. Smith. Advanced low emissions subsonic combustor study. Number NASA/CR-1998-207931, 1998.

[24] J. B. Howard and W. J. Kausch Jr. Soot control by fuel additives. *Progress in Energy and Combustion Science*, 6(3):263–276, 1980.

[25] M. C. Chiong, C. T. Chong, J. H. Ng, S. S. Lam, M. V. Tran, W. W. F. Chong, M. N. Mohd Jaafar, and A. Valera-Medina. Liquid biofuels production and emissions performance in gas turbines: A review. *Energy Conversion and Management*, 173:640–658, 2018.

[26] C. M. Cha, S. Hong, P. T. Ireland, P. Denman, and V. Savarianandam. Experimental and Numerical Investigation of Combustor-Turbine Interaction Using an Isothermal, Nonreacting Tracer. *Journal of Engineering for Gas Turbines and Power*, 134(8):081501, 06 2012.

[27] S. Jacobi and B. Rosic. Thermal investigation of integrated combustor vane concept under engine-realistic conditions. *Journal of Turbomachinery*, 139(2):021005, 2017.

[28] S. Jacobi and B. Rosic. Influence of combustor flow with swirl on integrated combustor vane concept full-stage performance. *Journal of Turbomachinery*, 140(1):011002, 2018.

[29] Y. Huang and V. Yang. Dynamics and stability of lean-premixed swirl-stabilized combustion. *Progress in energy and combustion science*, 35(4):293–364, 2009.

[30] S. Jacobi and B. Rosic. Development and Aerothermal Investigation of Integrated Combustor Vane Concept. *Journal of Turbomachinery*, 138(1):011002, 10 2015.

[31] I. Aslanidou and B. Rosic. Aerothermal Performance of Shielded Vane Design. *Journal of Turbomachinery*, 139(11):111003, 07 2017.

[32] A. Andreini, T. Bacci, M. Insinna, L. Mazzei, and S. Salvadori. Hybrid RANS-LES Modeling of the Aerothermal Field in an Annular Hot Streak Generator for the Study of Combustor–Turbine Interaction. *Journal of Engineering for Gas Turbines and Power*, 139(2):021508, 09 2016.

[33] J. Hilgert, M. Bruschewski, H. Werschnik, and H. P. Schiffer. Numerical Studies on Combustor-Turbine Interaction at the Large Scale Turbine Rig (LSTR). In *Turbo Expo: Power for Land, Sea, and Air Volume 2A: Turbomachinery*, page V02AT40A028, 06 2017.

[34] F. Duchaine, J. Dombard, L. Gicquel, and C. Koupper. Integrated Large Eddy Simulation of Combustor and Turbine Interactions: Effect of Turbine Stage Inlet Condition. In *Turbo Expo: Power for Land, Sea, and Air Volume 2B: Turbomachinery*, page V02BT41A014, 06 2017.

[35] J. J. McGuirk. The aerodynamic challenges of aeroengine gas-turbine combustion systems. *The Aeronautical Journal*, 118(1204):557–599, 2014.

[36] A. D. Walker, J. F. Carrotte, and J. J. McGuirk. Compressor/Diffuser/Combustor Aerodynamic Interactions in Lean Module Combustors. *Journal of Engineering for Gas Turbines and Power*, 130(1):011504, 01 2008.

[37] A. D. Walker, J. F. Carrotte, and J. J. McGuirk. The Influence of Dump Gap on External Combustor Aerodynamics at High Fuel Injector Flow Rates. *Journal of Engineering for Gas Turbines and Power*, 131(3):031506, 02 2009.

[38] A. D. Walker, A. G. Barker, J. F. Carrotte, J. J. Bolger, and M. J. Green. Integrated Outlet Guide Vane Design for an Aggressive S-Shaped Compressor Transition Duct. *Journal of Turbomachinery*, 135(1):011035, 10 2012.

[39] J. U. Schlüter, H. Pitsch, and P. Moin. Large-eddy simulation inflow conditions for coupling with reynolds-averaged flow solvers. *AIAA journal*, 42(3):478–484, 2004.

[40] W. A. McMullan and G. J. Page. Towards large eddy simulation of gas turbine compressors. *Progress in Aerospace Sciences*, 52:30–47, 2012. Applied Computational Aerodynamics and High Performance Computing in the UK.

[41] G. Medic, D. You, and G. Kalitzin. An approach for coupling rans and les in integrated computations of jet engines. *Center for Turbulence Research, Annual Research Briefs*, pages 275–286, 2006.

[42] J. U. Schlüter, H. Pitsch, and P. Moin. Outflow conditions for intregrated large eddy simulation/reynolds-averaged navier-stokes simulations. *AIAA journal*, 43(1):156–164, 2005.

[43] K. V. Kannan and G. J. Page. Coupling of Compressible Turbomachinery and Incompressible Combustor Flow Solvers for Aerothermal Applications. In *Turbo Expo: Power for Land, Sea, and Air Volume 2A: Turbomachinery*, page V02AT40A004, 06 2014.

[44] J. Xiang, J. U. Schlüter, and F. Duan. Study of kj-66 micro gas turbine compressor: Steady and unsteady reynolds-averaged navier–stokes approach. *Proceedings of the Institution of Mechanical Engineers, Part G: Journal of Aerospace Engineering*, 231(5):904–917, 2017.

[45] Y. Xu, C. Yan, and Y. Piao. Analysis of discrepancies between 3-d coupled and uncoupled schemes based on cfd in full engine simulation. *Aerospace Science and Technology*, 131:107978, 2022.

[46] C. P. Arroyo, J. Dombard, F. Duchaine, L. Gicquel, B. Martin, N. Odier, and G. Staffelbach. Towards the large-eddy simulation of a full engine: Integration of a 360 azimuthal degrees fan, compressor and combustion chamber. part i: Methodology and initialisation. *Journal of the Global Power and Propulsion Society*, (Special issue):133115, 2021.

[47] Y. Xu, L. Gao, R. Cao, C. Yan, and Y. Piao. Power balance strategies in steady-state simulation of the micro gas turbine engine by component-coupled 3d cfd method. *Aerospace*, 10(9):782, 2023.

[48] T. Barth and D. Jespersen. The design and application of upwind schemes on unstructured meshes. In *27th Aerospace Sciences Meeting*, page 366, 1989.

[49] C. M. Rhie and W.-L. Chow. Numerical study of the turbulent flow past an airfoil with trailing edge separation. *AIAA Journal*, 21(11):1525–1532, 1983.

[50] C.-M. Lee, K. Kundu, and B. Ghorashi. Simplified jet-a kinetic mechanism for combustor application. In *Aerospace Sciences Meeting*, number E-7457, 1993.

[51] M. C. Cameretti, R. Piazzesi, F. Reale, and R. Tuccillo. Comparison of external and internal egr concepts for low emission micro gas turbines. In *Turbo Expo: Power for Land, Sea, and Air*, volume 43987, pages 581–593, 2010.

[52] M. C. Cameretti, R. Tuccillo, and R. Piazzesi. Study of an exhaust gas recirculation equipped micro gas turbine supplied with bio-fuels. *Applied Thermal Engineering*, 59(1-2):162–173, 2013.

[53] C. Xing, L. Liu, P. Qiu, W. Shen, Y. Lyu, Z. Zhang, H. Wang, S. Wu, and Y. Qin. Combustion performance of an adjustable fuel feeding combustor under off-design conditions for a micro-gas turbine. *Applied Energy*, 208:12–24, 2017.

[54] P. J. O'Rourke and A. A. Amsden. The tab method for numerical calculation of spray droplet breakup. Technical report, SAE Technical Paper, 1987.

[55] F. X. Tanner. Liquid jet atomization and droplet breakup modeling of non-evaporating diesel fuel sprays. *SAE transactions*, pages 127–140, 1997.

[56] F. X. Tanner. A cascade atomization and drop breakup model for the simulation of high-pressure liquid jets. *SAE transactions*, pages 1352–1366, 2003.

[57] R. D. Reitz and R. Diwakar. Structure of high-pressure fuel sprays. *SAE transactions*, pages 492–509, 1987.

[58] E. M. Wahba and H. Nawar. Multiphase flow modeling and optimization for online wash systems of gas turbines. *Applied Mathematical Modelling*, 37(14-15):7549–7560, 2013.

[59] D. Sedarsky, M. Paciaroni, E. Berrocal, P. Petterson, J. Zelina, J. Gord, and M. Linne. Model validation image data for breakup of a liquid jet in crossflow: Part i. *Experiments in fluids*, 49:391–408, 2010.

[60] H.-F. Liu, W.-F. Li, X. Gong, X.-K. Cao, J.-L. Xu, X.-L. Chen, Y.-F. Wang, G.-S. Yu, F.-C. Wang, and Z.-H. Yu. Effect of liquid jet diameter on performance of coaxial two-fluid airblast atomizers. *Chemical Engineering and Processing: Process Intensification*, 45(4):240–245, 2006.

[61] B. F. Magnussen. The eddy dissipation concept for turbulent combustion modelling. its physical and practical implications. In *The First Topic Oriented Technical Meeting*, 1989.

[62] P.A. Tesner, T.D. Smegiriova, and V.G. Knorre. Kinetics of dispersed carbon formation. *Combustion and Flame*, 17(2):253–260, 1971.

[63] S. Honami, W. Tsuboi, and T. Shizawa. Effect of the Flame Dome Depth and Improvement of the Pressure Loss in the Dump Diffuser. In *Turbo Expo: Power for Land, Sea, and Air Volume 3: Coal, Biomass and Alternative Fuels; Combustion and Fuels; Oil and Gas Applications; Cycle Innovations*, page V003T06A012, 06 1998.

[64] J. F. Carrotte, D. W. Bailey, and C. W. Frodsham. Detailed Measurements on a Modern Combustor Dump Diffuser System. *Journal of Engineering for Gas Turbines and Power*, 117(4):678–685, 10 1995.

[65] P. Ghose, A. Datta, and A. Mukhopadhyay. Effect of Prediffuser Angle on the Static Pressure Recovery in Flow Through Casing-Liner Annulus of a Gas Turbine Combustor at Various Swirl Levels. *Journal of Thermal Science and Engineering Applications*, 8(1):011017, 11 2015.

[66] A. Rahim, S. N. Singh, and S. V. Veeravalli. Liner dome shape effect on the annulus flow characteristics with and without swirl for a can-combustor model. *Proceedings of the Institution of Mechanical Engineers, Part A: Journal of Power and Energy*, 221(3):359–368, 2007.

[67] J. F. Carrotte, P. A. Denman, A. P. Wray, and P. Fry. Detailed Performance Comparison of a Dump and Short Faired Combustor Diffuser System. *Journal of Engineering for Gas Turbines and Power*, 116(3):517–526, 07 1994.

[68] P. He, J. Suo, K. Xie, S. Chen, S. Shen, and Q. Zeng. The influence of dump gap on aerodynamic performance of a low-emission combustor dump diffuser. In *Turbo Expo: Power for Land, Sea, and Air*, volume 55119, page V01BT04A017. American Society of Mechanical Engineers, 2013.

[69] C. R. Fishenden and S. J. Stevens. Performance of annular combustor-dump diffusers. *Journal of Aircraft*, 14(1):60–67, 1977.

[70] R. Srinivasan, W. Freeman, J. Grahmann, and E. Coleman. Parametric evaluation of the aerodynamic performance of an annular combustor-diffuser system. In *26th Joint Propulsion Conference*, page 2163, 1990.

[71] A. Klein. Characteristics of combustor diffusers. *Progress in Aerospace Sciences*, 31(3):171–271, 1995.

[72] A. G. Barker and J. F. Carrotte. Compressor Exit Conditions and Their Impact on Flame Tube Injector Flows . *Journal of Engineering for Gas Turbines and Power*, 124(1):10–19, 03 1999.

[73] A. D. Walker, J. F. Carrotte, and P. A. Denman. Annular diffusers with large downstream blockage effects for gas turbine combustion applications. *Journal of Propulsion and Power*, 27(6):1218–1231, 2011.

[74] A. Klein, P. Pucher, and M. Rohiffs. The Effect of Blade-Wakes on the Performance of Short Dump-Diffuser Type Combustor Inlets. *Journal of Fluids Engineering*, 102(2):236–241, 06 1980.

[75] G. Iaccarino. Predictions of a turbulent separated flow using commercial cfd codes. *Journal of Fluids Engineering*, 123(4):819–828, 2001.

[76] H.-J. Kaltenbach, M. Fatica, R. Mittal, T. S. Lund, and P. Moin. Study of flow in a planar asymmetric diffuser using large-eddy simulation. *Journal of Fluid Mechanics*, 390:151–185, 1999.

[77] S. Obi, K. Aoki, and S. Masuda. Experimental and computational study of turbulent separating flow in an asymmetric plane diffuser. In *Ninth Symposium on Turbulent Shear Flows*, volume 305, pages 305–312, 1993.

[78] P. Ghose, A. Datta, and A. Mukhopadhyay. Effect of prediffuser angle on the static pressure recovery in flow through casing-liner annulus of a gas turbine combustor at various swirl levels. *Journal of Thermal Science and Engineering Applications*, 8(1):011017, 2016.

[79] J. H. Wagner, R. P. Dring, and H. D. Joslyn. Inlet Boundary Layer Effects in an Axial Compressor Rotor: Part I—Blade-to-Blade Effects. *Journal of Engineering for Gas Turbines and Power*, 107(2):374–380, 04 1985.

[80] J. D. Denton. Some limitations of turbomachinery cfd. In *Turbo Expo: Power for Land, Sea, and Air*, volume 44021, pages 735–745, 2010.

[81] H. M. Phan and L. He. Validation studies of linear oscillating compressor cascade and use of influence coefficient method. *Journal of Turbomachinery*, 142(5):051005, 2020.

[82] A. Duncan Walker, J. F. Carrotte, and J. J. McGuirk. Enhanced External Aerodynamic Performance of a Generic Combustor Using An Integrated OGV/Prediffuser Design Technique. *Journal of Engineering for Gas Turbines and Power*, 129(1):80–87, 02 2006.

[83] J. Li, G. Page, and J. McGuirk. Coupled reynolds-averaged navier–stokes/large-eddy simulation for outlet guide vane and prediffuser flows. *AIAA Journal*, 53(3):678–691, 2015.

[84] R. De Robbio. Micro gas turbine role in distributed generation with renewable energy sources. *Energies*, 16(2):704, 2023.

[85] R. Banihabib and M. Assadi. The role of micro gas turbines in energy transition. *Energies*, 15(21):8084, 2022.

[86] F. Ji, X. Zhang, F. Du, S. Ding, Y. Zhao, Z. Xu, Y. Wang, and Y. Zhou. Experimental and numerical investigation on micro gas turbine as a range extender for electric vehicle. *Applied Thermal Engineering*, 173:115236, 2020.

[87] R. Capata and M. Saracchini. Experimental campaign tests on ultra micro gas turbines, fuel supply comparison and optimization. *Energies*, 11(4):799, 2018.

[88] Z. Habib, R. Parthasarathy, and S. Gollahalli. Performance and emission characteristics of biofuel in a small-scale gas turbine engine. *Applied energy*, 87(5):1701–1709, 2010.

[89] J. Large and A. Pesyridis. Investigation of micro gas turbine systems for high speed long loiter tactical unmanned air systems. *Aerospace*, 6(5):55, 2019.

[90] E. C. Okafor, K. K. A. Somarathne, A. Hayakawa, T. Kudo, O. Kurata, N. Iki, and H. Kobayashi. Towards the development of an efficient low-nox ammonia combustor for a micro gas turbine. *Proceedings of the combustion institute*, 37(4):4597–4606, 2019.

[91] C. Zong, C. Ji, J. Cheng, T. Zhu, D. Guo, C. Li, and F. Duan. Toward off-design loads: Investigations on combustion and emissions characteristics of a micro gas turbine combustor by external combustion-air adjustments. *Energy*, 253:124194, 2022.

[92] A. H. Lefebvre. Fuel effects on gas turbine combustion-liner temperature, pattern factor, and pollutant emissions. *Journal of Aircraft*, 21(11):887–898, 1984.

[93] M. Chmielewski, P. Niszczota, and M. Gieras. Combustion efficiency of fuel-water emulsion in a small gas turbine. *Energy*, 211:118961, 2020.

[94] M. Chmielewski and M. Gieras. Impact of variable geometry combustor on performance and emissions from miniature gas turbine engine. *Journal of the Energy Institute*, 90(2):257–264, 2017.

[95] D. W. Naegeli, L. G. Dodge, and C. A. Moses. Effects of flame temperature and fuel composition on soot formation in gas turbine combustors. *Combustion science and technology*, 35(1-4):117–131, 1983.

[96] T. M. Rault, R. B. Vishwanath, and Ö. L. Gülder. Impact of ethanol blending on soot in turbulent swirl-stabilized jet a-1 spray flames in a model gas turbine combustor. *Proceedings of the Combustion Institute*, 38(4):6431–6439, 2021.

[97] H. M. Phan and L. He. Efficient steady and unsteady flow modeling for arbitrarily mis-staggered bladerow under influence of inlet distortion. *Journal of Engineering for Gas Turbines and Power*, 143(7):071009, 2021.

[98] H. M. Phan. Modeling of a turbine bladerow with stagger angle variation using the multi-fidelity influence superposition method. *Aerospace Science and Technology*, 121:107318, 2022.

[99] H. M. Phan and L. He. Efficient modeling of mistuned blade aeroelasticity using fully-coupled two-scale method. *Journal of Fluids and Structures*, 115:103777, 2022.

[100] K. Miki, J. Moder, and M.-S. Liou. Computational study of combustor–turbine interactions. *Journal of Propulsion and Power*, 34(6):1529–1541, 2018.

[101] H. M. Phan, P. H. Duan, and C. T. Dinh. Numerical aero-thermal study of high-pressure turbine nozzle guide vane: Effects of inflow conditions. *Physics of Fluids*, 32(3), 2020.

[102] T. Shang and A. H. Epstein. Analysis of Hot Streak Effects on Turbine Rotor Heat Load. *Journal of Turbomachinery*, 119(3):544–553, 07 1997.

[103] D. J. Dorney, R. L. Davis, D. E. Edwards, and N. K. Madavan. Unsteady analysis of hot streak migration in a turbine stage. *Journal of Propulsion and Power*, 8(2):520–529, 1992.

[104] M. Teixeira, L. Romagnosi, M. Mezine, Y. Baux, J. Anker, K. Claramunt, and C. Hirsch. A methodology for fully-coupled cfd engine simulations, applied to a micro gas turbine engine. In *Turbo Expo: Power for Land, Sea, and Air*, volume 51012, page V02CT42A047. American Society of Mechanical Engineers, 2018.

[105] A. M. Briones, A. W. Caswell, and B. A. Rankin. Fully coupled turbojet engine computational fluid dynamics simulations and cycle analyses along the equilibrium running line. *Journal of Engineering for Gas Turbines and Power*, 143(6):061019, 2021.

[106] O. A. Ozsoysal. Effects of combustion efficiency on an otto cycle. *International Journal of Exergy*, 7(2):232–242, 2010.

[107] Y. He and C.-H. Kim. Effect of nozzle port shape of fuel injector of micro gas turbine engine combustor on mixture gas formation for combustion. *Fluids*, 7(6):184, 2022.

[108] F. Raynaud, R. L. G. M. Eggels, M. Staufer, A. Sadiki, and J. Janicka. Towards Unsteady Simulation of Combustor-Turbine Interaction Using an Integrated Approach. In *Turbo Expo: Power for Land, Sea, and Air Volume 2B: Turbomachinery*, page V02BT39A004, 06 2015.

[109] C. Koupper, G. Bonneau, L. Gicquel, and F. Duchaine. Large Eddy Simulations of the Combustor Turbine Interface: Study of the Potential and Clocking Effects. In *Turbo Expo: Power for Land, Sea, and Air Volume 5B: Heat Transfer*, page V05BT17A003, 06 2016.

[110] F. Lo Presti, M. Sembritzky, B. Winhart, P. Post, F. di Mare, A. Wiedermann, J. Greving, and R. Krewinkel. Numerical Investigation of Unsteady

Combustor Turbine Interaction for Flexible Power Generation. *Journal of Turbomachinery*, 144(2):021003, 09 2021.

[111] F. Duchaine, J. Dombard, L. Gicquel, and C. Koupper. Integrated Large Eddy Simulation of Combustor and Turbine Interactions: Effect of Turbine Stage Inlet Condition. In *Turbo Expo: Power for Land, Sea, and Air Volume 2B: Turbomachinery*, page V02BT41A014, 06 2017.

[112] P. Flaszynski, M. Piotrowicz, and T. Bacci. Clocking and potential effects in combustor–turbine stator interactions. *Aerospace*, 8(10):285, 2021.

[113] K. Miki, T. Wey, and J. Moder. Computational study on fully coupled combustor–turbine interactions. *Journal of Propulsion and Power*, 39(4):540–553, 2023.

[114] S. Salvadori, G. Riccio, M. Insinna, and F. Martelli. Analysis of Combustor/Vane Interaction With Decoupled and Loosely Coupled Approaches. In *Turbo Expo: Power for Land, Sea, and Air Volume 8: Turbomachinery, Parts A, B, and C*, pages 2641–2652, 06 2012.

[115] I. Verma, L. Zori, J. Basani, and S. Rida. Modeling of Combustor and Turbine Vane Interaction. In *Turbo Expo: Power for Land, Sea, and Air Volume 2C: Turbomachinery*, page V02CT41A014, 06 2019.

[116] T. H. Nguyen, P. Nguyen-Tri, X. Vancassel, and F. Garnier. Aerothermodynamic and chemical process interactions in an axial high-pressure turbine of aircraft engines. *International Journal of Engine Research*, 20(6):653–669, 2019.

[117] A. A. Perpignan, S. G. Tomasello, and A. G. Rao. Evolution of emission species in an aero-engine turbine stator. *Aerospace*, 8(1):11, 2021.

[118] H. M. Phan and L. He. Investigation of structurally and aerodynamically mistuned oscillating cascade using fully coupled method. *Journal of Engineering for Gas Turbines and Power*, 144(3):031009, 2022.

[119] H. M. Phan. A spatial–temporal analysis approach for flutter predictions using decoupled and fully-coupled methods. *Journal of Fluids and Structures*, 107:103412, 2021.